# Mapping the natural visual world of the zebrafish (*Danio rerio*): from sensory input to behavioural output

Noora Emilia Nevala

Submitted for the degree of Doctor of Philosophy

University of Sussex

August 2020

# Declaration

This thesis conforms partly to an 'article format' in which the Chapter 2 is written in a format that is suitable for publication in a peer-reviewed journal. In addition, Chapters 3 and 4 include data that has been published in peer-reviewed journals. Nevertheless, Chapters 3 and 4 have been completely re-written by Noora Emilia Nevala. Throughout the thesis, only data, analysis and writing that is solely Noora Emilia Nevala's own work is presented, unless specifically declared otherwise.

For this thesis the general form of all chapters has been accommodated to present a uniform style. The first and final chapters present overviews and discussions of the field and the research undertaken.

**Chapter 2** has been published in Scientific Reports.

**A low-cost hyperspectral scanner for natural imaging and the study of animal colour vision above and under water**

Noora E Nevala and Tom Baden

For Chapter 2, NEN was responsible for all aspects of building the scanner, data collection and writing of the manuscript; TB was responsible for providing feedback on study design and corrections to the manuscript. Custom scripts were written by TB and modified by NEN. Manual for the scanner presented in the Appendix 1 of this thesis was created by NEN.

**Chapter 3** shows data that has been published in Current Biology.

**Zebrafish Differentially Process Color across Visual Space to Match Natural Scenes**

Maxime J.Y. Zimmermann*, MJY, Nevala*, NE, Yoshimatsu*, T, Osorio, D, Nilsson, D-E, Berens, P and Baden, T. **Co-first author*

**Chapter 4** shows data that has been published in Neuron.

**Fovea-like Photoreceptor Specializations Underlie Single UV Cone Driven Prey-Capture Behavior in Zebrafish**

Yoshimatsu, T, Schröder, C, Nevala, NE, Berens, P and Baden, T

---

I hereby declare that this thesis has not been and will not be, submitted in whole or in part to another University for the award of any other degree.

Signature: .....

## Summary

Vision is one of the most crucial senses for animals to catch prey, find mates and stay alive. The tetrachromatic zebrafish (*Danio rerio*) is a widely used model animal in visual neuroscience with four cone photoreceptors sensitive to UV, blue, green and red light. However, a detailed understanding of how their visual system is adapted to the natural environment, and what is important for the fish to see in their shallow freshwater habitats of the Indian subcontinent, has been missing. Therefore, it also has not been possible to carefully assess the importance of different parts of the light spectrum for their natural behaviours. In this thesis I introduce a new method for natural imaging, characterise the spectral composition of zebrafish's natural visual world and demonstrate the role of UV light in their prey capture behaviours.

To characterise the light conditions in natural environments, I developed and built two hyperspectral scanners to take spectrally detailed light measurements in shallow ponds and slowly moving streams in North-East India. As expected, the spectral profile becomes increasingly monochromatic and red shifted when moving from surface to the bottom. However, the short wavelength dominated surface and long wavelength dominated bottom are separated with colour-rich horizon. These spectral statistics match rather perfectly with the cone densities and colour processing abilities of the bipolar cells in the larval zebrafish retina.

Previous work has demonstrated how prey capture behaviours on larval zebrafish can be triggered by small, bright spots. The short wavelength dominated upper part of the visual field projects light from UV bright prey items perfectly to the ventro-temporal part of the retina ("strike zone") with high density of UV cones. Finally, with my behaviour experiments I demonstrate how prey capture behaviours are strongly driven by UV bright paramecia detected with the strike zone.

# Acknowledgements

I would like to thank my supervisor Tom Baden for giving me this amazing opportunity to work on this project and taking me into his lab. Over the years he has not only offered his guidance through puzzling research questions, but also inspired me to think outside the box and pushed me to try even the craziest ideas.

Thank you for the School of Life Sciences for funding my whole PhD. I want to thank my colleagues and other staff at the Sussex University and in the Baden Lab, especially Takeshi Yoshimatsu, Natasha Pouchkina-Stantcheva, Andre Maia Chagas, Hazel Smulders and Jeremy Niven for all the help they have given me. I have learned a lot from you.

I am forever grateful for all the laughs and encouragement I have shared and received with Ragnheidur, Louise, Tessa and Takeshi. I also want to thank all my other friends in the UK and in Finland for supporting me.

Finally, I want to thank my friend Tuuli, my partner Peter, my mother Irja and my brother Niko. This thesis would not have been possible without your endless love and support. You all inspire me every day and keep me going when I feel like quitting.

# Table of Contents

# List of Figures and Tables

## Chapter 1



## Chapter 2



## Chapter 3

## Chapter 4

# Abbreviations and symbols

| | |
|---|---|
| ° | Degree |
| ⌀ | Diameter of a circle |
| % | Percentage |
| £ | Pound |
| β | Beta |
| λ | Lambda, wavelength |
| $\lambda_{max}$ | Wavelength at which a substance shows maximum absorbance |
| θ | Theta |
| π | Pi (~3.14159) |
| 2D | Two-dimensional |
| 3D | Three-dimensional |
| A1 | 11-*cis*-retinal chromophore |
| A2 | 11-*cis*-3,4-didehydroretinal chromophore |
| Abs. | Absorption |
| am | Ante meridiem, before midday |
| a.u. | Arbitrary unit |
| B | Blue |
| *c* | Speed of light in vacuum (299 792.5 km/s) |
| °C | Celsius degree |
| $C_{1, 2, 3}$ | Chromatic axis 1-3 |
| CCD | Charge-coupled device |
| cm | Centimetre |
| cpd | Cycles per degree |
| Cumul. | Cumulative |
| Cyp27c1 | A protein (enzyme) that is encoded by the CYP27C1 gene |
| D10, 11, 13 | Digital pins on Arduino board |
| DIY | Do-it-yourself |
| DNA | Deoxyribonucleic acid |
| *dpf* | Days post fertilization |
| *E* | Energy |
| Fig. | Figure |
| FOV | Field of view |
| G | Green |
| GND | Ground |
| *h* | Planck's constant ($6.62607015 \times 10^{-34}$ J/s) |
| h | Hour |
| IR | Infrared |
| IRPB | Interophotoreceptor retinoid-binding protein |
| km | Kilometre |
| lat. | Latitude |
| LED | Light-emitting diode |
| long. | Longitude |
| LWS | Long wavelength sensitive |

| | |
|---|---|
| m | Metre |
| min | Minute |
| ml | Millilitre |
| mm | Millimetre |
| ms | Millisecond |
| MSP | Microspectrophotometer |
| MWS | Middle wavelength sensitive |
| *n* | Sample size |
| nm | Nanometre |
| Norm. | Normalised |
| PC | Principal component |
| PC1-4 | Principal component 1-4 |
| PCA | Principal component analysis |
| pm | Post meridiem, after midday |
| PVC | Polyvinyl chloride |
| *r* | Radius |
| R | Red |
| RGB | Red-green-blue |
| s | Second |
| SD | Standard deviation |
| s.e.m. | Standard error of mean |
| SNR | Signal-to-noise |
| SWS | Short wavelength sensitive |
| T50 | Value for 50% of the maximal transmittance of light |
| Tr. | Transmission |
| TTL | Transistor-transistor logic |
| U | UV |
| UHI | Underwater hyperspectral imager |
| µm | Micrometre |
| USB | Universal serial bus |
| UV | Ultraviolet |
| UVS | Ultraviolet sensitive |
| V | Volt |
| Vin | Input power pin on Arduino board |
| WT | Wild-type |

# *Chapter 1 – General introduction*

Vision is one of the most important senses for an animal to gain information from their surrounding world. Main features in the visual environment are constructed from changes in overall illumination based on the direction of the light source (the sun) and possible objects obstructing the light and creating shadows. Using the spectral and spatial visual information individuals can move and position themselves in their environments in the most suitable way to preserve energy, avoid predators, locate food sources and detect conspecifics. These different behaviours are triggered by specific visual cues and are designed to provide the best possible survival.

Rod and cone photoreceptors in the outermost part of the retina create the first steps in vision. Colour vision is based on a variety of cones absorbing photons from specific wavelengths of light at day light or "photopic" levels, whereas rods can function at dimmer "scotopic" light (Land and Nilsson, 2012). The sensation of seeing colours requires at least two different cone types that are most sensitive to different parts of the light spectrum independent from intensity (Baden and Osorio, 2019). Information coming from photoreceptors is compared and analysed in the neural part of the retina (bipolar, ganglion, horizontal and amacrine cells) before further processing in the brain and eventual behavioural response (Rodieck, 1998). Before light can reach the photoreceptors, however, there are other structures in the vertebrate eyes (cornea, lens and vitreous) that can contain additional light absorbing pigment granules. These structures and pigments can also affect the light spectrum available for visual sensation by absorbing possibly harmful, shorter wavelengths (Zigman, 1971). The sensitivity of the photoreceptors in addition to the existence and composition of these additional light absorbing structures depend on the spectral environment an animal is living in and what species-specific needs for survival they have. To understand these adaptations and visual requirements, it is important to study what there is to see in the animal's natural environments and how this information relates to certain behaviours.

In this chapter, I describe the natural habitats of zebrafish (*Danio rerio*) based on previous studies and observations in the field and how the study of natural imaging can be used to study natural spectral environments. Then, I give a general introduction to zebrafish's spectral sensitivity and colour vision abilities. Finally, I will briefly focus on previous studies done on zebrafish larvae's prey capture behaviours and how these could be driven by specific cone channels.

### 1.1 Zebrafish ecology and natural environment

Zebrafish are widely distributed on the Indian subcontinent (Fig. 1.1), with the highest densities of the observation sites focusing around the North-East parts of the country (Parichy, 2015). In nature they inhabit mostly small ponds, slowly moving streams and other still pools of shallow (<50 cm) water (McClure, McIntyre and McCune, 2006; Spence *et al.*, 2006; Engeszer *et al.*, 2007), but are also widely found in human cultivated rice paddies and fisheries (Spence *et al.*, 2006, 2007). There does not seem to be clear preference over open water or vegetation as both are commonly seen in these habitats together with varying types or substrate materials.

The Indian subcontinent has regular monsoon seasons, when most rivers flood and overflow creating small side rivers and ponds. In addition to rice paddies, these smaller pockets of water create ideal conditions for breeding between April and August with no predators and large amounts of nutrients rising from the substrate after rain. However, zebrafish adults are known to feed on their own eggs and larvae, and when occurring in water bodies with other larger fish species adult zebrafish have been found in the guts of snakehead fish (*Canna*), knifefish (*Notopterus*) and catfish (Spence *et al.*, 2006; Engeszer *et al.*, 2007). Both adult and larvae zebrafish themselves are omnivorous foraging on almost anything from insects dropping into the water from overhanging vegetation to zooplankton, algae and plant materials (Arunachalam *et al.*, 2013).

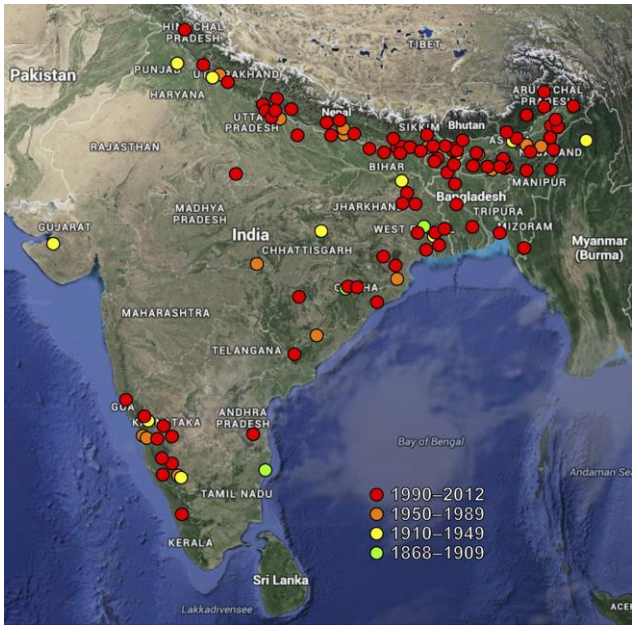


**Figure 1.1.** Distribution of observation sites for zebrafish on the Indian subcontinent between 1868 and 2012 (modified from Parichy, 2015).

As the different structures and amount of vegetation in these underwater habitats can vary drastically, the visual environment for the fish is not always the same. In addition, the spectrum of light entering the water column can change over the time of the day and year depending on the position of the sun (McFarland, Ogden and Lythgoes, 1979; Cronin *et al.*, 2014). To better understand how the zebrafish visual system is adapted to these environments, it is important first to know how light behaves in water.

## 1.2 Light and hyperspectral imaging

### *1.2.1 Light spectrum in nature*

All light in nature is electromagnetic radiation originating from the sun, and can be described as rays, particles (photons) or waves. As photons, these massless particles hold a certain amount of energy that can be calculated with a simple equation:

$$E = \frac{hc}{\lambda}$$

where *h* is Planck's constant, *c* is speed of light in vacuum (299 792.5 km/s) and λ is the photon's wavelength. Therefore, the energy one photon holds is inversely proportional to the wavelength: shorter wavelengths have higher energy than longer wavelengths (Johnsen, 2012). In vision science the most common way to describe light is with photons, and especially as photons per time per area ($s^{-1}m^2$). The light intensity increases as the number of photons increases over time and the amount of energy photons hold increases as wavelength becomes shorter (Land and Nilsson, 2012).

Different wavelengths of light can be perceived as different colours. The light spectrum often described as "visible" is between 380 and 700 nm (Fig. 1.2), where the spectral sensitivity of human photoreceptors lies within. However, a wide variety of animals, especially some fish, amphibian, reptile, bird and many invertebrate species, can also see ultraviolet (UV) light below 400 nm (Baden and Osorio, 2019).

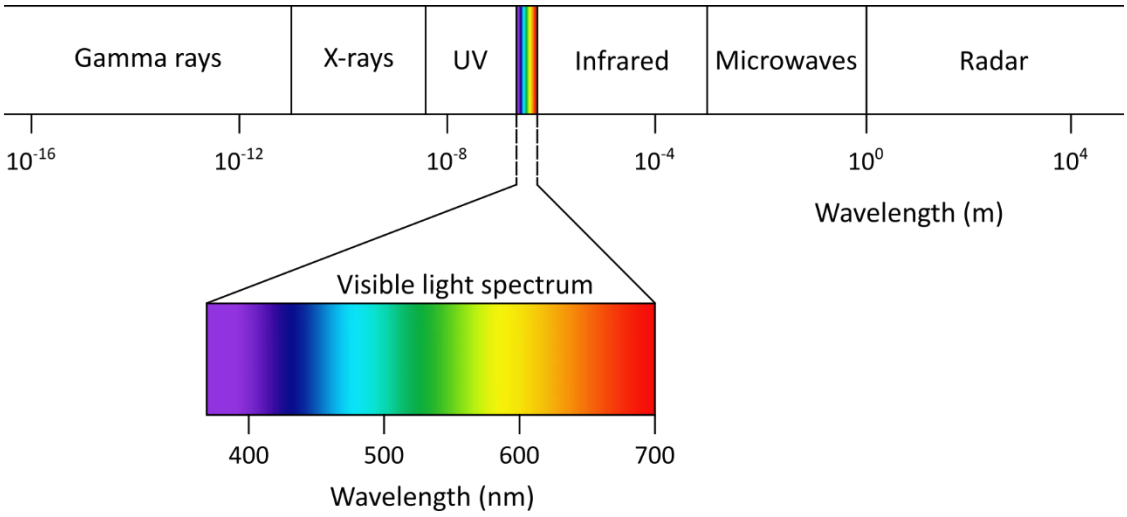


**Figure 1.2.** Spectrum of light. Created after Johnsen (2012).

The light spectrum reaching the eye depends on the illuminant and the object reflecting the light (Endler, 1993), as different surfaces absorb and reflect different parts of the light spectrum. Medium where light travels (air or water) can also have a strong effect, as water and particles in it absorb and scatter the light rays moving through. Light intensity decreases with increasing depth when moving from the water surface towards the bottom and the spectral range becomes more monochromatic (Levine and MacNichol, 1982). First, the shortest and longest wavelengths are scattered and absorbed already close to the surface whereas medium wavelengths penetrate to the deeper layers (Fig. 1.3). Second, the effect is even stronger on the short wavelengths in fresh water because of the higher amount of dissolved, organic material. For this, the light spectrum under the sea has a transmission maximum below 500 nm, whereas in fresh waters it can be red shifted close to 650 nm.

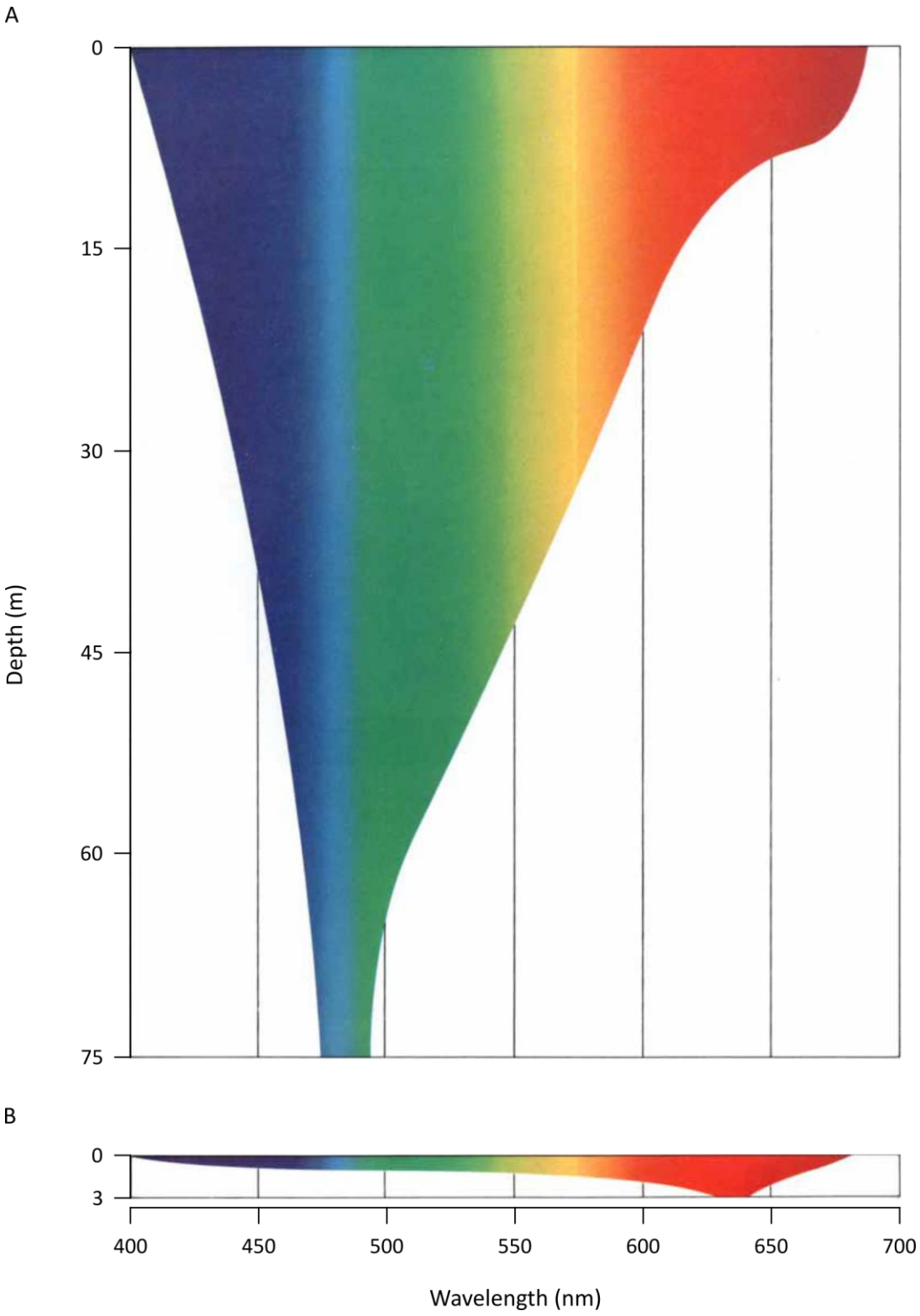


**Figure 1.3.** Light transmission in sea **(A)** and fresh water **(B)**. Light intensity decreases with increasing depth and the spectrum becomes more monochromatic, with clear red shift in fresh water. Modified after Levine and MacNichol, 1982.

*1.2.2 Hyperspectral imaging*

Even if different species would inhabit the exact same environment with the same spectral input, it is unlikely that they would see the world in the same way. Several different properties in the visual system can affect this, such as field of view, spatial resolution an eye can resolve and the spectral sensitivity of the light absorbing photoreceptors. These species-specific features have evolved to best fulfil the behavioural requirements for survival. To study how an animal can see their spectral environment, one must take accurate light measurements and analyse them according to the spectral sensitivity of the species. Different objects and surfaces in nature provide different types of information for an individual to see and to react on. The first step to understand the surrounding spectral world is to take measurements combining spatial and spectral information from the scene with hyperspectral imaging. Then, these datasets can be analysed, for example, based on the study animal's spectral sensitivity and spatial resolution abilities to extract chromatic and spatial details relevant to the species.

Hyperspectral imaging is a common technology in industries to study the quality of food (Gowen *et al.*, 2007; ElMasry, Sun and Allen, 2012) and crops (Lelong, Pinet and Poilve, 1998; Monteiro *et al.*, 2007; Feng *et al.*, 2019) but also to take images in astrology (Goetz *et al.*, 1985), earth surface observations (Uto *et al.*, 2016a, 2016b) and medical diagnostics (Lu and Fei, 2014). Outside industry, previous research has focused on taking images in a variety of natural and human influenced scenes to analyse the common spatial and chromatic features and how well these match the human vision abilities to process spectral information (Nagle and Osorio, 1993; Osorio, Ruderman and Cronin, 1998; Ruderman, Cronin and Chiao, 1998; Lewis and Li, 2006). These and several other studies (except Lewis and Li, 2006) used a high spatial resolution, CCD camera system with narrow (10-15 nm) bandpass interference filters in 7-20 nm intervals in the approximate range of 400-700 nm. An image of the scene is taken with each filter to produce a hyperspectral dataset from one scene. All these datasets were analysed with trichromat human spectral sensitivity, with cone photoreceptors sensitive to red (R), green (G) and blue (B). Importantly, human red and green cones mostly overlap, producing rather similar input to the visual system. Most variation from all scenes is explained by changes in general illumination where each photoreceptor is equally activated, producing an achromatic presentation of the observed scene. Therefore, all the remaining chromatic variation is created either by red and green (yellow) vs. blue or red vs. green opponency. In addition, Ruderman, Cronin and Chiao (1998) found that the opponent colour channels detect spatial patterns from the observed scene and these patterns in one channel cannot be predicted from the representation in another one.

Animals are expected to adapt to their surrounding environments in the best possible way to optimize the energy used to survive. This can be easily thought to mean that the vision systems should always be tuned to extract the maximal amount of spatiochromatic information. Interestingly, the overlapping red and green cones in humans are not tuned to see most chromatic variation available in natural scenes (Nagle and Osorio, 1993; Lewis and Li, 2006). The current positions of these photoreceptors seem to be located well to observe the possible variation at longer wavelengths to estimate the ripeness of the fruits and seems to be well conserved during the evolution of Old World primates (Jacobs and Deegan, 1999). Shifting the red cones towards longer wavelengths could increase the amount of colour information obtained from the scene, but this would be a trade off by making the red cones thermally too unstable and reducing sensitivity in dim light (Koskelainen *et al.*, 2000; Lewis and Li, 2006).

The CCD camera system with narrow bandpass filters provides a good representation of the surrounding spectral environment. However, the spectral resolution is not accurate enough to distinguish fine spectral variations and light spectrum below 400 nm (UV) has been lacking. In 2019 Tedore and Nilsson used a multispectral imaging approach where they designed individual filters to represent the spectral sensitivity of each individual cone (UV, blue, green and red) from an avian visual system. As with hyperspectral filter approach, an image of the same scene is taken with each filter. These produce high spatial resolution images that represent the studied scene as it would appear for each individual cone type. Detailed filters with a high spatial resolution camera provide accurate information and are the best option to study individual animal species. Unfortunately, this approach is expensive and out of reach for most basic research. In addition, the gathered dataset is truly usable only for the specific animals and cannot be used reliably for others.

As explained above, light is attenuated and spectrally shifted when moving through a water body. This alone creates a different spectral environment for the animal living below the surface. So far only a few studies have been devoted to spectrally map under water environments (Chiao, Cronin and Osorio, 2000; Johnsen *et al.*, 2013, 2016). Chiao, Cronin and Osorio (2000) used the previously mentioned narrow bandpass filter approach between 400-700 nm to study both terrestrial and coral reef scenes at 3-5 meters depth. As in line with previous terrestrial data, most of the variation in the underwater and terrestrial environments are again explained with achromatic luminance changes across the scene. Also, the main chromatic comparison is done with long vs. short wavelengths.

Although there have been several studies to study light spectrum in natural scenes, the measurements in shallow waters including UV have been lacking. Previous approaches with interference filters could provide solution, but the equipment is often costly and not easily available for basic research. In 2013 Baden *et al.* used an optic fibre attached to two servomotors with a spectrometer to take wide spectrum, terrestrial images including UV. With this "DIY" approach it possible to significantly reduce the cost of equipment. Unfortunately, the optic fibre makes their design fragile and bulky and therefore non-optimal for waterproofing to include measurements from underwater scenes.

In Chapter 2, I present the design and usability of my approach for a low-cost, DIY hyperspectral scanner to take high spectral resolution images both underwater and terrestrial environments. I also demonstrate how my method can be used to study spectral sensitivity of any animal with known spectral sensitivity. In Chapter 3 I bring the focus back to zebrafish and their natural spectral environments by showing my hyperspectral imaging results from India taken with two different hyperspectral scanner designs.

## 1.3 Vision system of the zebrafish

Zebrafish have a typical vertebrate eye where the light from the environment must pass first through a cornea, lens, vitreous and neuronal part of the retina to reach rod and cone photoreceptor cells at the back of the eye. Once photons reach the visual pigments held in the outer segments of these cells, there is a possibility for a phototransduction cascade to begin and the light signal can be transferred further to the neuronal part of the retina and to the brain for processing. However, before photons can initiate the phototransduction cascade there are several structures and properties in the eyes before the retina and in the photoreceptor cells that alter the spectrum of light and to what part of the light the cells are most sensitive to.

### *1.3.1 Zebrafish spectral sensitivity*

Zebrafish are tetrachromatic animals with four different cones and one rod photoreceptor types: UVS (ultraviolet sensitive), SWS (short wavelength sensitive), MWS (middle wavelength sensitive), LWS (long wavelength sensitive) and a rod (Branchek and Bremiller, 1984; Allison *et al.*, 2004). In adult zebrafish two single cones (UVS and SWS) and a double cone with principal and accessory members (LWS and MWS, respectively) are arranged in rows with regularly alternating, mosaic pattern (Engstrom, 1960; Robinson *et al.*, 1993; Allison *et al.*, 2010).

However, in larval zebrafish all cones are single cones, the average densities of different cones vary across the retina and the mosaic pattern seen in adult retina is lacking (Allison *et al.*, 2010; Zimmermann *et al.*, 2018). As explained in Chapter 3, the anisotropic arrangement of the cone photoreceptors in the larval zebrafish seems to match rather perfectly with the distribution of different wavelengths of light in their natural environment (Zimmermann *et al.*, 2018).

The spectral sensitivity range of vertebrate cones lies between 300-650 nm (Baden and Osorio, 2019). The specific wavelength for peak sensitivity where the pigment in the photoreceptor outer segment is most likely to absorb a photon ($\lambda_{max}$) depends, among other things, on the amino acid complement of the opsin the cells hold in their outer segments (Hunt *et al.*, 2001). In zebrafish, the $\lambda_{max}$ of the UVS cones expressing SWS1 opsin is at 355-365 nm and for the SWS cones expressing SWS2 opsin at 411-416 nm, hereafter called UV and blue cones, respectively (Table 1.1) (Chinen *et al.*, 2003; Allison *et al.*, 2004). However, with MWS and LWS cones the opsin complement has more variety. An MWS cone (hereafter green cone) has four different opsins it can express: RH2-1 ($\lambda_{max}$ at 467 nm), RH2-2 ($\lambda_{max}$ at 476 nm), RH2-3 ($\lambda_{max}$ at 488 nm) and RH2-4 ($\lambda_{max}$ at 505 nm). In LWS cones (hereafter red cones) the possible opsins are LWS1 ($\lambda_{max}$ at 558 nm) at LWS2 ($\lambda_{max}$ 548 nm). The rod photoreceptors have only one possible opsin type (RH1) with $\lambda_{max}$ at 501 nm. The most common opsins expressed in green and red cones varies across the retina and changes during the development state (Robinson, Schmitt and Dowling, 1995; Chinen *et al.*, 2003; Takechi and Kawamura, 2005a). During the first week of development (within 7 days post fertilization, "*dpf*") the RH2-1, RH2-2 and LWS2 are the most common opsins covering the central regions of retina (Takechi and Kawamura, 2005a). Later RH2-3, RH2-4 and LWS1 opsins are also expressed in the regions around the centre. This implies that the young zebrafish larvae are more sensitive to the shorter wavelengths than the older larvae and adults. In addition, the longer wavelength sensitive versions of the green and red opsins (RH2-3, RH2-4 and LWS1) are more frequently expressed around the edges and in the ventral side of the retina looking upwards in the visual field with the shorter wavelength version focused more in the centre or back of the eye.

| UV cone | Blue cone | Green cone | Red cone | Rod |
|---|---|---|---|---|
| SWS1 – 355-365 nm | SWS2 – 411-416 nm | RH2-1 – 467 nm* | LWS1 – 558 nm | RH1 – 501 nm |
| | | RH2-2 – 476 nm | LWS2 – 548 nm* | |
| | | RH2-3 – 488 nm | | |
| | | RH2-4 – 505 nm | | |

**Table 1.1.** Zebrafish cone types, opsin classes and $\lambda_{max}$ values for the corresponding visual pigments (Chinen *et al.*, 2003; Allison *et al.*, 2004). The most common opsins types of the green and red cones for the zebrafish larvae (< 10 *dpf*) have been marked with an asterisk (*).

As explained above, animals can tune the spectral sensitivity of their photoreceptors by changing the opsin complement of the visual pigment (Hubbard and Sperling, 1973; Chang *et al.*, 1995; Yokoyama *et al.*, 1999). This requires changes in the amino acid sequence that will be translated to the functional opsin protein. Mutations altering the $\lambda_{max}$ of the opsin are mostly located near the Shiff's base in the "pocket" holding the chromophore, where this protonated base forms a covalent bond between amino acid lysine and the chromophore (Nathans, 1990; Chang *et al.*, 1995; Park *et al.*, 2008). However, mutations in the opsins can happen only by changing the DNA coding of the opsin in evolutionary time scale (Yokoyama *et al.*, 1999). The spectral sensitivity of a photoreceptor depends also on the type of the chromophore that is bound to the opsin. In vertebrates, two types of chromophores exist: 11-*cis*-retinal and 11-*cis*-3,4-didehydroretinal (hereafter A1 and A2 vitamin, respectively). When the opsin protein is binding A1 vitamin, the visual pigment is called rhodopsin whereas with A2 vitamin the pigment is called porphyropsin. A2 vitamin holds an additional double bond in the β-ionone ring (Wald, 1939), which causes lowering of the activation energy when a photon is absorbed, a broader absorbance spectrum and in general shifting the $\lambda_{max}$ of the visual pigment 25-30 nm towards the longer wavelengths (Bridges, 1965; Pahlberg, 2007; Enright, Toomey, S. Y. Sato, *et al.*, 2015). Because of the lower activation energy, visual pigments using A2 vitamin are more prone to thermal activation and have a larger scale of dark noise (Barlow, 1957; Donner, Firsov and Govardovskii, 1990; Koskelainen *et al.*, 2000; Ala-Laurila *et al.*, 2003; Ala-laurila *et al.*, 2007). These consequences of using the A2 chromophore can cause problems for animal vision since the phototransduction cascade is the same whether it is initiated by thermal activation or an

actual photon absorption. Therefore, animals that occupy environments with higher temperatures and/or higher body temperatures have limits how far in the longer wavelengths the spectral sensitivity is sensible to tune in. In principle, spectral tuning should be limited to the wavelengths that provide best adaptation for the visual behaviour and still has high enough signal to noise ratio to separate the random thermal activation events in the visual pigments from the activations occurred after absorption of a photon (Ala-Laurila *et al.*, 2003).

Several studies have demonstrated how animals tune their spectral sensitivities with A1-A2 chromophore switch depending on their life stages, time of the year and the environment they are living in (Whitmore and Bowmaker, 1989; Enright, Toomey, S. Y. Sato, *et al.*, 2015). In many amphibian species, such as American bullfrog (*Rana catesbeiana*), the A2 chromophore is more abundant in tadpoles and A1 more prevalent in adults after metamorphosis (Wilt, 1959; Liebman and Entine, 1968), while for example migratory lamprey and salmon make the opposite change when moving from ocean to fresh water to breed (Wald, 1957; Beatty, 1966). In many of these examples the role of thyroid hormone has been demonstrated to be part of the initiation of the shift. In addition, Enright et al. (2015) demonstrated how Cyp27c1 enzyme specifically is needed for the conversion. All zebrafish photoreceptors hold initially A1 chromophore, but thyroid hormone treatment mediates the switch from A1 to A2 shifting the spectral sensitivity of green and red cones to longer wavelengths (Allison *et al.*, 2004; Enright, Toomey, S. Y. Sato, *et al.*, 2015). However, currently there has been no studies to show if this shift happens during the natural life cycle of zebrafish in laboratory or wild animals and therefore the real role of A2 chromophore in the spectral sensitivity of this species remains unclear.

Because of the multiple options for opsins in green and red cones, varying expression across the retina at different life stages and the possible effect of two different chromophores on the spectral sensitivity of different cones, it is easy to get confused when thinking how zebrafish might perceive their surrounding world. To establish some boundaries and to make the results more clear, in this thesis I am mostly focusing on RH2-1 opsin for green cones and LWS2 opsin for red cones, since these are the most abundant ones in <10 *dpf* old larvae. I always assume that the chromophore bound to the opsin is A1 type. These statements in mind, Figure 1.4 illustrates the templates for spectral sensitivity curves of cones used throughout this thesis.

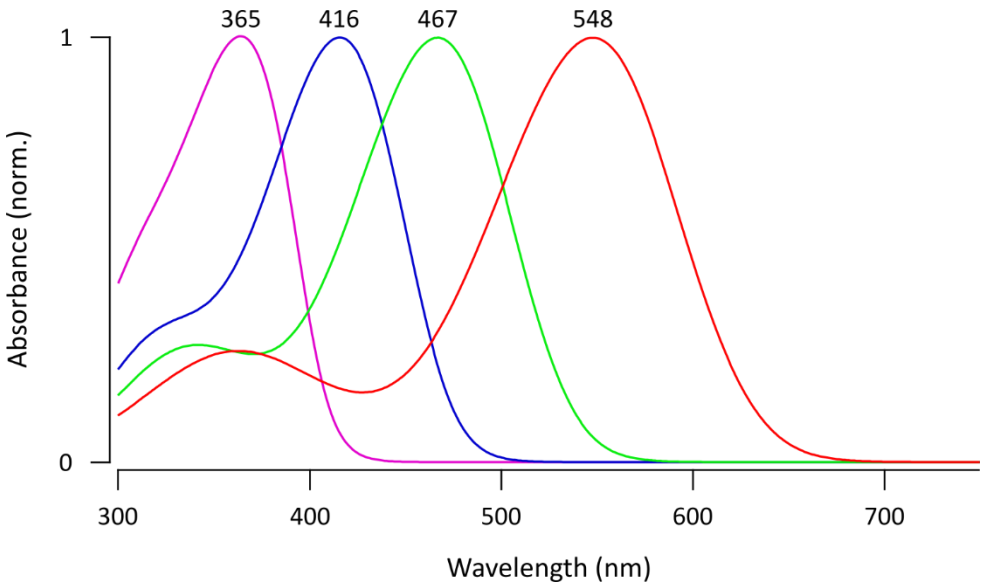


**Figure 1.4.** The spectral sensitivity curves (modified after Govardovskii *et al.*, 2000) with $\lambda_{max}$ values for UV, blue, green and red cones (pink, blue, green and red lines, respectively) when most abundantly expressed opsin types are bound to A1 chromophores in <10 *dpf* zebrafish larvae.

### *1.3.2 Ocular media*

In a vertebrate eye, ocular media consists of cornea, lens and vitreous, where the cornea and lens are responsible for refracting and focusing the incoming light to the correct layer of the retina on the outer segments of the photoreceptors to maximize the photon absorption and spatial resolution. Unlike in the adult zebrafish, in larval zebrafish eye the lens and retina fill out the whole eye and lie right next to each other leaving almost no space at all for the vitreous (Soules and Link, 2005). Furthermore, in aquatic vertebrates like zebrafish, the cornea has no optical power and the almost perfectly spherical lens is solely responsible in focusing the light (Land and Nilsson, 2012).

The ultraviolet (UV) part of the light can cause damages to the retina which has led some diurnal and shallow water fish species to develop a UV filtering pigmentation in the ocular media (Zigman, 1971; Douglas and McGuigan, 1989; Siebeck and Marshall, 2001). For animals like zebrafish with UV sensitive photoreceptors it makes no sense to have completely UV-blocking pigments in the optical path. However, small amounts of pigment can work as protecting filters still allowing small amounts of short wavelength photons to reach the retina. The preliminary measurements on broad range light transmittance through the dissected cornea and lens of an adult zebrafish suggest that 50% of the maximal transmittance of light (T50) is approximately at 320 nm (data not shown). Based on this finding it can be concluded that the effects of possible filtering pigments in the ocular media of a zebrafish adult are small. However, larger sample size

including both adult and larvae individuals are needed to make stronger statements on the light composition eventually reaching the photoreceptors at different life stages.

### *1.3.3 Photoreceptor patterns and spatial resolution in zebrafish*

As mentioned above, photoreceptors in adult zebrafish retina are arranged in a mosaic pattern with UV, blue, green and red cones alternating in tightly organized manner (Fig. 1.5) (Engstrom, 1960; Robinson *et al.*, 1993). Interestingly, larval zebrafish do not show any mosaic pattern but instead have varying cone densities across the retina (Zimmermann *et al.*, 2018). The highest density of UV cones is in the ventro-temporal part of the retina ("strike zone") while most of the blue cones are in the middle band of the eye looking straight forward. Long wavelength sensitive green and red cones have the highest numbers in the dorsal and middle part of the retina. The varying distribution of different cone types and the possible advantage of this for the larval zebrafish are discussed further in chapters 3, 4 and 5 of this thesis.

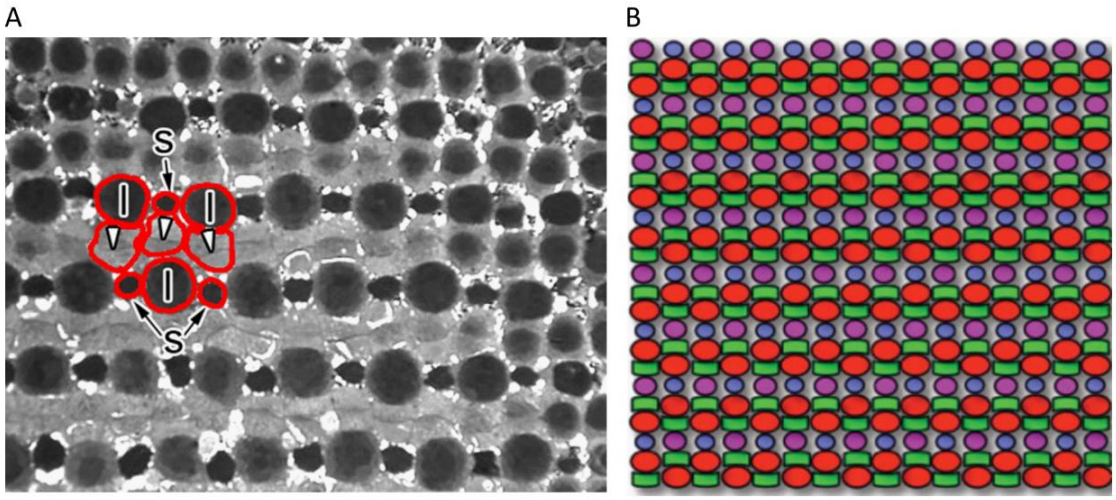


**Figure 1.5.** The cone mosaics in adult zebrafish retina. **A)** Microscopic image of the cone mosaics in the adult zebrafish retina. S = ultraviolet (UV) sensitive cone, I = blue sensitive cone and arrowhead = joined green and red sensitive cones Modified from Suliman and Novales Flamarique, 2014. **B)** Schematic picture of the UV, blue, green and red sensitive cone mosaic (purple, blue, green and red shapes, respectively). Modified from Allison *et al.*, 2010.

Among other properties of the eye, the physical limit of spatial resolution an animal eye can resolve depends on the photoreceptor density across the retina (Land and Nilsson, 2012). However, as the visual information is filtered and analysed through the neural retina and brain, the effective visual acuity can be assessed by behavioural testing, for example with an optokinetic response. These tests follow the eye movement reflex of the fish when presented

with moving stripes and determine what is the smallest detail the fish still reacts to at a constant speed (Bilotta and Saszik, 2001). Behavioural resolution limit on larval zebrafish is approximately 0.16 cycles per degree (cpd) or ~1° (Haug *et al.*, 2010), whereas adults have behavioural visual acuity at 0.58 cpd or ~3° (Tappeiner *et al.,* 2012).

### *1.3.4 Colour processing in the neural retina*

Before reaching the brain, information from photoreceptor cells is analysed and processed in horizontal, bipolar, amacrine and ganglion cells in the neural retina. After photoreceptors, horizontal cells have the first chance to alter the information before it reaches next neuronal layers. Here, the input from a cone to the horizontal cell can trigger an inhibitory input from the same horizontal cell to the same and other cones (Twig, Levy and Perlman, 2003). In addition to horizontal cells, photoreceptors make selective connections to bipolar cells as well. Interestingly, in zebrafish the bipolar cell wiring seems to match rather well with the anisotopic organization of the photoreceptors matching the natural statistics of colour in their environment (Chapter 3 and 5, Zimmermann *et al.*, 2018). This is especially true for the larval zebrafish, while the adults represent more other tetrachromatic vertebrates (Baden and Osorio, 2019). These colour-opponent bipolar cells feedforward to ganglion cells before reaching the brain. In zebrafish, the ganglion cells display complex colour opponency with regionally specialized areas (Zhou *et al.*, 2020). However, these recent studies provide only a glimpse to what seems to be functionally highly complex example of a vertebrate retina.

## 1.4 Prey capture behaviour in larval zebrafish

Zebrafish larvae have a completely functional cone array already at 4-5 *dpf* (Branchek, T., Bremiller, 1984; Raymond, Barthel and Curran, 1995; Saszik, Bilotta and Givin, 1999; Schmitt and Dowling, 1999). Starting already at 3 *dpf*, zebrafish larvae show first optokinetic tracking responses to a horizontally moving bar stimulus (Easter Jr. and Nicola, 1996; Neuhauss, 2003) which are entirely visually guided and necessary to detect and capture prey (McElligott and O'Malley, 2005). Since at this early age the retina lacks functional rod photoreceptors (Branchek, T., Bremiller, 1984), it can be assumed that the prey capture behaviour is cone driven. The early development of the visual system, fully sequenced genome and the possibilities to create genetically modified animals makes zebrafish an excellent option to study prey capture behaviours. As larvae, they feed on organic material and small zooplankton, such as single celled

paramecia (Lawrence, 2007). Interestingly, there is some evidence showing how live and moving diets can produce behaviourally more active individuals in captivity than artificial foods (Lawrence, 2007; Patterson *et al.*, 2013; Lagogiannis, Diana and Meyer, 2019) demonstrating how the visual cues during early life stages can have a strong effect on developing natural visually guided behaviours such as prey capture.

Before striking, zebrafish larva detects the prey and produces a sequence of locomotor movements to position the item in the upfront of the visual field for better observation and at striking distance ("strike zone"). Previous research have used both live paramecia and daphnia (Gahtan, Tanger and Baier, 2005; McElligott and O'Malley, 2005; Bianco, Kampff and Engert, 2011; Patterson *et al.*, 2013; Semmelhack *et al.*, 2014; Novales Flamarique, 2016; Muto and Kawakami, 2018; Mearns *et al.*, 2019) as well as artificial visual stimuli (Bianco, Kampff and Engert, 2011; Semmelhack *et al.*, 2014; Jouary *et al.*, 2016) of bright, moving spots to successfully evoke prey capture behaviours. Although live, naturally moving prey might feel as the obvious choice when studying natural behaviours, artificial stimuli has the advantage to control the size and speed of the presented "prey". The optimal size for a dot to elicit prey capture behaviour is approximately 3° when the spot is moving at 90°/s, while larger dots (> 10°) easily produce an avoidance reaction, possibly reminding of a looming predator (Bianco, Kampff and Engert, 2011; Semmelhack *et al.*, 2014).

After detection, the first response is the eye convergence to increase the binocular view (Fig. 1.6) (Bianco, Kampff and Engert, 2011; Patterson *et al.*, 2013). The degree of eye convergence does not depend on the distance of the prey from the larvae but the strength and direction of the tail movements (bouts) correlate with the location of the item triggering the movements (Patterson *et al.*, 2013; Trivedi and Bollmann, 2013). Because the first movements after prey detection are used to position the prey in the upper front part of the larvae, it is logical that items that are further to the sides of the fish and at longer distance produce stronger and faster bouts (J-turns) to move the animal quickly closer. When the prey is in front of the larvae to start with the tail movements are symmetrical and subtle, or the larva might even move backwards if the target is too close to attack and falls off the binocular field of view.

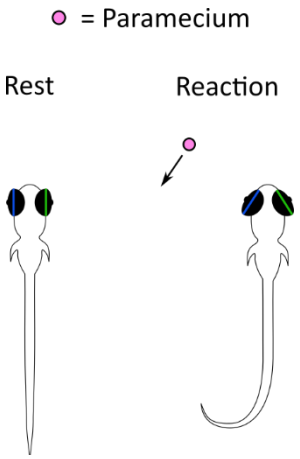


**Figure 1.6.** A schematic illustration of a zebrafish larvae at rest and after detecting a paramecium triggers eye convergence and tail flip reactions.

As explained above, previous research has carefully characterized the prey capture behaviour responses to moving dots and live prey items in both freely moving and constrained zebrafish larvae. Studies have demonstrated how prey capture behaviour is clearly visually guided as the successful prey capture events diminish in dark conditions, blind mutants and tectum ablated individuals (Gahtan, Tanger and Baier, 2005; Patterson *et al.*, 2013). However, experiments on zebrafish prey capture behaviour under different light conditions have been lacking. Since different objects and surfaces in nature reflect and absorb different parts of the ambient light spectrum, they can provide different types of information for an animal. Therefore, prey items could be seen as specific light channels for easy and efficient detection against otherwise crowded visual environment. The role of UV light has been studied in some planktivorous fish species as some pigmentated zooplanktons absorb wavelengths below 400 nm (Browman, Novales-Flamarique and Hawryshyn, 1994; Johnsen and Widder, 2001; Novales Flamarique, 2013). In addition, Novales Flamarique (2016) demonstrated how foraging performance towards *Daphnia manga* zooplankton was reduced in UV cone knock-out zebrafish compared to the wild types with normal UV vision, suggesting that UV vision serves enhanced contrast detection in short wavelengths. Although these promising results show how UV cones are important for prey capture in zebrafish, additional studies are needed to investigate the input from other cones. In Chapter 4 I present my results for the study of prey detection behaviours towards paramecia on constrained zebrafish larvae under red, green and UV light conditions.

*1.4.1 Cone channel isolation*

When studying the role of specific cone channels in animal's behaviour, such as the role of UV channel on prey detection in this thesis, an important factor is isolating the cone channels from others. In zebrafish, isolating the UV cone channel especially from overlapping blue and green channels is important. As explained in Chapter 4, in this thesis I have used the transgenic zebrafish line nfsB-mCherry to ablate UV cones from the larval zebrafish retina, and compared the behaviour response of these fish to the normal wild type line with normal UV vision.

Because individual photoreceptors cannot distinguish between changes in wavelength and intensity (principle of univariance, Rushton, 1972), another possibility to isolate cone channels could be to present the study animal a display with metameric colours. Metameric colours are perceived the same, but they hold different spectral power distributions. By using this silent substitution method, it is possible to stimulate wanted photoreceptor type without creating response from the other (silenced) photoreceptors. Photoreceptor's response to a stimulus depends on the wavelength and the number of photons per unit area. Therefore, photoreceptors cannot separate if a stimulus is created from one individual light source or a combination of two or more light sources as long as the energy carried by the photons to create the response is the same (Estévez and Spekreijse, 1982). This is an especially useful way to target specific photoreceptor types when studying animal's response to certain, monochromatic visual cues without altering the retina. This method is widely used with human and mouse photoreceptor and melanopsin research (Zele *et al.*, 2018; Allen, Martial and Lucas, 2019), but has not yet been introduced to zebrafish studies.

**1.5 Aims of this PhD**

The first aim of this thesis is to characterize the spectral environment of zebrafish's natural habitats. As explained above, previous natural imaging research has mostly focused on filter cameras as the method to explain the light variation in naturalistic scenes. However, this approach has several problems by either being too expensive or missing relevant wavelengths for zebrafish. As a solution to these shortcomings, I introduce a new method for natural imaging: a self-made hyperspectral scanner. With this method I demonstrate the spectral variation in the natural habitats of zebrafish (*Danio rerio*) in North-East India and how well these spectral characteristics match with the colour vision abilities in the zebrafish larvae retina.

A second aim of this thesis is to demonstrate the relevance of UV part of the light spectrum in the prey capture behaviour. In previous research small, bright objects have been shown to initiate prey capture. I show for the first time how the UV cones create the most important channel to detect prey items (such as paramecia) while long wavelength sensitive red and green cones mostly ignore this information.

# *Chapter 2 –*

# *A low-cost hyperspectral scanner for natural imaging and the study of animal colour vision above and under water*

## 2.1 Abstract

Hyperspectral imaging is a widely used technology for industrial and scientific purposes, but the high cost and large size of commercial setups have made them impractical for most basic research. Here, we designed and implemented a fully open source and low-cost hyperspectral scanner based on a commercial spectrometer coupled to custom optical, mechanical and electronic components. We demonstrate our scanner's utility for natural imaging in both terrestrial and underwater environments. Our design provides sub-nm spectral resolution between 350-1000 nm, including the UV part of the light spectrum which has been mostly absent from commercial solutions and previous natural imaging studies. By comparing the full light spectra from natural scenes to the spectral sensitivity of animals, we show how our system can be used to identify subtle variations in chromatic details detectable by different species. In addition, we have created an open access database for hyperspectral datasets collected from natural scenes in the UK and India. Together with comprehensive online build- and use-instructions, our setup provides an inexpensive and customisable solution to gather and share hyperspectral imaging data.

## 2.2 Introduction

Hyperspectral imaging combines spatial and detailed spectral information of a scene to construct images where the full spectrum of light at each pixel is known (Goetz *et al.*, 1985). Commercial hyperspectral imaging technology is used, for example, in food industry (Gowen *et al.*, 2007; ElMasry, Sun and Allen, 2012), agriculture (Lelong, Pinet and Poilve, 1998; Monteiro *et al.*, 2007), astronomy (Goetz *et al.*, 1985) and low altitude aerial observations (Uto *et al.*, 2016a, 2016b). However, these devices typically are expensive, lack the ultraviolet (UV) part of the spectrum, or do not work under water. Moreover, many are bulky and must be attached to a plane or other heavy machinery, which makes them unsuitable for most basic research (but see Uto *et al.*, 2016a, 2016b). Here, we present a low-cost and open source hyperspectral scanner design and demonstrate its utility for studying animal colour vision in the context of the natural visual world.

Animals obtain sensory information that meets their specific needs to stay alive and to reproduce. For many animals, this requires telling wavelength independent from intensity– an ability widely referred to as colour vision (Baden and Osorio, 2018). To study what chromatic contrasts are available for an animal to see in nature requires measuring the spectral content of its environment (natural imaging) and comparing this to the eye's spectral sensitivity.

Most previous work on natural imaging to study animal colour vision used sets of spectrally narrow images generated by iteratively placing different interference filters within the range of 400-1,000 nm (Nagle and Osorio, 1993; Brelstafø *et al.*, 1995; Ruderman, Cronin and Chiao, 1998; Chiao, Cronin and Osorio, 2000) in front of a spectrally broad sensor array. So far, a major focus has been on our own trichromatic visual system that samples the short (blue "B"), medium (green "G") and long (red "R") wavelength ("human visible") range of the electromagnetic spectrum (Buchsbaum, G. & Gottschalk, 1983; Nagle and Osorio, 1993; Webster and Mollon, 1997; Ruderman, Cronin and Chiao, 1998; Lewis and Li, 2006). However, across animals the number and spectral sensitivity of retinal photoreceptor types varies widely. Perhaps most importantly, and unlike humans, many animals can see in the UV part of the spectrum, which has not been included in available hyperspectral measurements from terrestrial or underwater scenes. Johnsen et al. (2013, 2016) used an underwater hyperspectral imager (UHI) to map the seafloor in an effort to identify structures and objects with varying depth, but more shallow underwater habitats have not been studied in this way. Finally, in 2013 Baden et al. used a hyperspectral scanner based on a spectrometer reaching the UV spectrum of light and an optical fibre controlled by two servo motors. With their setup it is possible to build hyperspectral images in a similar way to the design presented here, but the system is bulky and fragile making it inconvenient to enclose in a waterproofed casing. In their setup the point of light from the scene is guided with the optic fibre attached to the spectrometer which further complicates the build. Our design instead uses mirrors to overcome these shortcomings.

Here, we designed and built a low-cost open source hyperspectral scanner from 3D printed parts, off-the-shelf electronic components and a commercial spectrometer that can take full spectrum (~350-950 nm), low spatial resolution (4.2° horizontal, 9.0° vertical) images above and under water. With our fully open design and instructions it is possible for researchers to build and modify their own hyperspectral scanners at substantially lower costs compared to commercial devices (~£1,500 for a spectrometer if unavailable, plus ~£113-340 for all additional components, compared to tens to hundreds of thousands for commercial alternatives). We demonstrate the performance of our system using example scans and show how this data can be used to study animal colour vision in the immediate context of their natural visual world. We provide all raw data of these and additional scans to populate a new public database of natural hyperspectral images measured in the UK and in India (https://zenodo.org/communities/hyperspectral-natural-imaging), to complement existing datasets (Párraga *et al.*, 1998; Foster *et al.*, 2006; Baden *et al.*, 2014). Complete build and

installation instructions are detailed in the manual on the project GitHub page: https://github.com/BadenLab/Hyperspectral-scanner (Appendix 1 in this thesis).

## 2.3 Methods

### *2.3.1 Hardware design*

The scanner (Fig. 2.1) is built around a trigger-enabled, commercial spectrometer (Thorlabs CCS200/M, advertised as 200-1,000 nm but effectively useful between 350 nm and 950 nm). A set of two movable UV reflecting mirrors (Thorlabs PFSQ10-03-F01 25.4 x 25.4 mm and PFSQ05-03-F01 12.7 x 12.7 mm) directs light from the scanned scene onto the spectrometer's vertically elongated slit (20 µm x 1.2 mm) via a 1 mm diameter round pinhole placed at 23 mm distance from the slit, giving an effective opening angle of ~2.5° (Figs. 2.1B-C and 2.3A, see also Baden et al. 2013). However, the effective resolution limit of the full system is ~4.2° (horizontal) and ~9.0° (vertical) (see results). To gradually assemble an image, an Arduino Uno microcontroller (www.Arduino.cc) iteratively moves the two mirrors via servo-motors along a pre-defined scan-path under serial control from a computer. At each new mirror position, the Arduino triggers the spectrometer via a transistor-transistor logic (TTL) pulse to take a single reading (Fig. 2.1D-E). An optional 9V battery powers the Arduino to relieve its universal serial bus (USB) power connection. The entire set-up is encased in a waterproofed housing fitted with a quartz-window (Thorlabs WG42012 50.8 mm UVFS Broadband Precision Window) to permit light to enter (Fig. 2.1A). For underwater measurements, optional diving weights can be added to control buoyancy. All internal mechanical components were designed using the freely available OpenSCAD (www.OpenScad.org) and 3D printed on an Ultimaker 2 3D printer running Cura 2.7.0 (Ultimaker). For detailed build instructions including all 3D files and Arduino control code, see the project's GitHub page at https://github.com/BadenLab/Hyperspectral-scanner.

### *2.3.2 Scan-paths*

Four scan paths are pre-programmed onto the Arduino control code: a 100-point raster at 6° x- and y-spacing (60° x 60°), and three paths with spirals covering an $r$ = ±30° area with equally spaced 300, 600 or 1,000 points, respectively (Fig. 2.2). To generate spirals, we computed $n$ points of a Fermat's spiral:

$$r = \sqrt{\theta \times n}$$

$$\theta = \pi\left(3 - \sqrt{5}\right)$$

where $r$ is the radius and $\theta$, in radians, is the "golden angle" (~137.5°). Next, we sorted points by angle from the origin and thereafter ran a custom algorithm to minimise total path length. For this, we iteratively and randomly exchanged two scan positions and calculated total path length. Exchanges were kept if they resulted in path shortening but rejected in all other cases. Running this algorithm for $10^5$ iterations resulted in the semi-scrambled scan paths shown in Figure 2.2.

When choosing a suitable scan-path for a given application, it is important to weigh sampling density (and thus scan-time) against achievable resolution. The effective field of view (FOV) and thus resolution of the scanner is ~4.2° x ~9.0° (see results). In comparison, the pre-defined 300, 600 and 1,000 point spiral scan paths offer regular inter-point-spacings of 3.1°, 2.1° and 1.6°, respectively. Accordingly, the 1,000 point spiral (Fig. 2.2D) oversamples the image in both the horizontal and vertical dimension (i.e. both the X and Y dimensions of the scanner's FOV exceed the scans' inter-point spacings by a factor of 2). The 600 point spiral (Fig. 2.2C) also oversamples vertically, but horizontally is well matched to the scanner's effective resolution. Finally, the 300 point spiral (Fig. 2.2B) undersamples horizontally but still oversamples vertically. In comparison, the 100-point rectangle scan (Fig. 2.2A, spacing of 6° along cardinal and 8.5° along obtuse angles, respectively) under samples in both dimensions and is therefore more suited for rapid "test-scans". Another advantage of the round spiral scan paths is that they are matched to the scanner's circular window. Overall, substantial oversampling can be desirable as it allows averaging out "noise" or movement in the scene in post-processing. Notably, the scanner can also be used standing on its side, thus effectively swapping the vertical and horizontal resolution limits.

Alternative scan-paths, such as higher-density rectangle-scans, a honeycomb pattern to compromise regular sampling density and regularity, or one that acknowledges the asymmetry of horizontal and vertical resolution, can be easily implemented by the user. Details on how to execute the pre-programmed scan modes and how to alter them are included in the manual: https://github.com/BadenLab/Hyperspectral-scanner.

A

B

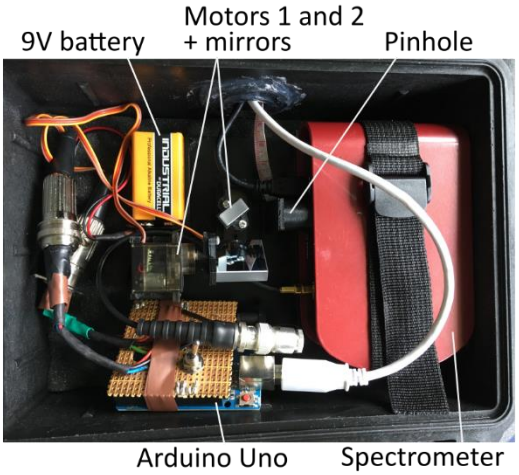
9V battery
Motors 1 and 2
+ mirrors
Pinhole
Arduino Uno
Spectrometer

C

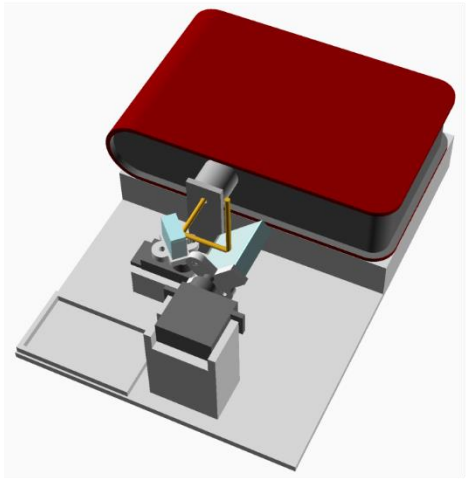

D

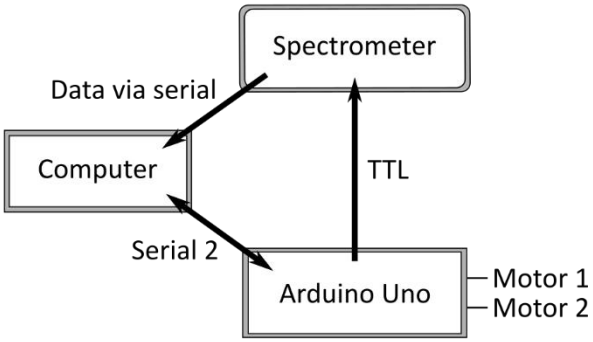
Spectrometer
Data via serial
Computer
TTL
Serial 2
Arduino Uno
Motor 1
Motor 2

E

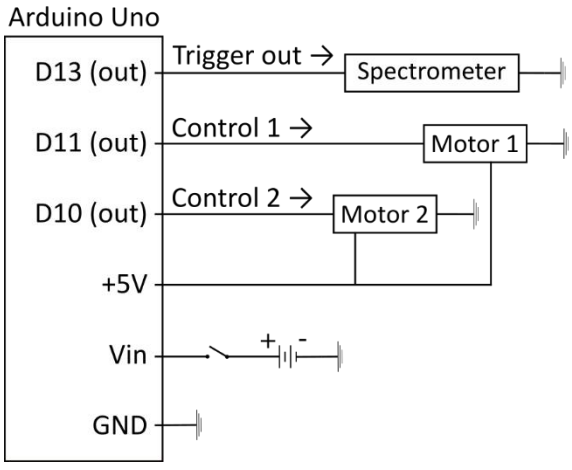
Arduino Uno
D13 (out)
Trigger out →
Spectrometer
D11 (out)
Control 1 →
Motor 1
D10 (out)
Control 2 →
Motor 2
+5V
Vin
+
-
GND

**Figure 2.1 (previous page).** A Hyperspectral scanner for low-cost natural imaging. **(A)** The waterproof casing with a window (white asterisk) for light to enter. The PVC tube on top protects the cables to the computer. **(B)** Internal arrangement of parts: the spectrometer, Arduino Uno microcontroller, 9V battery, two servo motors (Motors 1 and 2) with mirrors attached to them and a round pinhole ($r$ = 0.5 mm). **(C)** A schematic illustration of the optical path (Arduino, 9V battery and chords are left out for clarity). First, light beam (yellow lines) enters the system from above through the window. Light reaches first the larger mirror underneath the window of the casing, reflects to the smaller mirror and from there through the pinhole to the spectrometer's slit. The pinhole is placed at 23 mm distance from the slit (20 µm x 1.2 mm effective slit dimension). Light deflected off the first mirror is partly shadowed by the edges of the casing, which creates dark stripes at the horizontal edges of the scanned images when the box is closed. These edges are cropped in the presented example scans (Figs. 2.3 and 2.8). Spectral filtering by the quartz window was corrected for in postprocessing (Figs. 2.3D-E). **(D)** Operational logic. The scanning path is uploaded to the Arduino from the computer via Serial 2 connection to define the motor movements. After each movement the spectrophotometer is triggered via TTL to take a measurement and send the data to the computer vial serial. The ongoing state of the scanning path is fed from the control circuit to the computer. **(E)** Circuit diagram.

### *2.3.3 Data collection*

All recordings shown in this work used the 1,000-point spiral. Acquisition time for each scan was 4-6 minutes, depending on the time set for each mirror movement (260-500 ms) and the spectrometer's integration time (100-200 ms). These were adjusted based on the amount of light available in the environment to yield an approximately constant signal-to-noise ratio (SNR) between scans. In all cases, the scanner was supported using a hard-plastic box to maintain an upright position. All outdoor scans were taken in sunny weather with a clear sky. For details of the underwater measurement done in West Bengal India, see Zimmermann, Nevala, Yoshimatsu et al., 2018. In addition, we took a 180° RGB colour photograph of each scanned scene with an action camera (Campark ACT80 3K 360°) or a ~120° photograph with an ELP megapixel Super Mini 720p USB Camera Module.

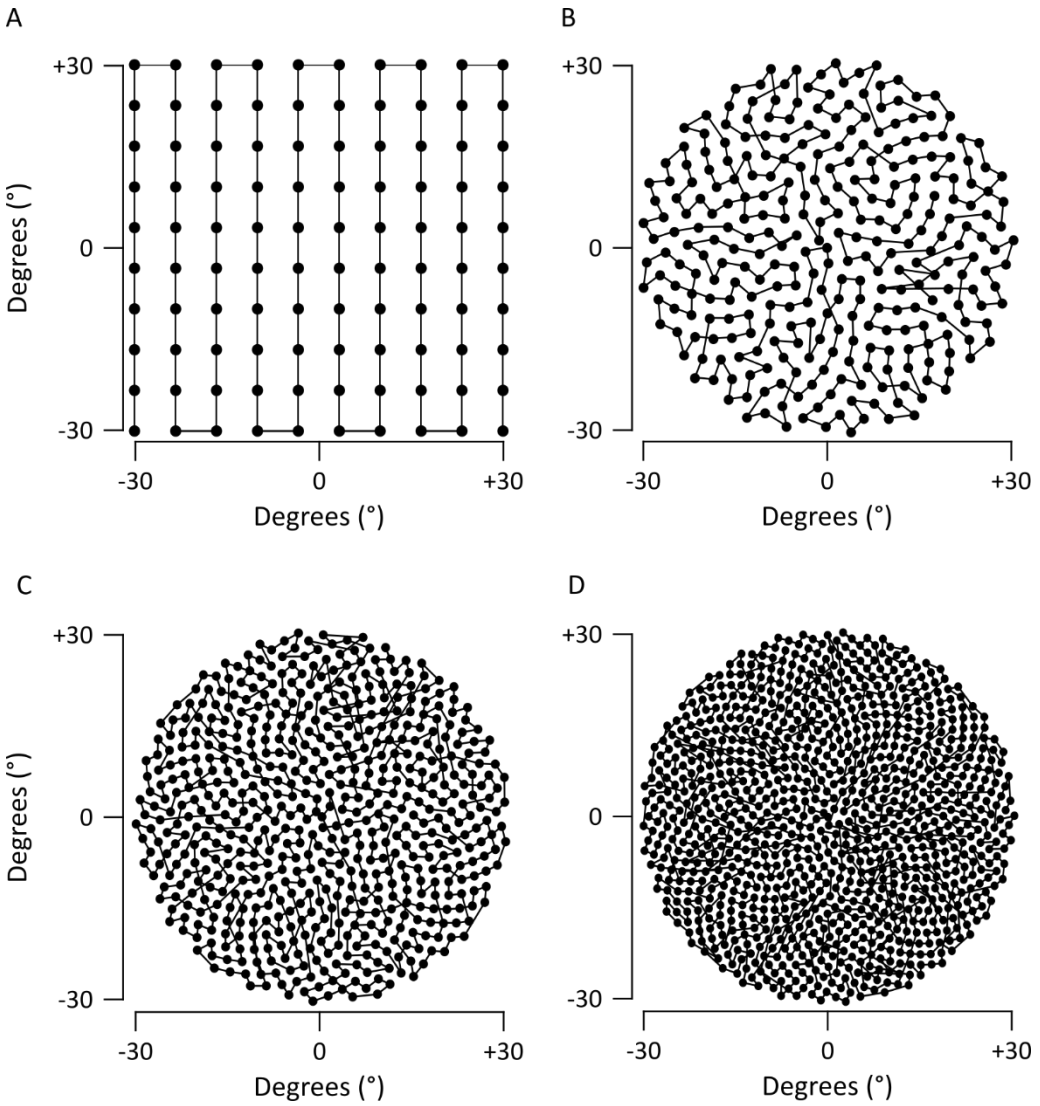


**Figure 2.2.** Four scanning paths created with the Fermat's spiral across the 60° area. **(A)** 100 points square, **(B)** 300 points spiral **(C)** 600 points spiral **(D)** 1000 points spiral.

*2.3.4 Data analysis*

The spectrometer was used with the factory-set spectral pre-compensation to ensure that readings are as accurate as possible across the full spectral range. This factory calibration was done with the optic fibre; however, our system gathers light through a quartz window and two mirrors without an optic fibre (Figs. 2.1A-C). We measured the additional spectral transfer function required to correct our data (Figs. 2.3D-E) and applied this curve to all measurements throughout this work. To obtain this transfer function, we pointed the spectrometer at the mid-day sun (a bright and spectrally broad light source) and took 100 readings each through the optic fibre (as factory calibrated), and then without the fibre but instead passing through the scanner's

full optical path. The transfer function shown is the dividend of the mean from each of these recordings:

Let $\overrightarrow{e_i} = (0, \dots, 0, 1, 0, \dots, 0)$ where the $i^{th}$ entry is 1, then

$$\vec{a}(\lambda) = \sum_{i=1}^{200-1000} b_i(\lambda) c_i(\lambda)^{-1} \vec{e}_i$$

Where *a*(x) is the transfer function and *b* and *c* the spectra taken through the full scanner and via the optic fibre, respectively. The inverse of this transfer function was applied to all subsequent spectra taken with the scanner. All data was analysed using custom scripts written in IGOR Pro 7 (Wavemetrics) and Fiji (NIH). To visualise scanned images, we calculated the effective brightness of each individual spectrum (hereafter referred to as "pixel") as sampled by different animals' opsin templates. In each case, we z-normalised each channel's output across an entire scan and mapped the resultant brightness map to 16-bit greyscale or false-colour coded maps, in each case with zero centred at $2^{15}$ and range to 0 and to $2^{16}$-1. We then mapped each pixel onto the 2D plane using a standard fish-eye projection. To map each spiral scan into a bitmap image, we scaled a blank 150x150 target vector to ±30° (same as the scanner range), mapped each of *n* scanner pixels to its nearest position in this target vector to yield *n* seed-pixels, and linearly interpolated between seed-pixels to give the final image. The 150 x 150 pixel (60 x 60 degrees) target vector was truncated beyond 30° from the centre to cut the corners which comprised no data points. We also created hyperspectral videos by adding a 3rd dimension so that each pixel in the 150 x 150 target vector holds a full spectrum. This way each video is constructed from 800 individual images where one frame equals to 1 nm window starting from 200 nm.

*2.3.5 Principal component analysis*

For principal component analysis (PCA), we always projected across the chromatic dimension (e.g. human trichromatic image would use 3 basis vectors, "red", "green" and "blue") after z-normalising each vector.

## 2.4 Results

The scanner with water-proofed casing, its inner workings and control logic are illustrated in Figure 2.1. Light from the to-be-imaged scene enters the box through the quartz window (Fig. 2.1A) and reflects off the larger and then the smaller mirror, passing through a pinhole to illuminate the active part of the spectrometer (Figs. 2.1B-C). To scan a scene, an Arduino script is started via serial command from a computer to iteratively move the two mirrors through a pre-defined scan path (Methods, Fig. 2.2 and Supplementary Video 1 available online). At each scan-position, the mirrors briefly wait while the spectrometer is triggered to take a single reading. All instructions for building the scanner, including 3D part models and the microcontroller control code are provided at the project's GitHub page at https://github.com/BadenLab/Hyperspectral-scanner.

### *2.4.1 Scanner performance*

In our scanner design, several factors contribute to the spatial resolution limit of the complete system. These include spacing of the individual scan-points (discussed in methods), angular precision of the servo-motors, the effective angular size of the pinhole in two dimensions, the optical properties of the mirrors and the quartz window as well as the dimensions of the spectrometer's slit. To therefore establish the scanner's effective spatial resolution, we first determined a single "pixel's" effective field of view (FOV). For this, we statically pointed the scanner at a PC screen and presented individual 5° white squares on a black background in all of 5x5 positions of a grid pattern, and each time noted the total signal power recorded by the spectrometer. This revealed that this FOV is vertically elongated, likely due to the spectrometer's vertically oriented slid (Fig. 2.3A). To determine how this elongated FOV impacts spatial resolution in an actual scanned scene, we scanned a printout of a 3.8° width white cross on a black background in the mid-day sun using a 1,000-point spiral (Figs. 2.2D, 2.3B-C) and compared the result to the original scene (Figs. 2.3B-C). The difference between the horizontal profile across the cross' vertical arm and the original scene approximately equated to a Gaussian blur of 2.1° standard deviation. This effectively translates to ~4.2° as the finest detail the scanner can reliably resolve along the horizontal axis under these light conditions. Vertically, this blur was about twice that (~9.0°), in line with the vertically elongated FOV. While this spatial resolution falls far behind even the simplest commercial digital camera systems, our scanner instead provides 600 nm spectral range at sub-nm resolution that can be used to identify fine spectral details in the scanned scene.

To illustrate the scanner's spectral resolution, we took a 1,000-point scan in the mid-day sun of a blue door and red brick wall (Fig. 2.3F) and reconstructed the scene based on human red, green and blue opsin templates (Stockman and Sharpe, 2000) to assemble an RGB image (Methods, Fig. 2.3F). From this scan, we then picked two individual "pixels" (blue and red dots) and extracted their full spectra (Fig. 2.3G). Next, we illustrate the function with examples from terrestrial and underwater scenes.

### *2.4.2 Natural imaging and animal colour vision*

The ability to take high-spectral resolution images is useful for many applications, including food quality controls (Gowen *et al.*, 2007; ElMasry, Sun and Allen, 2012), agricultural monitoring (Lelong, Pinet and Poilve, 1998; Monteiro *et al.*, 2007) and surface material identification from space (Goetz *et al.*, 1985). Another possibility is to study the spectral information available for colour vision by different animals. Here, our portable, waterproofed and low-cost hyperspectral scanner reaching into the UV range allows studying the light environment animals live in. To illustrate what can be achieved in this field, we showcase scans of three different scenes: a forest scene from Brighton, UK (Figs. 2.4-2.6), a close-up scan of a flowering cactus (Fig. 2.7) and an underwater river scene from West Bengal, India (Fig. 2.8). In each case, the estimated 60° field of view covered by the scanner is indicated in the accompanying widefield photos (Figs. 2.4A, 2.5A, 2.7A, 2.8A). To showcase chromatic contrasts available for colour vision by different animals in these scenes, we reconstructed the forest and cactus data with mouse (*Mus musculus*), human (*Homo sapiens*), bee (*Apis melifera*), butterfly (*Graphium sarpedon*), chicken (*Gallus gallus domesticus*) and zebra finch (*Taeniopygia guttata*) spectral sensitivities (Figs. 2.6B, 2.7C). The underwater scan was reconstructed based on zebrafish (*Danio rerio*) spectral sensitivity (Fig. 2.8B) (Jacobs, Neitz and Deegan, 1991; Peitsch *et al.*, 1992; Stockman and Sharpe, 2000; Chinen *et al.*, 2003; Allison *et al.*, 2004; Toomey *et al.*, 2016). In addition, we provide hyperspectral movies between 200 and 1,000 nm for these three scenes, where each frame is a 1 nm instance of the scanned scene (Supplementary Videos 2-4 available online). These videos illustrate how different structures in the scene appear at different wavelengths.

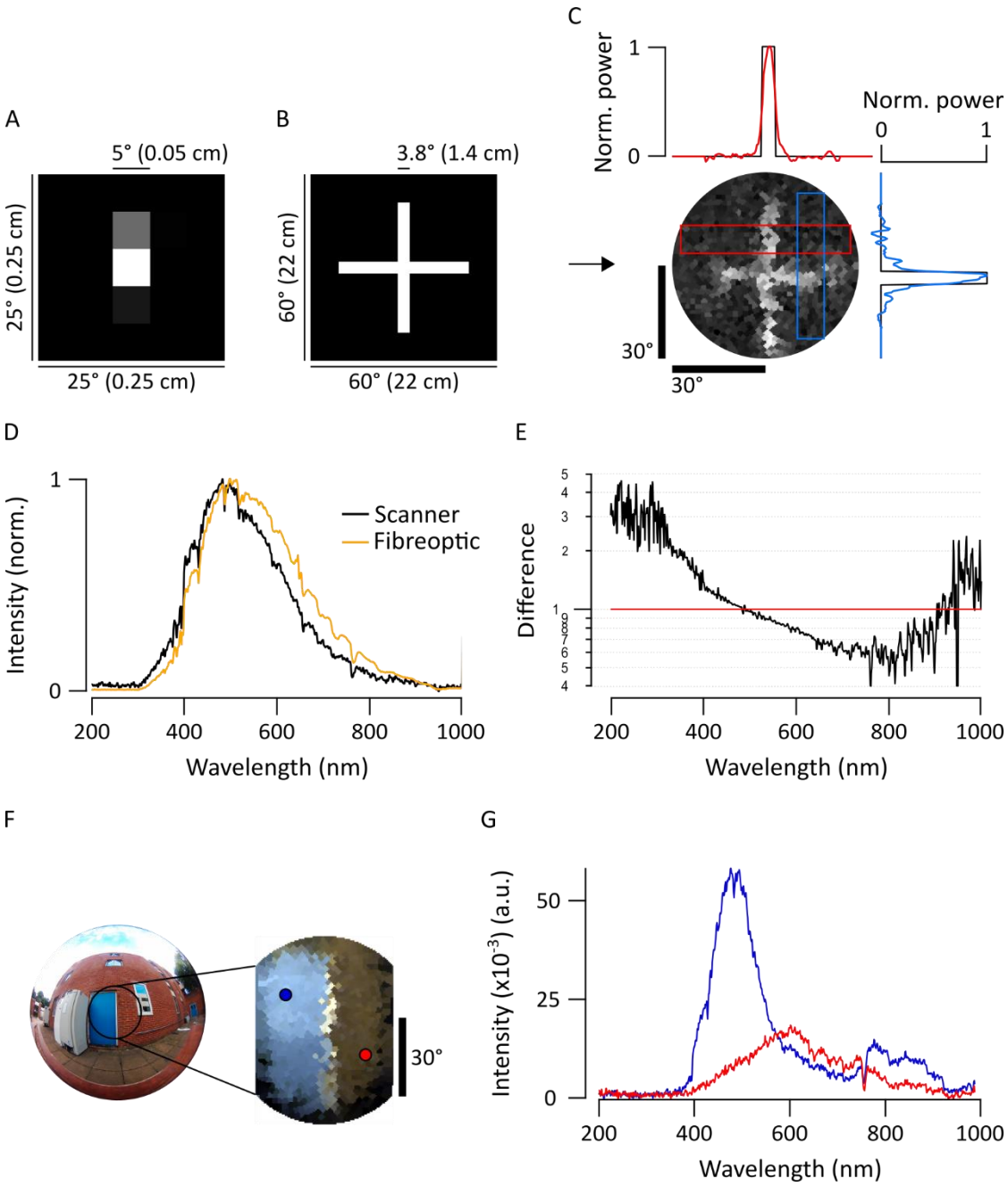


**Figure 2.3.** Scanner performance. **(A)** Single pixel field of view (FOV) is vertically elongated as determined by spot-mapping. **(B-C)** A printout of a 3.8° white cross on a black background (B) was scanned with a 1,000 point spiral scanning path (Fig. 2.2D) to estimate the scanner's spatial resolution. In (C), power (red and blue lines in the graphs) represents brightness profiles across the cross' arms as indicated, superimposed on the original profile (black). **(D)** Spectrometer readings of a clear daylight sky taken through the spectrometer's fibreoptic (orange) and through the complete optical path of the scanner (black, i.e. 2 mirrors and a quartz window, though lacking the fibreoptic). When purchased, the spectrometer is calibrated with the fibreoptic attached. Accordingly, we computed the corresponding correction curve and applied it to all scanner data presented throughout this work **(E)**. **(F)** An action camera picture of the blue door + red brick wall measured outdoors and an RGB representation image of the scan when using opsin templates from human spectral sensitivity. Blue and red dots in the RGB representation refer to the two points used to show examples of individual spectra in **(G)**.

First, we used the data from the forest scene scan to compute how a trichromat human with three opsins (red, green and blue) might see it (Fig. 2.4). To this end, we multiplied the spectra from each "pixel" with the spectral sensitivity of each of the three corresponding opsins templates to create "opsin activation maps" (red "R", green "G" and blue "B", Fig. 2.4A, Methods), hereafter referred to as "channels". These false-colour coded, monochromatic images show the luminance driving each opsin across the scene. In this example, the R- and G-channels clearly highlight the dark band of trees in the middle of the scene with varying light and dark structures in the sky and on the ground. However, the B-channel shows mainly structures from the sky but provides low contrast on the ground. To illustrate how these channels can be used for our sense of colour vision, we combined them into an RGB image (Fig. 2.4A, right).

Next, we used principal component analysis (PCA) to highlight spectral structure in the data. When using PCA on natural images it is common to compute across the spatial dimension (Hancock, Baddeley and Smith, 1992; Ruderman, Cronin and Chiao, 1998), however we computed across the spectral dimension (i.e. the individual measurement points in 3-dimensional RGB space) by using the R-, G- and B-channels as 3 basis vectors (Figs. 2.4B-C). This way the concept of PCA was same as in the previous studies, but only the dimension of the data was changed. In natural scenes, most variance is driven by changes in overall luminance rather than chromatic contrasts (Ruderman, Cronin and Chiao, 1998; Chiao, Cronin and Osorio, 2000; Lewis and Li, 2006). In this type of data, the first principal component (PC1) therefore reliably extracts the achromatic (greyscale) image content. From here it follows that all subsequent principal components (PC2-n) must describe the chromatic axes in the image, in decreasing order of importance. For simplicity, we hereafter refer to PC1 as the achromatic axis and PC2, PC3 and (where applicable) PC4 as first, second and third chromatic axes, respectively ($C_{1, 2, 3}$). When applied to the example scan of the forest scene with human spectral sensitivity, the achromatic image with near equal loadings across the R-, G- and B-channels accounted for majority (97.7%) of the total image variance (Figs. 2.4D-F), in agreement with previous work (Ruderman, Cronin and Chiao, 1998; Chiao, Cronin and Osorio, 2000; Lewis and Li, 2006). This left 2.3% total variance for the first and second chromatic axes $C_1$ and $C_2$ (Table 2.1). In line with Ruderman et al. (1998), the chromatic contrasts emerging from PCA were R+G against B ($C_1$, long- vs short-wavelength opponency) and R against G while effectively ignoring B ($C_2$, Fig. 2.4E). These two chromatic axes predicted from the hyperspectral image matched the main chromatic comparisons performed by the human visual system ("blue vs. yellow" and "red vs. green"). To show where in the image different chromatic contrasts exist across space, and to facilitate visual

comparison between animals, we also mapped the chromatic axes into an RGB image such that R displays $C_1$, G $C_2$ and B $C_3$. Since the trichromat human can only compute two orthogonal chromatic axes (nOpsins – 1), $C_3$ was set to $2^{15}$ (i.e. the mid-point in 16-bit) in this example. These PC-based RGB images ignore the brightness variations of the achromatic channel, therefore describing only chromatic information in a scene. This specific projection allows a trichromat human observer viewing an RGB-enabled screen or printout to judge where in a scanned scene an animal might detect dominant chromatic contrasts, even if that animal uses more than three spectral cone types for colour vision. The power of this approach can be illustrated when considering non-human colour vision based on the same dataset.

Unlike humans, many animals use the ultraviolet (UV) part of the spectrum for vision (Hunt *et al.*, 2001; Siebeck, 2013). To illustrate how the addition of UV-channel can change available chromatic information, we next performed the same analysis for a tetrachromatic zebra finch (Fig. 2.5). This bird uses four, approximately equi-spaced opsins (red, green, blue and UV), which in addition are spectrally sharpened with oil droplets (Toomey *et al.*, 2016). As before, the monochromatic opsin-channels (RGB and "U" for UV, Fig. 2.5A) appeared with R- and G-channels showing structures both in the sky and on the ground while B- and U-channels mainly highlighted the sky. We next computed the principal components across the now four opsin channels (Figs. 2.5B-F).

This time the achromatic axis explained only 92.5% of the total variance leaving 7.5% for chromatic comparisons, which now comprised three chromatic axes ($C_{1\text{-}3}$, Table 2.1). As with humans, the most important chromatic axis compared long- and short-wavelength channels ($C_1$, R+G against B+U, single zero crossing in Fig. 2.5E). $C_2$ was also similar to the human version by comparing R- and G-channels, but in addition paired the R-channel with the UV and the G-channel with the blue (two zero crossings). While the spatial structure highlighted by $C_1$ was similar to that of the human, $C_2$ picked up additional details from the ground (Fig. 2.5D). Finally, $C_3$ (R+B against G+U) highlighted additional structures in the scene that are largely invisible to the human observer.

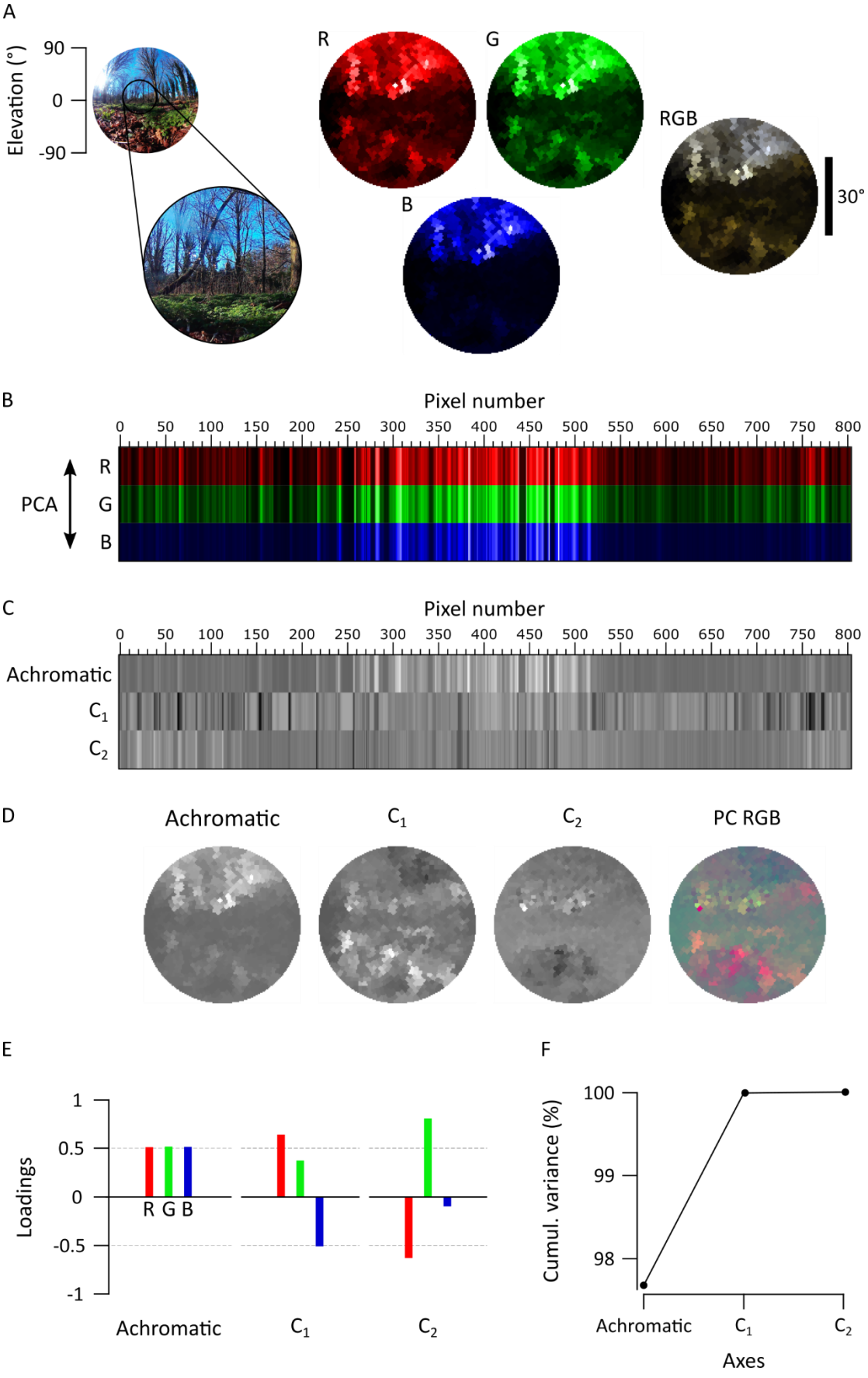
A
Elevation (°)
90
0
-90
R
G
B
RGB
30°
B
Pixel number
0 50 100 150 200 250 300 350 400 450 500 550 600 650 700 750 800
PCA
R
G
B
C
Pixel number
0 50 100 150 200 250 300 350 400 450 500 550 600 650 700 750 800
Achromatic
C1
C2
D
Achromatic
C1
C2
PC RGB
E
Loadings
1
0.5
0
-0.5
-1
R G B
Achromatic
C1
C2
F
Cumul. variance (%)
100
99
98
Achromatic
C1
C2
Axes

**Figure 2.4 (previous page).** An example data set of the forest scene with human spectral sensitivity. **(A)** A 180° photo of the forest scene with an approximate 60° scanner covered area (left). On the right, monochromatic R-, G- and B-channels were constructed from the scanned data by multiplying spectra from each pixel with the opsin templates (see Figs. 2.5B, 2.6C). The RGB image shows the reconstruction built based on the opsin channels. The different colour appearance of this RGB reconstruction compared to the photograph is due to the photograph representing long, middle and short wavelengths tuned for human spectral sensitivity presented as an RGB image. **(B)** Pixels from the R-, G- and B-channels aligned in the order of the measurement with an arrow on the right indicating the direction of the principal component analysis (PCA) across the measurement points. **(C)** Achromatic and chromatic axes $C_{1\text{-}2}$ aligned in the same order as in the previous image, and then reconstructed back to images in **(D)** to add the spatial information. The RGB image shows $C_1$ in red and $C_2$ in green (blue set to constant brightness). **(E)** Loadings from achromatic and chromatic axes, bars illustrating the amount of input from each opsin channel. **(F)** The cumulative variance explained (%) for each axis.

| | Variance explained by chromatic axes $C_{1\text{-}n}$ (%) | |
|---|---|---|
| | Forest (Fig. 2.6) | Cactus (Fig. 2.7) |
| Mouse | 2.6 | 8 |
| Human | 2.3 | 1.4 |
| Bee | 3.9 | 8.1 |
| Butterfly | 3.8 | 3.8 |
| Chicken | 6.7 | 2.9 |
| Zebra finch | 7.5 | 6.5 |

**Table 2.1.** The total variance explained by chromatic axes $C_{1\text{-}n}$ in the forest and cactus scans. An animal's opsin complement dictates discernible chromatic contrasts.

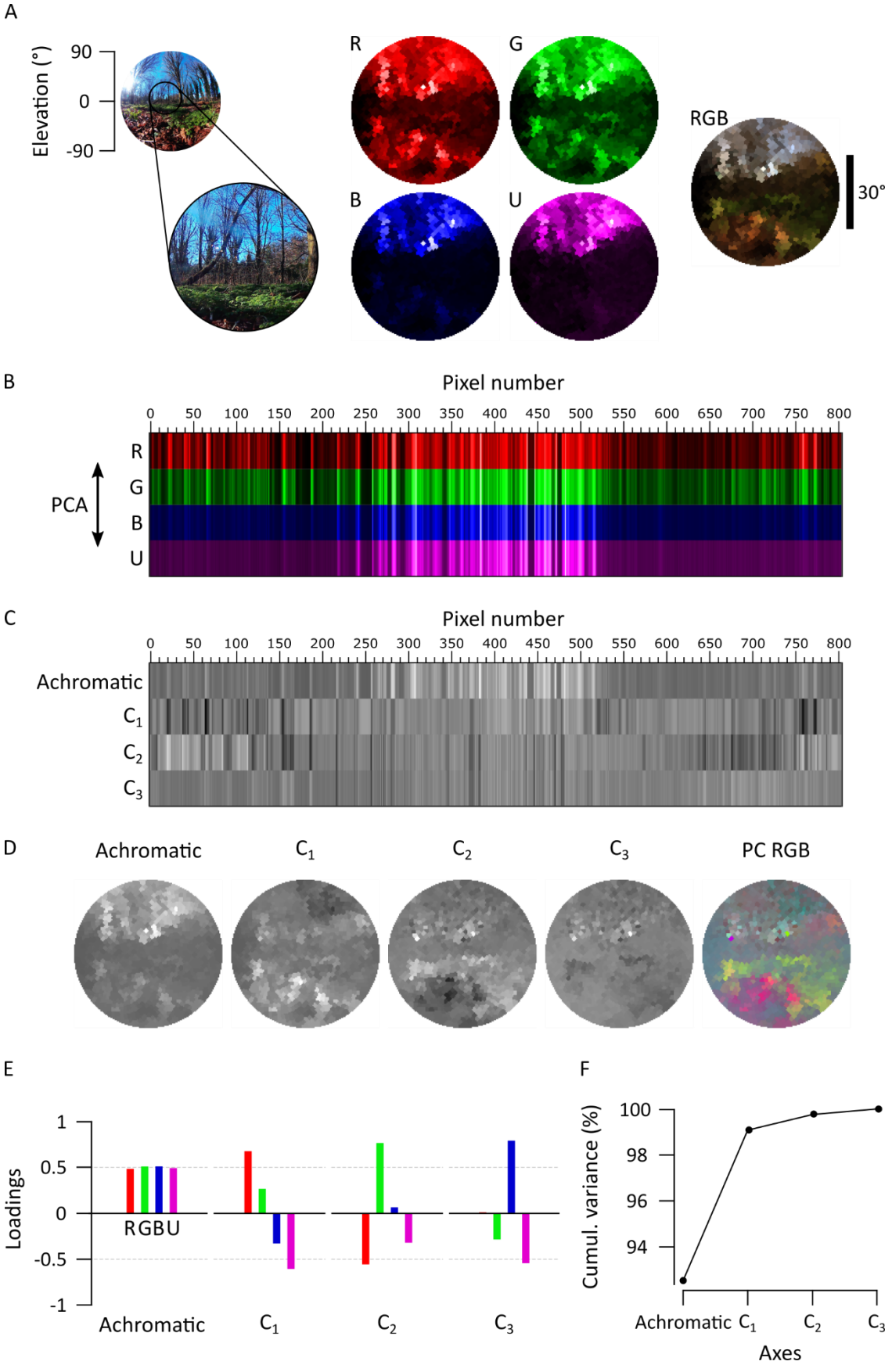
A
Elevation (°)
90
0
-90
R
G
B
U
RGB
30°
B
Pixel number
0 50 100 150 200 250 300 350 400 450 500 550 600 650 700 750 800
PCA
R
G
B
U
C
Pixel number
0 50 100 150 200 250 300 350 400 450 500 550 600 650 700 750 800
Achromatic
C1
C2
C3
D
Achromatic
C1
C2
C3
PC RGB
E
Loadings
1
0.5
0
-0.5
-1
RGBU
Achromatic
C1
C2
C3
F
Cumul. variance (%)
100
98
96
94
Achromatic C1 C2 C3
Axes

**Figure 2.5 (previous page).** The forest scene with zebra finch spectral sensitivity. **(A)** A still image of the forest scene with the approximated 60° scanner covered area, monochromatic opsin channels (R, G, B, U) and an RGB reconstruction where R is shown as red, G as green and B+U as blue. **(B-F)** As in Figure 2.3, with an addition of the UV channel (U) in all images. The RGB image in (D) displays $C_1$ in red, $C_2$ in green and $C_3$ in blue.

To further survey how an animal's opsin complement can affect the way chromatic details are detectable in complex scenes, we compared data from the forest scene (Fig. 2.6) to a close-up scan of a flowering cactus (Fig. 2.7) and filtered each using different animals' spectral sensitivities: a dichromat mouse, a trichromat human and bee and a tetrachromat butterfly, chicken and zebra finch. In these scenes, the order of the chromatic axes was largely stable across opsin complements used (PC1 – achromatic, $C_1$ – long vs short wavelengths, $C_2$ – R+U vs G+B, $C_3$ – R+B vs G+U), and here we only show the achromatic and $C_{1\text{-}3}$ reconstructions alongside the PC RGB images (Figs. 2.6A and 2.7B) next to the spectral sensitivity of each animal (Figs. 2.6B and 2.7C). In each case, the number of chromatic channels shown corresponds to the number of an animal's cone types minus 1.

The chromatic axes usable by different animals revealed diverse spatio-chromatic structures from both scenes (Figs. 2.6 and 2.7). Across all animals compared, while $C_1$ still reliably highlighted a long- vs. short-wavelength axis, the exact image content picked up along $C_{1\text{-}n}$ varied between opsin complements (Figs. 2.6A and 2.7B). For example, in the cactus scene the $C_1$ for the chicken highlighted spatial structures in the image that other animals instead picked up with $C_2$. A similar difference was also seen in the forest scene, where $C_2$ and $C_3$ in butterfly showed structures that were captured in the inverse order in the chicken and zebra finch (Fig. 2.6A). In addition, humans and butterflies had more consistent arrangement and structures in chromatic axes between each other than with other animals, possibly due to their similarly overlapping spectral sensitivities of the green and red cones.

For all animals in both scenes, the achromatic image content captured at least 91.9% of the total variance, leaving 1.4-8.1% for the chromatic axes (Table 2.1). For the forest scene, the addition of opsin-channels increased the amount of variance explained by the chromatic axes, and in particular for animals with widely spaced spectral channels (e.g. with chicken and butterfly, Table 2.1). In general, more chromatic details was discerned with more cones, especially when these cones had low-overlap spectral sensitivities covering a wide range of the natural light spectrum (e.g. from around 350 nm to over 600 nm as with zebra finch). Moreover, spectral sharpening of the opsin peaks through the addition of oil droplets (chicken and zebra finch) brought out further details and higher chromatic contrasts in the scanned scene. The order of

importance for the chromatic axes that optimally decompose scans depended strongly on the set of input vectors – the spectral shape and position of the animal's opsins.

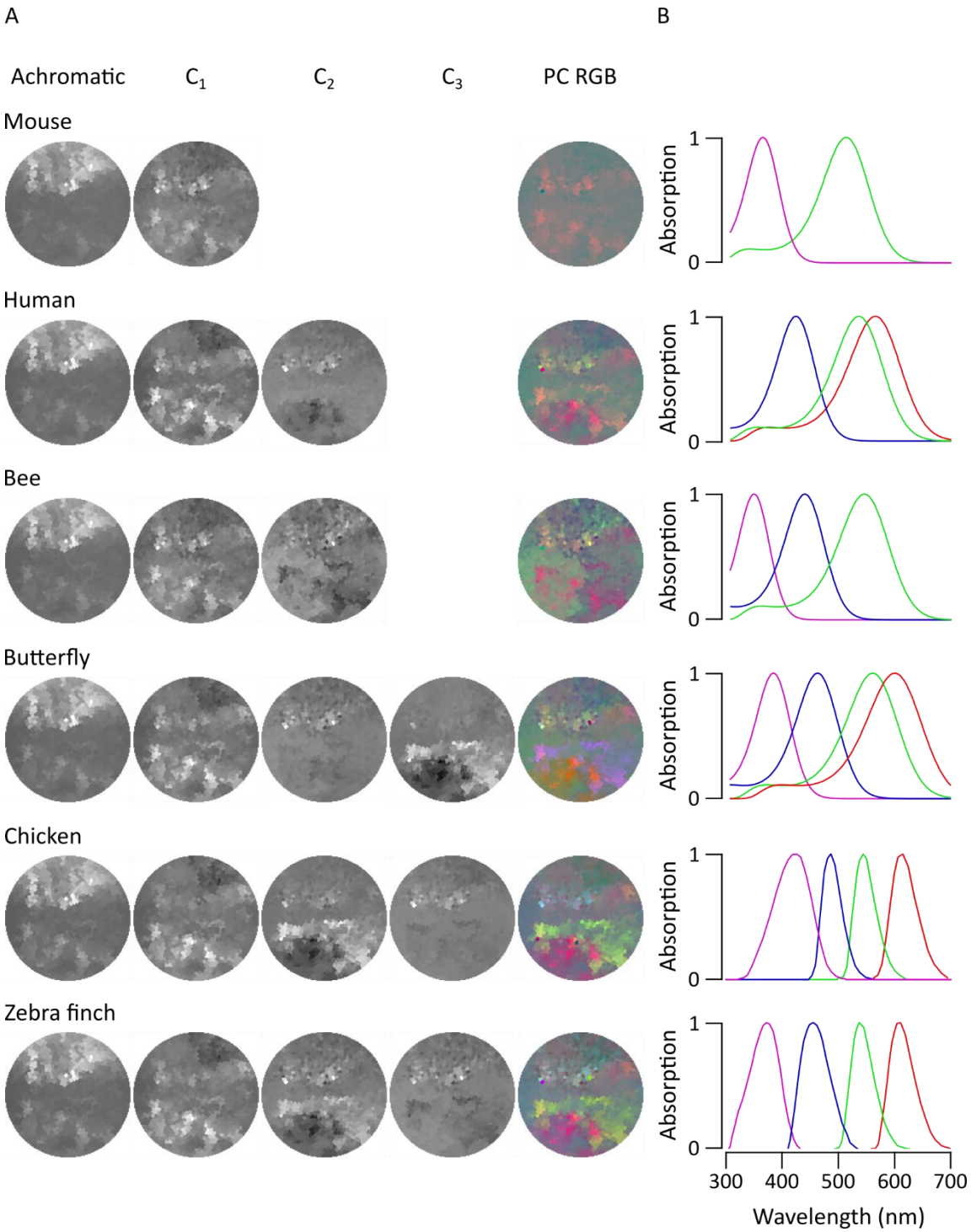

**Figure 2.6 (previous page).** PC reconstructions of the forest scene. **(A)** Achromatic and chromatic PCA reconstructions from the forest scene data for a mouse (*Mus musculus*), a human (*Homo sapiens*), a bee (*Apis melifera*), a butterfly (*Graphium sarpedon*), a chicken (*Gallus gallus domesticus*) and a zebra finch (*Taeniopygia guttata*) and PC RGB pictures. The number of chromatic axes equals to the number of cone types minus 1. Again, the PC RGB picture is constructed from chromatic axes $C_{1\text{-}n}$. In PC RGB, the $C_1$ is shown as red, $C_2$ as green and $C_3$ as blue. **(B)** Visual pigment absorption curves showing the spectral sensitivity of the cones for each animal. The pink, blue, green and red curves correspond to UV, blue, green and red sensitive opsins, respectively.

### *2.4.3 Hyperspectral imaging under water*

As light travels through the water column, water and dissolved particles absorb both extremes of the light spectrum making it more monochromatic with increasing depth (Morris *et al.*, 1995; Chiao, Cronin and Osorio, 2000). Mainly because of this filtering and scattering, underwater light environments have spectral characteristics that differ strongly from terrestrial scenes. To illustrate one example from this underwater world, we show a scan from a shallow freshwater river scene (Fig. 2.8A) taken in the natural habitat of zebrafish (*Danio rerio*) in West Bengal, India (Zimmermann *et al.*, 2018). The data was analysed based on the spectral sensitivity of the tetrachromatic zebrafish with red, green, blue and UV sensitive cones (Fig. 2.8B) (Hunt *et al.*, 2001; Allison *et al.*, 2004). In this example, the monochromatic R-, G-, and B-channels picked up different dominant spatial structures in the scene, while the U channel appeared more “blurry” with only small intensity differences around the horizon (Fig. 2.8C). Here, the total variance explained by the chromatic axes $C_{1\text{-}3}$ (14.7%, Fig. 2.8F) was higher compared to the two terrestrial scenes. $C_1$ compared long (R+G) and short (B+U) wavelengths between upper and lower parts of the scene (Figs. 2.8D-E) that arose from spectral filtering under water. Finally, $C_2$ and $C_3$ brought out further details that probably correspond to pieces of the imaged vegetation.

### *2.4.4 An open database for natural imaging*

Based on these and other additional scans above and under water from around the world (for example, see Zimmermann et al., 2018) we created an open access database online (https://zenodo.org/communities/hyperspectral-natural-imaging). All measurements in the database are taken with the hyperspectral scanner as described here.

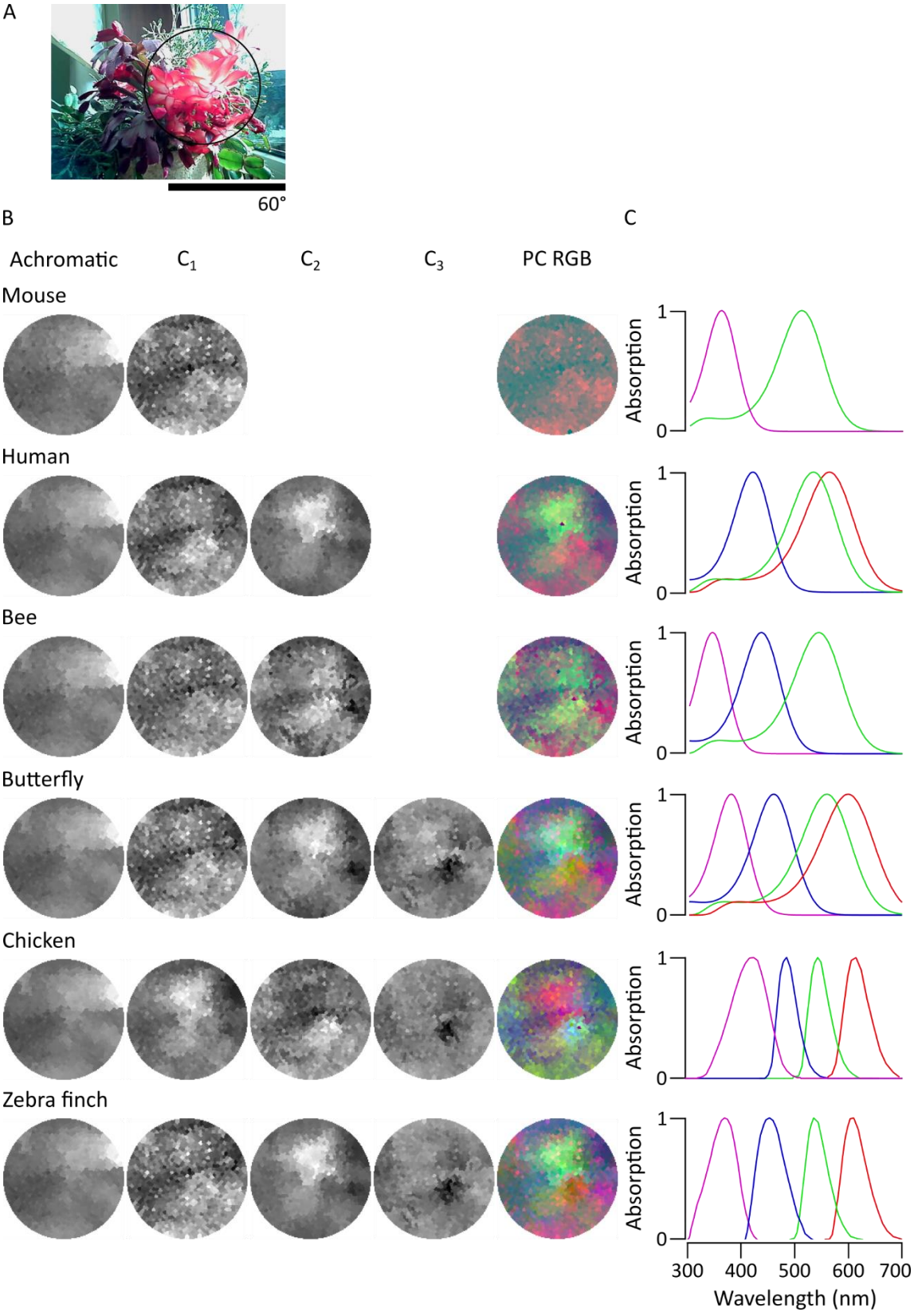


**Figure 2.7.** PC reconstructions of the flowering cactus. **(A)** A 120° photo of the scanned scene with a flowering cactus and the approximate 60° window (black circle) the scanner can cover. **(B)** Reconstructions for the chromatic axes $C_{1\text{-}n}$ and PC RGB images and **(C)** the absorption curves for each animal as in Figure 2.6B.

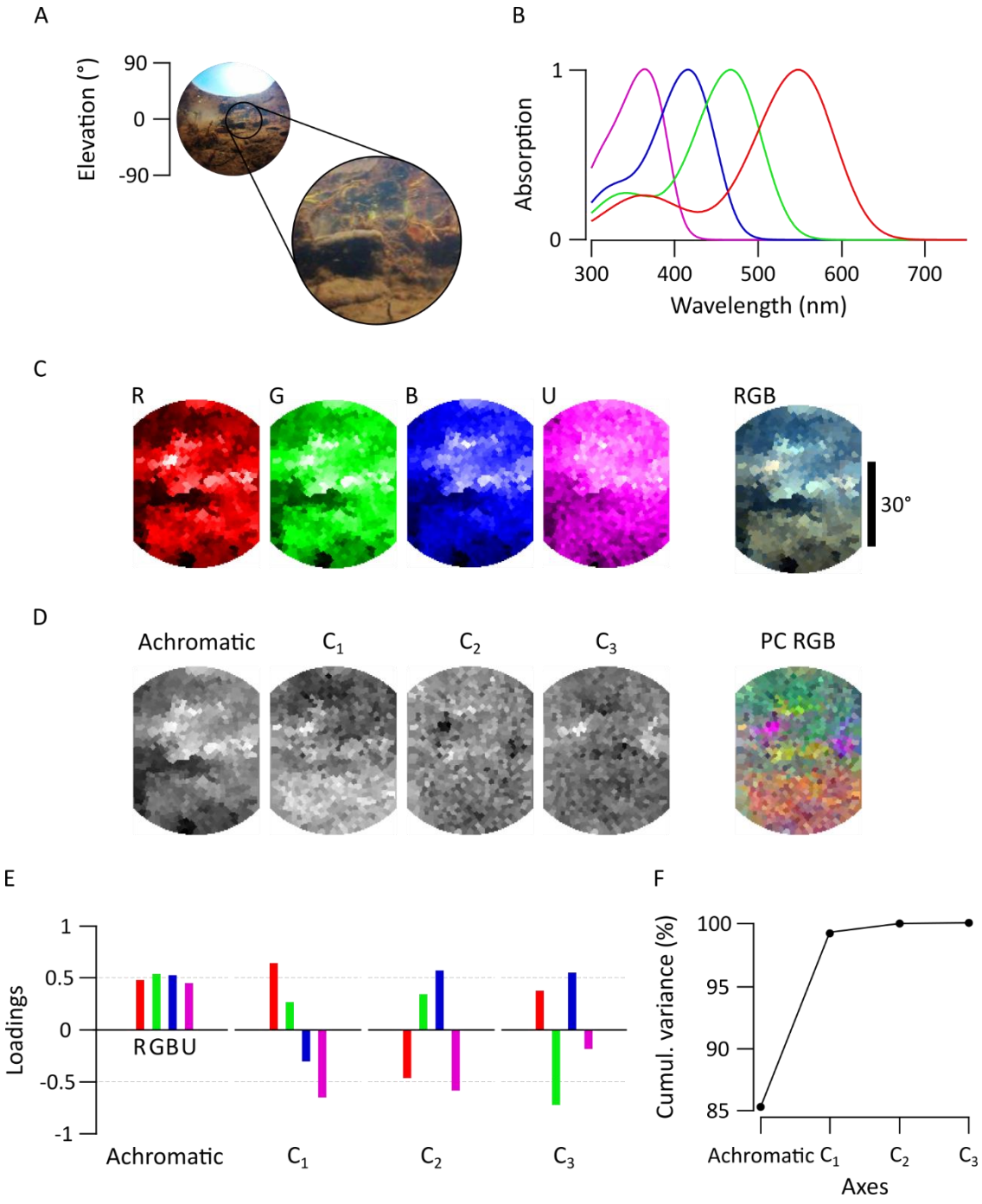


**Figure 2.8.** An underwater scene from India with zebrafish spectral sensitivity. **(A)** A 180° photo of the scanned underwater river scene from West Bengal, India, and the approximate 60° scanner covered window. **(B)** The zebrafish visual pigment complement. **(C)** The monochromatic opsin channels (RGBU) and the RGB reconstruction as in Figure 2.4. **(D)** The achromatic and chromatic axes reconstructed back to images to show where in the scene information based on each axis can be found. **(E)** Loadings from each opsin channel as explained in Figure 2.4E. **(F)** The cumulative variance explained (%) for each axis.

**2.5 Discussion**

We have designed and implemented an inexpensive and easy-to-build alternative to commercial hyperspectral scanners suited for field work above and under water. Without the spectrometer (~£1,500), the entire system can be built for ~£113-340, making it notably cheaper than commercial alternatives. In principle, any trigger-enabled spectrometer can be used for the design. Alternatively, spectrometers can also be home-built (Warren and CC-BY-SA 2017 Public Lab contributors; Rossel, 2017) to further reduce costs.

When studying natural imagery in relation to animal colour vision, it is important to consider how the spatial detail of the measured image relates to the spatial detail the animal's retina can resolve. The spatial resolution limit of our scanner with the oversampling 1,000-points scan (4.2°), though substantially below that of most commercial camera systems, is close to the behavioural resolution limit of key model-species like zebrafish larvae (~3°) (Haug *et al.*, 2010) or fruit flies (~1-4°) (Juusola *et al.*, 2017) but falls short of the spatial resolution achieved by most larger species such as mice or primates. Accordingly, natural imaging data obtained with our scanner spatially under samples the natural visual world of these larger animals. However, when studying animal colour vision this is not necessarily a major issue. First, spatial contrast in images is generally scale-invariant (Saremi and Sejnowski, 2016). Second, most animal visual systems inherently combine a low-spatial resolution chromatic representation of the visual world with a high-spatial resolution achromatic representation (Mullen, 1985; Giurfa *et al.*, 1996; Lind and Kelber, 2011). As such, our system can likely also give useful insights into the chromatic visual world of animals with much more highly resolved eyes.

The spatial resolution of our system could principally be further improved, for example by using a smaller pinhole in combination with higher-angular-precision motors. However, the amount of natural light for vision is limited, especially when imaging under water where light is quickly attenuated with increasing depth. As a result, higher spatial resolution in our system would require a substantially increased integration times for each pixel. This would result in very long scan-durations, which is unfavourable when scanning in quickly changing natural environments. Alternatively, the addition of a lens or parabolic mirrors would allow substantially increasing the total amount of light picked up by the system, thus bringing down integration time. Finally, the use of an elongated pinhole oriented perpendicular to the spectrometer slit may help set-up a more symmetrical field of view. These modifications would likely need to come in hand with substantial mechanical alterations, increased cost, and possibly new limitations pertaining to chromatic aberrations.

Spatial resolution aside, the spectral range and detail of our scanning approach far exceeds the spectral performance of interference filter-based approaches, as used in most previous hyperspectral imaging studies (Nagle and Osorio, 1993; Osorio, Ruderman and Cronin, 1998; Párraga *et al.*, 1998; Ruderman, Cronin and Chiao, 1998; Chiao, Cronin and Osorio, 2000). This difference may be crucial for some questions. For example, zebrafish have four opsin-genes for middle wavelength sensitive (MWS) cones ("green cones") that are used in different parts of the retina and are separated in spectral sensitivity by few nanometres (Chinen *et al.*, 2003; Takechi and Kawamura, 2005a). Most interference filter setups use relatively broad spectral sensitivity steps and would therefore miss small details in the natural scenes that could be picked up with slightly different spectral sensitivities of different opsins. By choosing individual "pixels" and the spectra they hold, it is possible to analyse fine details in complex scenes that animals can use for colour vision. This can be done already with very coarse spatial resolution to reveal structures that otherwise would remain undetected. In agreement with previous studies, we have shown how principal component analysis aids to separate achromatic and chromatic information in natural images (Ruderman, Cronin and Chiao, 1998; Chiao, Cronin and Osorio, 2000). Here, PCA across the chromatic channels highlights spatio-chromatic aspects in the scene that may be useful for vision. Perhaps not surprisingly, this reveals major, overall trends in landscapes (Figs. 2.4-2.6) with short wavelength dominated sky and long wavelength dominated ground. This is true also for the underwater habitats (Fig. 2.8), where light spectrum in the water column transforms from "blue-ish" short wavelength dominated to "red-ish" long wavelength dominated with increasing depth (Zimmermann *et al.*, 2018). The PCs can also highlight details in complex scenes that might otherwise stay hidden but that may be important for animals to see in their natural habitats.

Even though our spectrometer is sensitive deep into UV range (200-400 nm), the sensitivity of CCD spectrometers at these wavelengths is approximately 2.5 times less than at 650-700 nm due to the photometric calibration. For now, this has not been accounted in the measurements shown throughout this thesis and our analysis might underestimate the number of UV photons available in the nature. A spectrometer with higher sensitivity to UV light could produce slightly different results with stronger contrasts in colour channels.

With our examples from terrestrial and aquatic environments (Figs. 2.4-2.8) we demonstrate how our device and the resulting data can be used for studying the first steps of animal colour vision. With diverse and careful measurements, it is possible to reach better understanding of the spectral environments that animals live in. Here, by considering their photoreceptor tunings it is possible to get first ideas of what might be important for specific animals to see in their

natural habitats. However, to more fully understand how animals use and respond to the spectral information reaching their retinas, additional direct physiological recordings as well as behavioural testing are needed (Baden and Osorio, 2018).

### 2.6 Conclusion

We have shown how our simple, self-made scanner can produce hyperspectral images that can be used to study animal colour vision. We demonstrate this with examples from both terrestrial and aquatic environments and show how individual hyperspectral images can be used to make comparisons between different species and their possible view of the world. We have also started to populate an open database of hyperspectral images from various natural scenes (https://zenodo.org/communities/hyperspectral-natural-imaging). In the future, it will be interesting to survey a more varied set of habitats and, for example, to compare how closely related animal species living in different habitats have evolved with varying visual abilities. This could also include variations of the presented design, for example to scan larger fields of view, or a time-automation mode by which the same scene can be conveniently followed over the course of a day. We will be pleased to facilitate other's additions to the design through a centralised project repository (https://github.com/BadenLab/Hyperspectral-scanner) and hope that in this way more researchers will be able to contribute to building a more global picture of the natural light available for animal vision on earth.

### 2.7 Author contributions

The scanner was conceived and implemented by NEN and TB. Data was analysed by NEN using custom scripts written by TB and modified by NEN. The paper was written by NEN with help from TB.

### 2.8 Acknowledgements

We thank Kripan Sarkar and Fredrik Jutfeld for help with fieldwork, and Dan-Eric Nilsson, Daniel Osorio and Thomas Euler for general discussions. The authors would also like to acknowledge support from the FENS-Kavli Network of Excellence. Funding was provided by the European Research Council (ERC-StG "NeuroVisEco" 677687 to TB), The Medical Research Council (TB,

MC_PC_15071), The Biotechnology and Biological Sciences Research Council (TB, BB/R014817/1), the Leverhulme Trust (PLP-2017-005 to TB) and the Lister Foundation.

**2.9 Declaration of Interests**

The authors declare no competing interests.

# *Chapter 3 – Spectral variation in zebrafish's natural habitats*

In this chapter I present my results from a published paper: Zimmermann*, MJY, Nevala*, NE, Yoshimatsu*, T, Osorio, D, Nilsson, D-E, Berens, P and Baden T. 2018. Zebrafish Differentially Process Color across Visual Space to Match Natural Scenes. *Current Biology*, 28, 2018-2032.
* = first co-author. All individual measurements taken with the 60° scanner are presented in the Appendix 2. In addition, here I present extra findings from the field that are currently unpublished.

### 3.1 Introduction

Zebrafish (*Danio rerio*) is a common model in visual neuroscience but systematic studies on their natural visual environments at the Indian subcontinent have been lacking. They live in small, shallow ponds and slowly moving streams with varying amount of vegetation, and are omnivorous accepting anything from zooplankton to small insects and plant detritus as their prey (Arunachalam *et al.*, 2013). As zebrafish themselves are also a prey for other larger fish species and birds (Engeszer *et al.*, 2007) they can be found in protective rice paddies and side pockets of larger rivers as well.

Breeding happens from April till August in shallow, protective side waters. Starting from 4-5 *dpf* zebrafish larvae are relying on their vision to catch prey (Raymond, Barthel and Curran, 1995; Easter Jr. and Nicola, 1996; Schmitt and Dowling, 1999; McElligott and O'Malley, 2005). By this age, they have large, fully developed eyes with a complete tetrachromatic colour vision sensitive to UV, blue, green and red light. As explained in Chapter 1, there are several options for the opsin expression for green and red cones and the expression rates change during the development. In addition, the chromophore bound to the opsin can be either 11-*cis*-retinal (A1 vitamin) or 11-*cis*-3,4-didehydroretinal (A2 vitamin), although the use of A2 chromophore in natural conditions has not been proved. To simplify the spectral sensitivity of the larvae, here after the $\lambda_{max}$ values for each cone type are assumed as 365 nm for UV (U), 416 nm for blue (B), 467 nm for green (G) and 548 nm for red (R) cones (Chinen *et al.*, 2003; Allison *et al.*, 2004; Takechi and Kawamura, 2005a). Other possible pigments in the cornea, vitreous and the lens can also have an effect to the light spectrum reaching the photopigments in the photoreceptors, especially designed to filter out the shorter and therefore much more harmful wavelengths (Douglas and McGuigan, 1989; Siebeck and Marshall, 2001). Measurements for the existence of these pigments in the zebrafish larval eyes are lacking, but strong expression of UV cones across the whole retina suggests that they either do not have these pigments or the possible effect is negligible.

Considering the increasing amount of research focusing on the retinal connections processing the visual information in zebrafish eyes, it is surprising how the spectral composition of their natural habitats has not been properly studied. With natural imaging it is possible to get detailed spatial and spectral information from an animal's natural environment. Combining these results to the colour vision abilities of the animal it is possible to understand what chromatic information is available and how well they have adapted to their environment. This is especially useful for popular model animals such as zebrafish, as it enables designing and implementing species specific, spectrally detailed visual stimulators that mimic closely natural spectral variations.

Here, I examined the spectral composition of zebrafish's natural environments in India with commercially available, high spatial resolution action camera and two custom built hyperspectral scanners. One of the scanners, introduced in Chapter 2, produces a 60° high spectral resolution image of the scanned scene. My second scanner design takes 46 equally spaced hyperspectral measurements on a 180° vertical line. With both scanners I found that the light spectrum becomes increasingly monochromatic and biased towards longer wavelengths with increasing depth. Principal component analysis on the 60° scanner data reveals chromatically rich zones around the horizon and lower visual field. In addition, by examining the measured scans as monochromatic representations with individual zebrafish cone types, different cones provide different type of information on their own. These findings match rather perfectly with the varying cone densities and anisotropic organization of bipolar cells in the zebrafish larvae retina.

## 3.2 Methods

### *3.2.1 Field sites*

Measurements with the 60° image forming scanner (here after referred as the "60° scanner") were taken in May in 2017 in North-East India (Fig. 3.1A, circles). The global positioning coordinates for these sites are: site 1 (lat. 26.531390, long. 88.669265), site 2 (lat. 26.528117, long. 88.641474), site 3 (lat. 26.841041, long. 88.828882), site 4 (lat. 26.792305, long. 88.588003), site 5 (lat. 26.903202, long. 88.554333) and site 6 (lat. 26.533690, long. 88.648729). Altogether $n$ = 31 measurements were taken between 11am and 5pm. Sky was either cloudy or clear, but weather conditions remained constant through each measurement. As explained in Chapter 2, the acquisition time for one scan depends on the time set for mirror movements (sampling time) and the time set for the spectrometer to take a measurement from one "pixel"

(integration time). The sampling times (200-500 ms) and integration times (80-200 ms) were adjusted individually for each site to get consistent signal-to-noise ratio independent of the overall light intensity. Overall each scan lasted approximately between 4 and 8 minutes. Immediately after each scan an additional still image was taken at the scanner position with an action camera (Campark ACT80 3K 360°) with a 180° fisheye lens.

Measurements taken with the 180° vertical line scanner (here after referred as the "180° scanner") were taken in October 2019 in North-East India (Fig. 3.1A, triangle). The global positioning coordinates for this site are: lat. 26.31241, long. 91.475. Altogether $n$ = 6 scans were taken between 8 and 11 AM at one site under a clear sky. Measurement time lasted approximately 30 seconds depending on the integration (200 ms) and sampling (300 ms) times. As with the 60° scanner, a still image with the Campark action camera was taken towards the direction of the vertical scan after each measurement.

As the main criteria for a measurement spot, zebrafish of all ages were found at all sites. The measured habitats included natural streams and ponds as well as a human made fish farm pond (Figs. 3.1B-D). The vegetation above and under water in these habitats varied from dense to no vegetation at all, had different substrate types and variable water currents (Figs. 3.1E-G). Water depth remained below 50 cm for each measurement and diving weights were used to control the buoyancy and stabilize both scanners under water. After placing the equipment in the water, I waited for 5 minutes for the debris to settle before starting a measurement to avoid possible disturbances in the view.

### *3.2.2 Hyperspectral imaging*

In the 60° image forming scanner two spectrally broad UV reflecting mirrors are mounted on top of micro-servo motors, which are controlled by an Arduino Uno microcontroller. In the complete system, light travels first through a quartz-window to reach the mirrors inside a waterproofed casing and is then reflected through a pinhole to reach the active sensor array on the spectrometer (Thorlabs CCS200/M, 200-1,000 nm). During one scan, the mirrors are moved iteratively through space in order of a previously defined scan path under a serial control from a computer. At each new mirror position the spectrometer is triggered to take a measurement, which is fed to a computer running the OSA Thorlabs software. Here, each scan was taken with a 1,000 points spiral scan path. For further details, see Chapter 2 (Nevala and Baden, 2019).

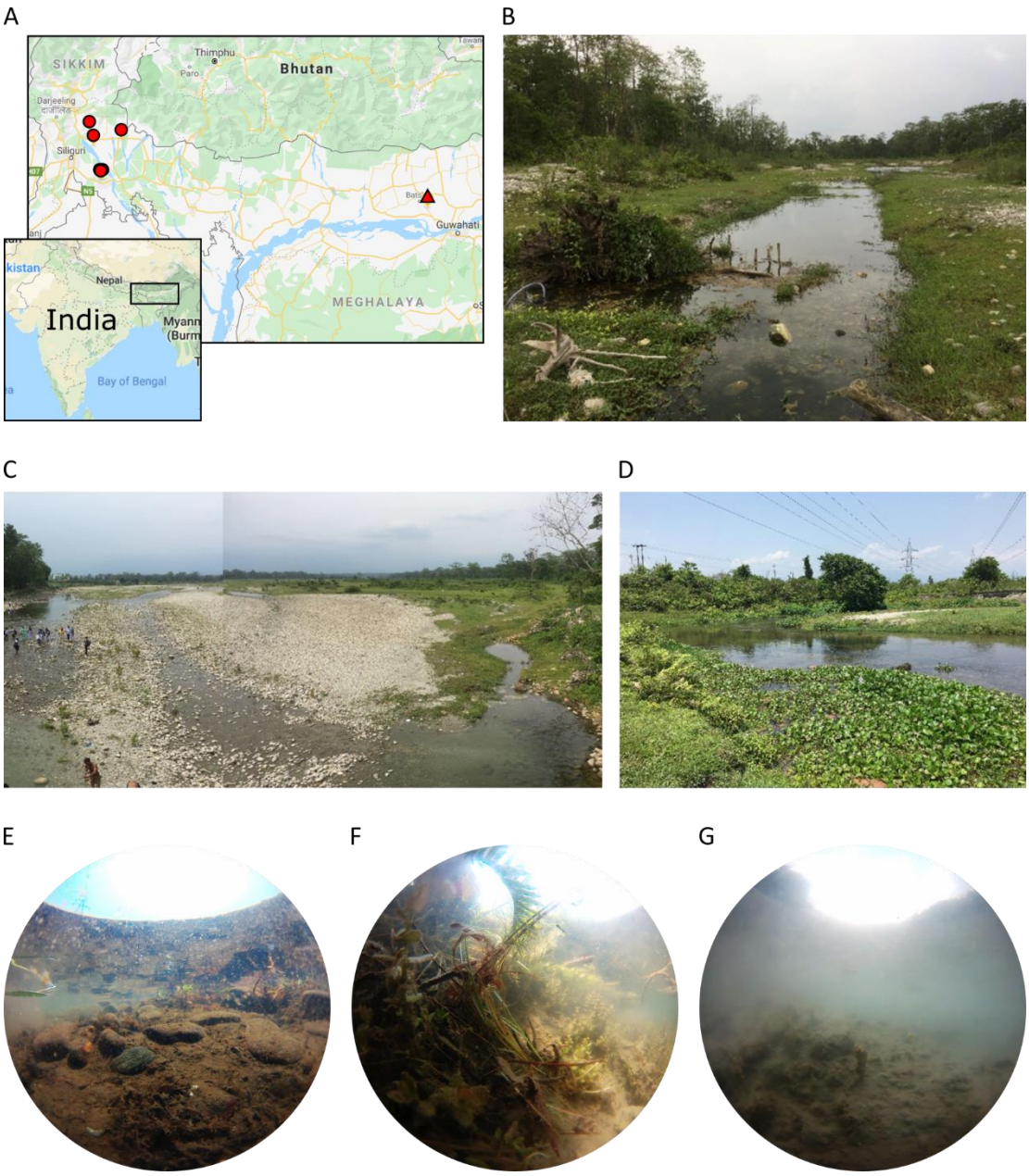


**Figure 3.1. (A)** Locations of the field sites visited in 2017 (circles) and 2019 (triangles). **(B-D)** Example images of the field sites visited in May 2017. **(E-G)** Examples of measured underwater scenes.

Like the 60° scanner, the 180° vertical line hyperspectral scanner is built around Thorlabs CCS200/M spectrometer. In this setup, light first enters a 3D printed periscope through a broadband window (Thorlabs WG41050 - Ø1" UVFS Broadband Precision Window, Uncoated, t = 5 mm). Light rays are focused, collimated and reflected with two lenses (Thorlabs LA1131 - N-BK7 Plano-Convex Lens, Ø1", f = 50.0 mm, Uncoated and Thorlabs LA1417 - N-BK7 Plano-Convex Lens, Ø2", f = 150.0 mm, Uncoated) and a mirror (Thorlabs PFSQ10-03-F01 - 1" x 1" UV-Enhanced Aluminum Mirror) before reaching the spectrometer inside a waterproofed Peli 1150 Protector Case (Figs. 3.2A-B). An Arduino Uno microcontroller moves a 3D printed cogwheel mounted on

a servo motor (Lewansoul Hiwonder LD-20MG Full Metal Gear Standard Digital Servo) in individual, 4° increments to move another cogwheel attached to the base of the periscope in order to move the measurement point is space. After each motor movement, the spectrometer is triggered to take a single reading via the Arduino (Figs. 3.2C-D). All in all, one scan is constructed from 46 measurement points when moving from up to down, and another set of 46 measurements from the same points when the periscope returns to the starting position via the same route. All the 3D printed parts were designed with OpenSCAD (www.openscad.org) and printed with an Ultimated 2 3D printer running Cura 2.7.0 (Ultimaker). All hyperspectral imaging data was analysed with IGOR Pro 7 (Wavemetrics) and Fiji (NIH) with self-made scripts.

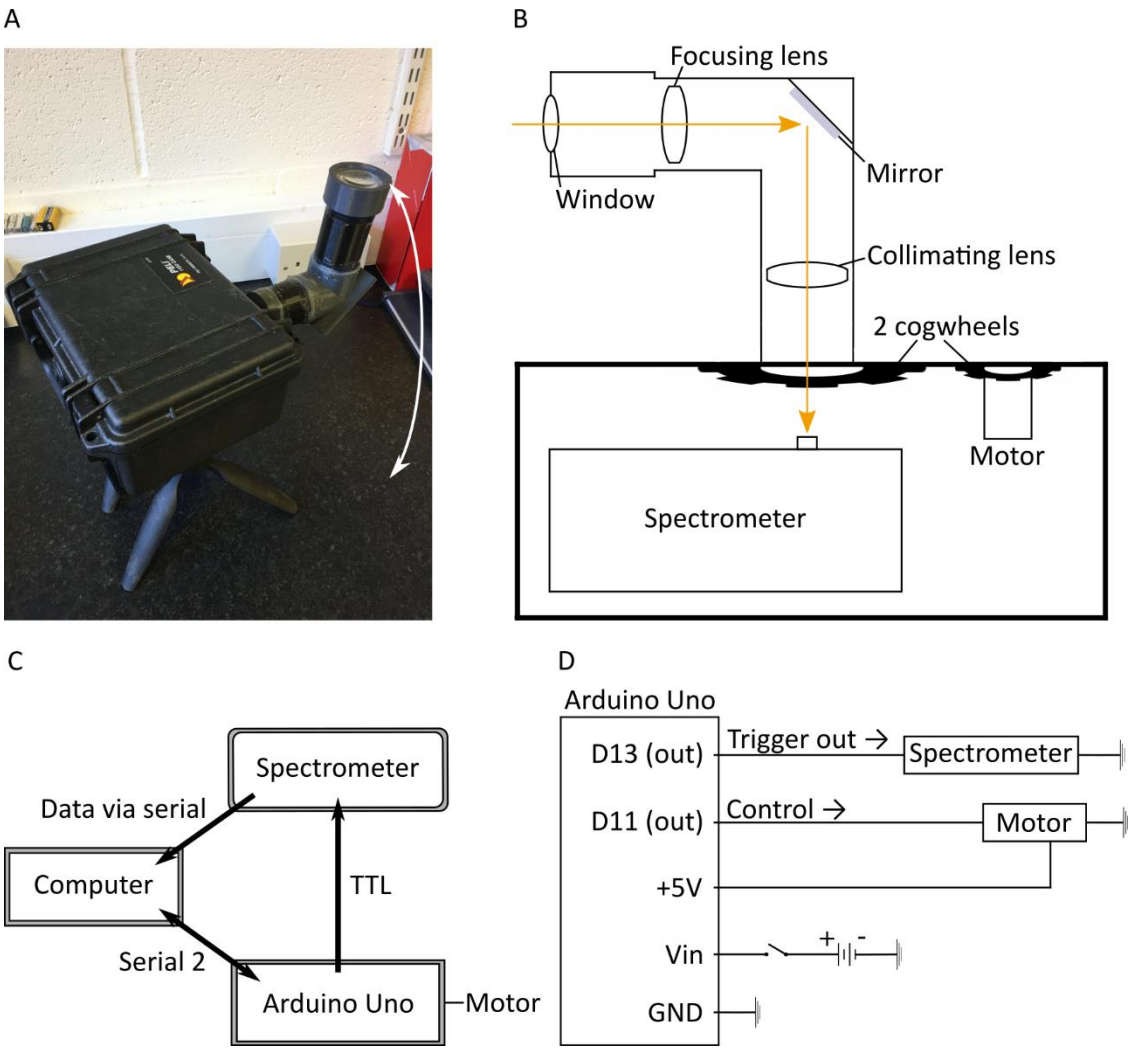


**Figure 3.2.** A 180° vertical line scanner. **(A)** A photograph with the periscope in the starting position pointing upwards. The white arrow shows the up- and downward directions of the scan. **(B)** A schematic illustration of the main components in the system, with yellow arrow showing the light path to the spectrometer. The cogwheel attached to the motor will turn the other cogwheel attached to the periscope. Operational logic **(C)** and circuit diagram **(D)** in line with the 60° scanner explained in Chapter 2, except here with only one motor.

## 3.3 Results

### *3.3.1 Action camera images provide the first glimpse to the zebrafish's underwater world*

In zebrafish larvae each eye covers a 163° field of view when at rest (Bianco, Kampff and Engert, 2011). The 180° action camera images demonstrate visual features dominating the visual field in every habitat (Fig. 3.3A) that are simultaneously visible for the larvae's eyes. The upper part of the water body is dominated by a clear opening called Snell's window, where the almost full 180° representation of the world above the water is projected through a 97° cone of light to the viewer below. Outside the Snell's window the underside of the water surface reflects the ground and other physical features such as rocks and plants below.

All 31 action camera images were averaged together (Fig. 3.3F) and the z-normalised luminance values for blue, green and red channels across the scene were taken (Fig. 3.3G). To better show the difference between the three channels, mean between all channels was subtracted (Fig. 3.3H). Unsurprisingly, the overall luminance for all channels decreases and the light available becomes long wavelength (red) dominated with increasing depth. The upper part of the water body with Snell's window is short wavelength (blue) dominated with green dominated horizon below.

As explained in Chapter 2, principal component analysis (PCA) offers a useful way to handle complex datasets to extract variables that explain most of the data in decreasing order of importance. In natural imaging PCA can be used to separate achromatic and chromatic information. Here, I used PCA across the 31 action camera images individually to find the chromatic variance in the scenes (Figs. 3.3B-D). In line with previous research (Chiao, Cronin and Osorio, 2000; Lewis and Li, 2006), the first principal component (PC1) is always the achromatic channel with equal variation from all three RGB channels describing the variation in luminance across the scene. From the total variance, PC1 always covers >90% of the data leaving ~10% for the chromatic variation in PC2 and PC3.

As the PC2 and PC3 are the chromatic channels (hereafter $C_1$ and $C_2$, respectively), they explain the data by comparing individual channels. $C_1$ covers most of the chromatic variation across the scene by comparing blue and red channels to each other. The remaining data is covered by $C_2$, where the information from blue and green channels is compared. Figures 3.3C-D show how different details in the scene are highlighted by $C_1$ and $C_2$, and how $C_2$ gets increasingly noisy with less spatial structures appearing. Next, each of these PC images were further divided to 5° wide horizontal stripes and the amount of variation each principal component covered in each stripe was plotted against elevation (Fig. 3.3E). Most of the chromatic information from $C_1$ and

$C_2$ is located around and below the horizon, while the area covering the Snell's window is strongly achromatic.

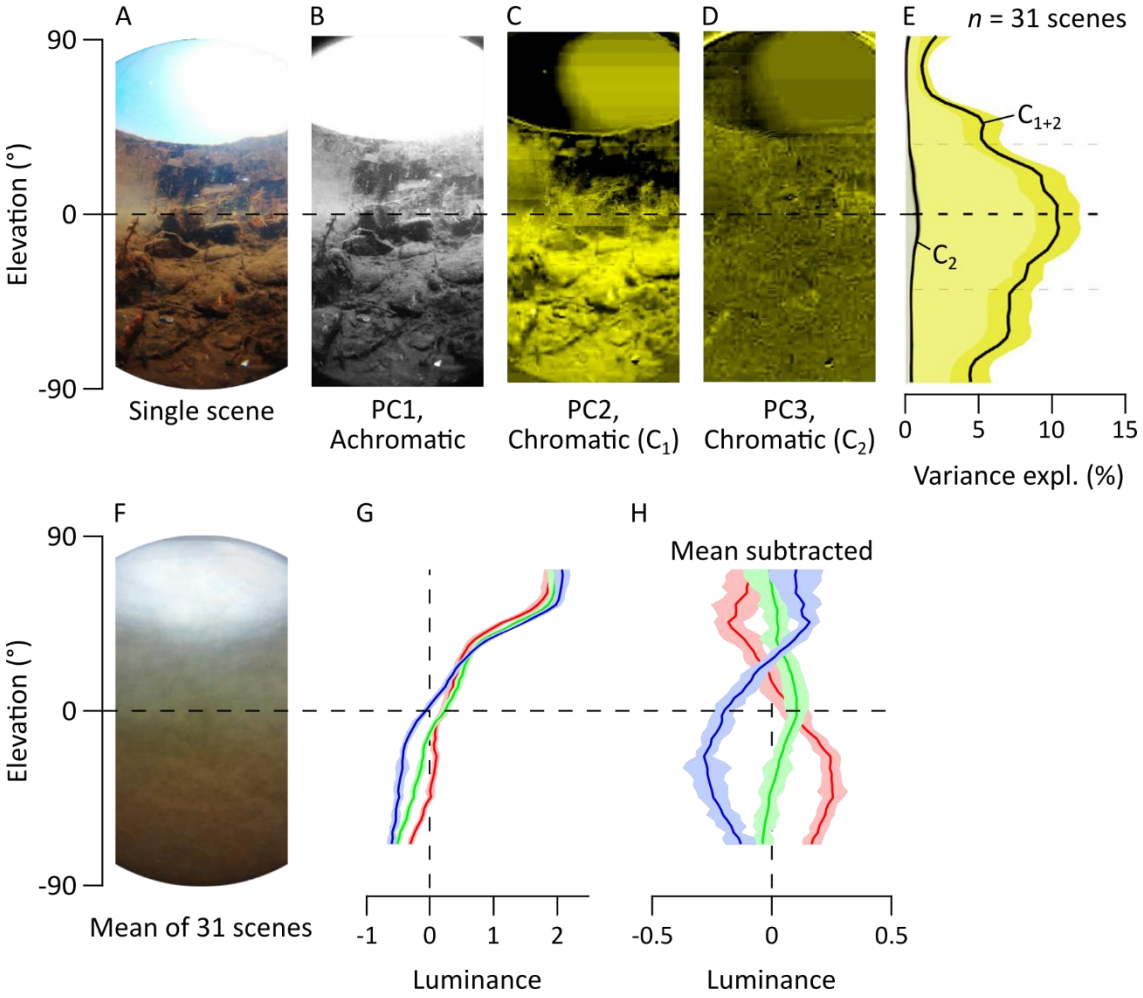


**Figure 3.3.** Principal component analysis across an action camera image and luminance variation in red, green and blue channels against elevation. **A)** An action camera picture of a single scene. **(B)** PC1 is an achromatic channel describing variation is overall luminance. Here, the "achromatic" refers to lack of chromatic contrast in the data. **(C)** PC2 ($C_1$) is the most important chromatic channel and covers most of the colour variance done between long and short wavelengths. **(D)** PC3 ($C_2$), the last chromatic channel, shows only small details with more complex colour comparisons. **(E)** Cumulative variance from $C_1$ and $C_2$ against elevation from 31 scenes. Most chromatic variance is at and below horizon, while Snell's window is strongly achromatic. **(F)** The mean of 31 still images. Luminance **(G)** and luminance with mean subtracted **(H)** for RGB channels from the averaged 31 scenes. Luminance decreases with increasing depth and the dominant channel changes from blue in the Snell's window to red below the horizon. Between horizon and blue there is a green biased area. Errors s.e.m.

While the results from analysing the action camera images provide a good starting point for characterising the spectral composition of the underwater world, it is not feasible to study the natural light environment for zebrafish. Firstly, the action cameras are designed for human trichromatic vision and therefore filtered for human spectral sensitivity. Obviously, this is significantly different from zebrafish's spectral tuning. Secondly, the UV wavelengths are filtered out leaving an important part of the zebrafish's visual world completely ignored. Therefore, hyperspectral measurements with broad sensitive spectrometer were used to get full representation of the spectral content from these scenes.

### *3.3.2 Chromatically rich horizon lies between short and long wavelength dominated zones*

The 60° image forming hyperspectral scanner moves iteratively through the pre-defined 1,000 points spiral scan path and takes a full spectrum (200-1,000 nm) measurement at each "pixel" (for details see Chapter 2) (Nevala and Baden, 2019). Altogether 31 scans were taken, and as each scan has 1,000 measurement points the total amount of individual measurement points adds up to 31,000 individual spectra. To yield a general description of the light spectrum available in zebrafish's natural habitats and how it is seen by zebrafish cones, I averaged all the 31,000 spectra together and multiplied the result with the zebrafish's cone absorption curves (Fig. 3.4). The light spectrum under these fresh waters is strongly red shifted compared to the light spectrum measured from the sky with most of the short wavelengths (< 400 nm) absorbed and scattered (Fig. 3.4A). However, the peak of the underwater spectrum aligns closely with the peak sensitivity ($\lambda_{max}$) of the red cones at 548 nm (Fig. 3.4B). As the red cones get most of the power input in these scenes, it is sensible to think that these long wavelength sensitive photoreceptors are responsible to detect features that require the highest signal-to-noise ratio, such as movement detection. Compared to the red cones, green cones receive approximately 45% and blue cones 16% of the photons available. Interestingly, the UV cones only receive ~7% of the photons compared to the red cones. Even though the photons available for these short wavelengths is minimal, the larval zebrafish still invest considerable amount of energy to maintain functional UV cones throughout the retina. From this it can be concluded that the UV channel provides important benefits for the fish, such prey detection (Novales Flamarique, 2013, 2016), and lacking this ability would crucially reduce the chances of survival. However, this is only a generalized light spectrum over the entire light profile and therefore does not include the spatial details of how different features in the scene are detected with different cones.

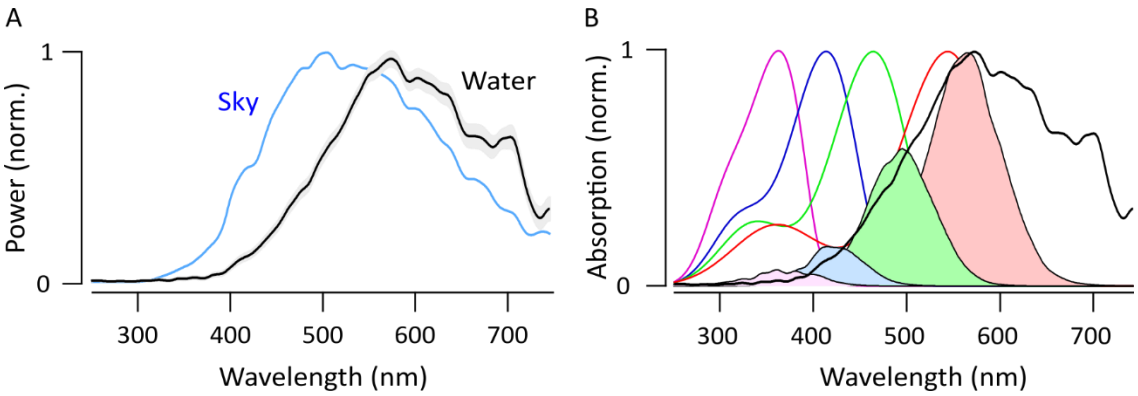


**Figure 3.4.** The average light spectra from sky and underwater. **(A)** Shorter wavelengths are absorbed and scattered under water, red shifting the average light spectrum when compared to the measurements taken on land from a clear sky. **(B)** The average light spectrum (black line) from 31,000 individual measurements shown in (A) has the highest peak slightly shifted towards longer wavelengths from the red cones. Shaded pink, blue, green and red areas demonstrate the relative photon catch rates when the average light spectrum is multiplied with UV, blue, green and red visual pigment templates (pink, blue, green and red solid curves, respectively).

All the spectra from 1,000 pixels from each scan were first multiplied with the zebrafish's cone absorption spectra to create monochromatic images or "opsin activation maps" for each cone type (Fig. 3.5A). These reconstructions demonstrate how the measured scene would look like when observed only by one cone type at a time. The clear differences can be seen between long wavelength (green and red) and short wavelength (blue and UV) cones. While R and G cones clearly pick up most of spatial structures such as the rocks and plants in the middle of the scene, the B and U cones become increasingly noisy mostly detecting the decreasing illumination with increasing depth. Therefore, individual cones can provide different type of information for the animal. For example, shorter wavelengths are much more suitable to detect passing dark shadows from possible predators, whereas this information would easily get lost in already crowded long wavelength channels (Cronin and Bok, 2016).

Next, as with the action camera images, I calculated the luminance values for each channel (R, G, B, and U) across the measured scenes against the elevation (Fig. 3.5B). Even though the Snell's window is excluded from the 60° scanner's view, the short wavelength channels are still the most dominant ones in the upper part of the scene. This time the, right before the horizon, there green channel is overridden by the red channel that has the highest luminance all the way to the bottom. The UV channel does provide an interesting profile however, as it has a drop in luminance at the horizon but increases again towards the bottom. This could be explained by small, individual UV bright surfaces on plants or rocks at the lower part of the scene.

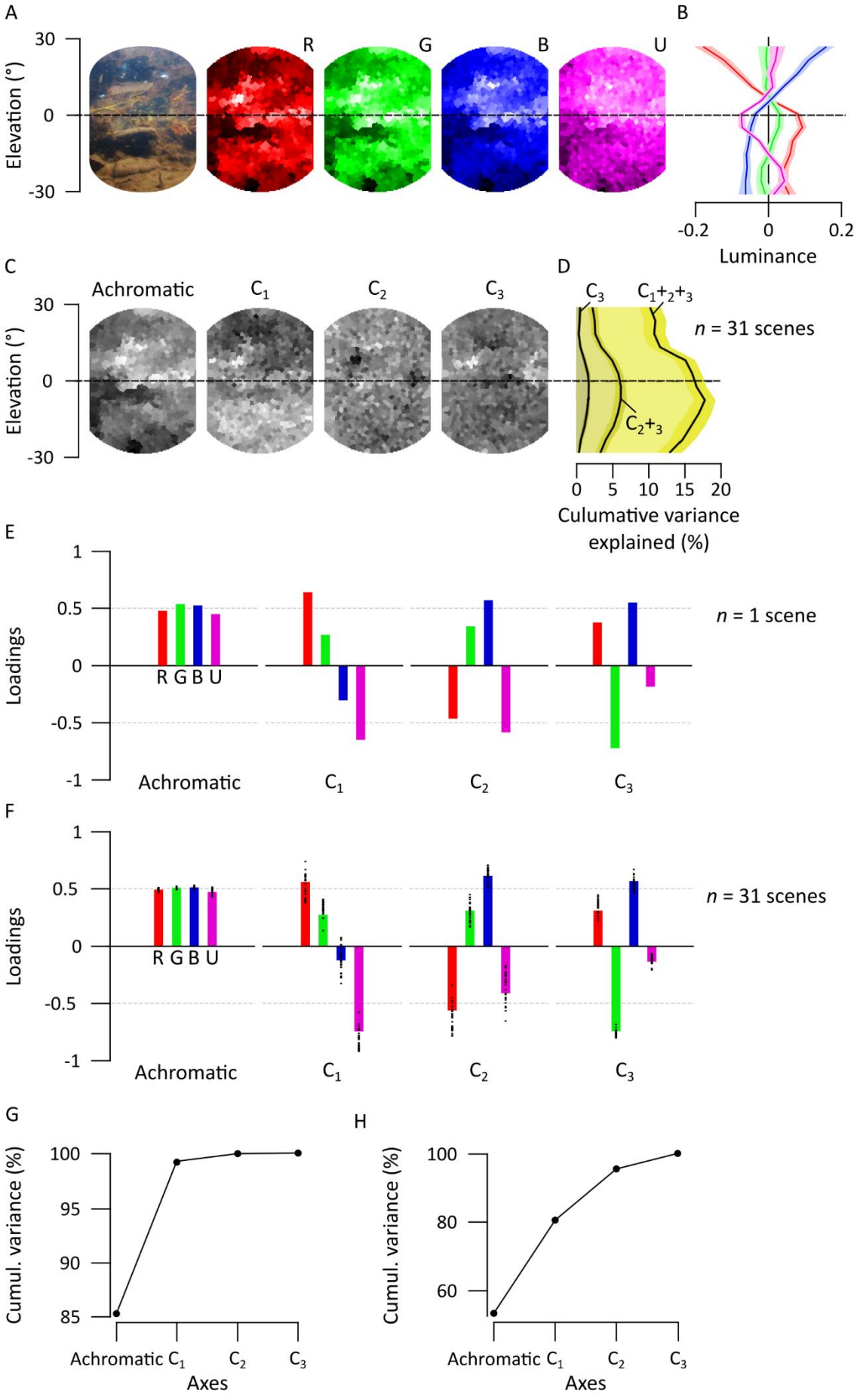
A
B
C
D
E
F
G
H
Elevation (°)
30
0
-30
R
G
B
U
-0.2
0
0.2
Luminance
Achromatic
C1
C2
C3
C1+2+3
C2+3
n = 31 scenes
0 5 10 15 20
Culumative variance explained (%)
Loadings
1
0.5
0
-0.5
-1
R G B U
n = 1 scene
n = 31 scenes
Cumul. variance (%)
100
95
90
85
80
60
Achromatic C1 C2 C3
Axes

**Figure. 3.5 (previous page).** An example measurement taken with the 60° scanner. **(A)** An action camera picture cropped to represent approximately the scanned scene and monochromatic cone activation maps when the original spectra from each pixel is multiplied with each cone absorption spectra. Different cone types can provide different information of the observed scene: red (R) and green (G) cones pick up most of the spatial information whereas blue (B) and UV (U) cones are more noisy describing illumination differences between upper and lower parts of the scene. **(B)** Luminance with mean subtracted from RGBU channels from the scanned scene. Shorter wavelengths dominate in the upper part of the scene while red channel becomes dominant at and below horizon. **(C)** Reconstructions of the principal component analysis to show where in the scanned scene chromatic details are. For further explanation see Figure 2.4 in Chapter 2. **(D)** The cumulative variance from chromatic channels after principal component analysis plotted against the elevation from all 31 scanned scenes averaged together. **(E)** Loadings explaining the input from each opsin activation map to the corresponding principal component. For further explanation see Figure 2.4 in Chapter 2. **(F)** Average loadings from all 31 measured scenes. Distribution of individual measurements shown in black squares. **(G)** The cumulative variance explained (%) for each axis for the example scene in A-E. **(H)** The cumulative variance explained (%) for each axis taken from random noise control.

As the opsin activation maps alone cannot provide chromatic information from the scene, I performed principal component analysis across these four channels. Again, the PC1 provides the achromatic variation in luminance with similar input from each cone channel (loadings, Fig. 3.5E) and always covers >90% of the data in each scan. The remaining PC2, PC3 and PC4 are the chromatic channels ($C_1$-$C_3$ hereafter) in decreasing order of importance comparing R+G vs. B+U in $C_1$, G+B vs. R+U in $C_2$ and R+B vs. G+U in $C_3$. These results are uniform across all the 31 measured scenes as shown in Figure 3.5F. As explained in Chapter 2, most of the variance in data is always covered by the achromatic axis with approximately 15% left for the chromatic axes (Fig. 3.5G). As a control, I created random, white noise data and performed PCA across the noise to see if the variance for each axis changes. Indeed, the variance explained is less highlighted by the first PC and the remaining data is more equally distributed with the remaining components (Fig. 3.5H). As the short wavelengths are quickly absorbed and scattered in the upper part of the water body leaving the deeper parts heavily long wavelength biased, the $C_2$ channel shows how most of the comparisons happen between above and below the horizon (Fig. 3.5C). The remaining chromatic channels, C2 and C3, together always only cover <1 % of the whole data leaving the PC reconstructions appearing noisier. However, individual details are still picked up. With the current hyperspectral scanners, it is not possible to reliably interpret what these small details count for and what they mean to the fish, but as energy is invested to detect them it is safe to say that they hardly are completely meaningless. Figure 3.5C shows an individual example of the principal component analysis results for one scene, but the opsin activation maps, PC RGB reconstructions and images from all 31 scenes can be found in the Appendix 2.

Like with the action camera images, the PC reconstruction images were again cut in 5° stripes and cumulative variation of each stripe was plotted against elevation (Fig. 3.5D). This revealed a similar build-up of the chromatic information around and below the horizon as in Figure 3.3E. The difference at the upper part of the scene with these colour rich areas was less striking than in the action camera images, as the completely achromatic Snell's window was not included in the scans.

### *3.3.3 The average light spectra across the 180° elevation are mostly driving green cone activations*

The results from the 60° scanner show how areas up and below the horizon create spectrally different zones with short wavelength dominated upper part and long wavelength dominated lower part of the water body. However, a 60° image is only a limited snapshot of the surroundings, especially for a zebrafish larva that has a 163° field of view for each eye. To overcome this limitation, I designed and built a 180° hyperspectral scanner to take light measurements from a vertical line in underwater habitats. With this method I was able to complement my existing dataset from the 60° scanner to gain a better understanding of the spectral variation in the zebrafish larva's whole vertical field of view.

Each scan consisted of 46 measurement points on vertical line in 4° increments with first measurement taken directly upwards and last straight down. Each point was measured twice as the scanner repeated the measurements when returning to the original position, resulting in total of 92 measured points. All 6 scans were averaged together and further sliced to nine 20° wide horizontal zones (A-I, Fig. 3.6A) where an average spectrum from each zone was taken (Fig. 3.6B). Figures 3.6B and 3.6E show how light intensity decreases over 10-fold when moving from the surface to the bottom. Interestingly, the light intensity peak is not at the zone A but at the zone B. This might result from the sun shining slightly from the side and not directly above when performing the scans (Fig. 3.6A).

In line with the previously discussed data, Figures. 3.6B-C and 3.6G demonstrate how the light spectrum becomes increasingly monochromatic when both extremes of the wavelengths are absorbed and scattered. The peak of average light spectrum shifts from 524 nm in zone A looking upwards in the water column to 586 nm in zone I looking downwards (Fig. 3.6D). In line with the results from the 60° scanner, the average spectrum from zone I is shifted slightly towards longer wavelengths when compared to the red cone peak absorbance. By multiplying the average spectrum from each zone with the spectral sensitivities of the larval zebrafish cones, I then

created a relative opsin activation profiles against the elevation (Fig. 3.6F). This revealed how green cones are dominating at all other water depths except at the bottom where the red cones absorb most of the photons available. UV cones lose almost all the photons when directed to the bottom whereas, rather surprisingly, blue cones stay active throughout the entire water body.

**Figure 3.6 (next page).** 180° vertical line scanner measurements. **(A)** An action camera image of a single scanned scene with a white dashed line indicating approximately the direction of the scanned, vertical line. Zones A-I demonstrate the 9 areas used to describe the different elevations in the following graphs. **(B)** Average spectra from each 9 zones (A-I from dark blue to light grey, respectively) demonstrate how light intensity decreases with increasing depth. Both extremes of the wavelength variation are absorbed and scattered turning the spectrum more monochromatic. **(C)** Average spectra from (B) normalised to show how light becomes more monochromatic while shifting towards longer wavelengths with increasing depth. **(D)** Normalized average spectra for A and I zones (blue and grey lines, respectively) plotted against UV, blue, green and red cone absorption curves (shaded areas). **(E)** Light intensity profile against elevation. Highest intensity in the zone B is likely to result from sun shining slightly from the side rather than directly above during the scan. Error shadings in SD. **(F)** Relative opsin activations with SD error shadings for red, green, blue and UV cones against elevation (red, green, blue and pink lines, respectively). Green cones dominate in all other elevations except at the bottom (zones H and I). **(G)** A heatmap from one example measurement illustrating light intensities at different wavelengths across the elevation in one example measurement. In (B-F) data is from the average of $n$ = 6 scans.

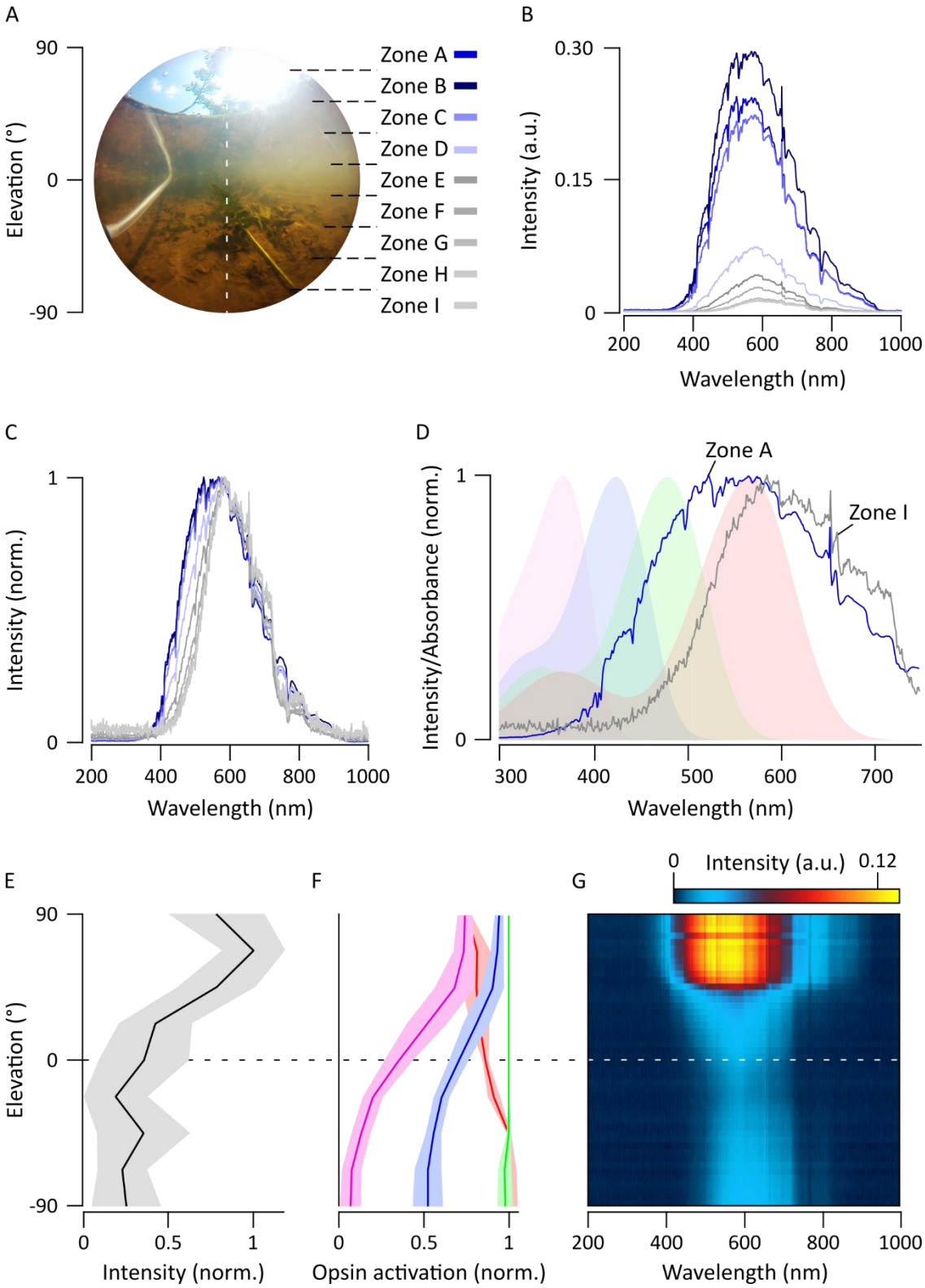
A
90
0
-90
Elevation (°)
Zone A
Zone B
Zone C
Zone D
Zone E
Zone F
Zone G
Zone H
Zone I
B
0.30
0.15
0
Intensity (a.u.)
200
400
600
800
1000
Wavelength (nm)
C
1
0
Intensity (norm.)
200
400
600
800
1000
Wavelength (nm)
D
1
0
Intensity/Absorbance (norm.)
Zone A
Zone I
300
400
500
600
700
Wavelength (nm)
E
90
0
-90
Elevation (°)
0
0.5
1
Intensity (norm.)
F
0
0.5
1
Opsin activation (norm.)
G
0
Intensity (a.u.)
0.12
200
400
600
800
1000
Wavelength (nm)

**3.4 Discussion**

In this chapter I have showed my results from the light spectrum measurements in zebrafish's natural habitats on the Indian subcontinent with three different methods: action camera images, 60° image forming hyperspectral scanner and a 180° vertical line scanner. Although none of these methods alone are sufficient to perfectly describe the spectral properties of these under water habitats, they complement each other and provide a representative, first description on what visual information is available for the zebrafish to see.

The general light spectrum produced by averaging 31,000 individual measurement points from the 60° scanner dataset showed a strong red shift compared to the light spectrum measured from the sky, aligning closely with the peak spectral sensitivity ($\lambda_{max}$) of the red cones at 548 nm (Fig. 3.4B). The 180° scanner data covering three times larger vertical spatial variation can be further divided into separate zones to demonstrate how elevation affects the light spectrum (Fig. 3.6). This revealed how light at the zone closest to the water surface has a broad spectrum with peak at 524 nm. As expected, the maximal transmission at the bottom zone is red shifted for approximately 60 nm. At the zones A-G green cones dominate with the highest opsin activation (Fig. 3.6F). Since the 60° scanner spectrum fits best with the average spectra taken from the two lowest zones in the 180° scanner data, it is possible that the 60° measurements have been pointing more towards the bottom. In addition, the sample size is significantly different as the 60° scanner dataset was gathered from 31 different scenes covering several different habitat types and the 180° consists of only 6 scans from one habitat. The data from 60° scanner could not be easily divided into different habitat types because the substrate, vegetation and water flow varied at every spot, so the possible effect of these in the spectra could not be studied from my existing scans. Furthermore, time of the day and even the season could affect the difference in general light spectrum from 60° and 180° scanners (Mcfarland, Ogden and Lythgoes, 1979). Additional measurements are needed at controlled times of the day and during different seasons to understand how this might affect the spectral information available at different times.

Both hyperspectral scanners demonstrate how light becomes increasingly monochromatic when moving from water surface towards the bottom (Figs. 3.5B and 3.6C). In addition, light closer to the surface is short wavelength dominated while the spectra below the horizon are dominated with longer wavelengths. This most important chromatic variation is also explained by the principal component analysis, where most of the chromatic comparisons is always done with red and green vs. blue and UV (Figs. 3.5C, E). Data from action camera images and 60°

hyperspectral scanner demonstrates how most of the chromatic information available for the zebrafish larvae in their natural habitats is situated around the horizon. According to the efficient coding hypothesis (Attneave, 1954; Simoncelli and Olshausen, 2001), this should be reflected also in the functional properties of the retina. Unlike the adult zebrafish (Engstrom, 1960), zebrafish larvae do not have evenly distributed cones in a mosaic pattern. Instead, different cone types have varying densities with RGB cones showing their highest peak at the horizon well aligned with the natural statistics (Zimmermann *et al.*, 2018). The UV cones have their highest density in the ventro-temporal part of the retina ("strike zone"), looking towards the up-front part of the visual field. This aligns rather perfectly with their spectral surroundings as well, as most of the shortest wavelengths are in the upper part of the visual field. Since these short wavelengths (< 400 nm) are well detected with the high density of the UV cones in the strike zone, this further supports the previous speculations that the UV channel could be used to detect UV-bright zooplankton such as paramecia (Cronin and Bok, 2016; Novales Flamarique, 2016; Yoshimatsu *et al.*, 2020).

Although this dataset provides an important first glimpse to the zebrafish's natural spectral environments, further improvements are still needed. As the spatial resolution of the 60° scanner is limited and cannot be improved easily (see Discussion in Chapter 2), other methods should be used to study how adult zebrafish see their surroundings and how this differs with the larvae. One option to achieve this goal is to use the same approach as Tedore and Nilsson (2019) presented in their study for avian vision. Since the spectral sensitivity of a zebrafish is well known, spectrally specific filters can be designed to use a multispectral wheel camera to take high spatial resolution images from underwater world as it would be seen by each individual cone type. This would overcome the current resolution limitations of my designs, although not providing a perfect solution because of the hight costs and a narrow field of view.

The 180° scanner increases the field of view but can only measure an individual line and therefore does not provide a full image like the 60° scanner. One major advantage of my hyperspectral scanners is that they can be further modified, and in this case additional motors could be added to move the whole 180° scanner in small increments to take vertical line scans right next to each other to build up a full image. As with the 60° scanner, adding individual measurement points to the scan increases the time an individual scanned image requires and increases the risk of disruptions. This creates a trade-off point to the feasible measurement time and accuracy for the scans (see further discussion in Chapter 2).

# *CHAPTER 4 – Prey detection in zebrafish larvae relies on UV light*

In this chapter I present my results from a published paper:

Yoshimatsu T[§], Schroeder C, Nevala NE, Berens P, Baden T[§]. 'Fovea-like Photoreceptor Specializations Underlies Single UV Cone Driven Prey-Capture Behaviour in Zebrafish', *Neuron*. 107, 1-18.

I also present additional experiments on paramecium detection distance and UV versus green light conditions for prey detection.

**4.1 Introduction**

In nature, larval zebrafish live in shallow, protected side pockets of water and human made rice paddies (Spence *et al.*, 2006). These sites protect them from predators but also provide a good source of plant- and zooplankton, such as paramecia or daphnia (Spence *et al.*, 2006). The larvae start foraging at 4-5 *dpf* when they start to run out of nutrients from their yolk sac (Lawrence, 2007). Already at this stage, they have a fully developed cone vision array but lack functional rod photoreceptors (Raymond, Barthel and Curran, 1995; Schmitt and Dowling, 1999). This strongly indicates that prey detection must be cone driven.

In zebrafish larvae, prey detection initiates a series of eye and tail movements in order to move the body so that the prey becomes situated in the upper front visual field for better inspection. If these movements are successfully executed, the prey is then observed with the ventro-temporal part of the retina (*area temporalis*, aka. "strike zone") with high UV cone density (Zimmermann *et al.*, 2018; Yoshimatsu *et al.*, 2020). The locomotor responses are characterised by eye convergence bringing the prey item in the binocular view in front of the fish with simultaneous tail movements (Figs. 4.1A-B) (Bianco, Kampff and Engert, 2011; Patterson *et al.*, 2013; Trivedi and Bollmann, 2013). While the degree of eye convergence is highly stereotyped, the location of the prey item in visual space determines how strongly the fish will response with the tail flicker, as prey items further away require stronger swim bouts for the fish to get closer.

Most previous studies on larval prey detection behaviour have been done under broad spectrum ("white") or long-wavelength biased infrared light (McElligott and O'Malley, 2005; Bianco, Kampff and Engert, 2011; Patterson *et al.*, 2013; Semmelhack *et al.*, 2014; Jouary *et al.*, 2016; Muto and Kawakami, 2018). The details on what extend the white light conditions excited each cone type remains unclear. However, in 2016 Novales Flamarique demonstrated how adults of a transgenic zebrafish line with diminished UV cone population show reduced foraging performance towards paramecia when compared to a wild-type line with normal vision. Both

distance from the tip of the head to the paramecium and the angle of how far to the sides the paramecium could be detected when triggering the first responses are decreased in fish without functional UV vision. These suggest that the UV channel helps to achieve a better contrast against the background to detect the small prey items. In addition, previous research has shown how at least in principle, a UV channel alone could be used to detect UV dark silhouettes and possibly UV bright prey items in otherwise crowded visual environment (Browman, Novales-Flamarique and Hawryshyn, 1994; Novales Flamarique, 2013; Cronin and Bok, 2016).

In Yoshimatsu *et al.*, 2019 we demonstrate with a simple DIY filter camera setup (Figs. 4.2A-B) how paramecia are visible in a naturalistic tank when pictures are taken with UV filters (bandpass 245-400 nm) but not with "yellow" filters (bandpass 485-565 nm) (Fig. 4.2C, data by Takeshi Yoshimatsu). Based on this and previous studies (Novales Flamarique, 2013, 2016) UV light seems to play an important role in zebrafish prey detection. To test whether or not the UV light is important to see prey, here I demonstrate my behaviour experiments on 6-8 *dpf* zebrafish larvae under UV, red and green light conditions. I show how the reaction frequency towards freely moving paramecia is always higher under UV light, with clearly diminished reactions under red and green light. For the first time, this study provides an important example on how different spectral cues from the environment can be used as individual channels in addition to complementing each other in zebrafish larvae prey detection behaviours.

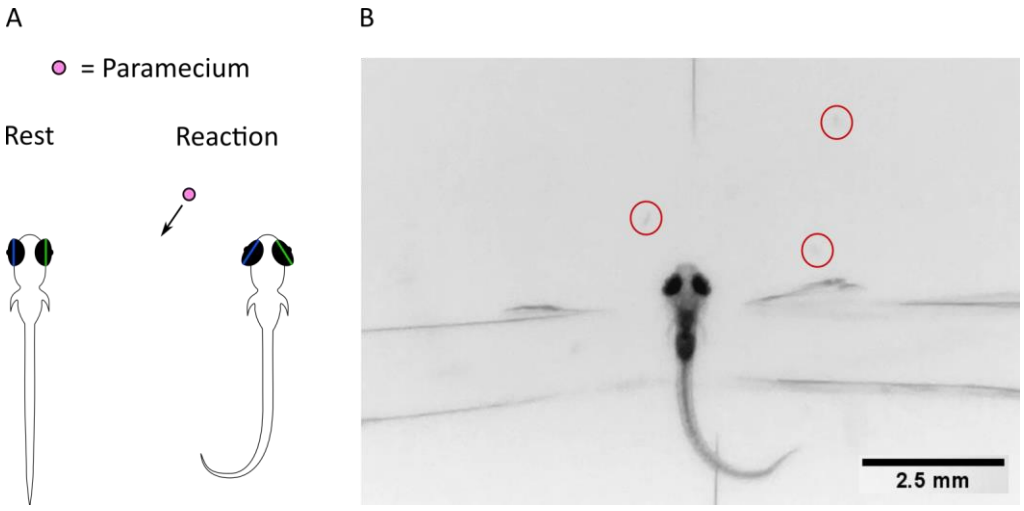


**Figure 4.1. A)** A schematic illustration of a zebrafish larva when at rest and after a paramecium triggers eye convergence and tail flip reactions. **B)** A screenshot from an experimental video with the larva demonstrating a prey detection reaction. Three nearby paramecia circled in red.

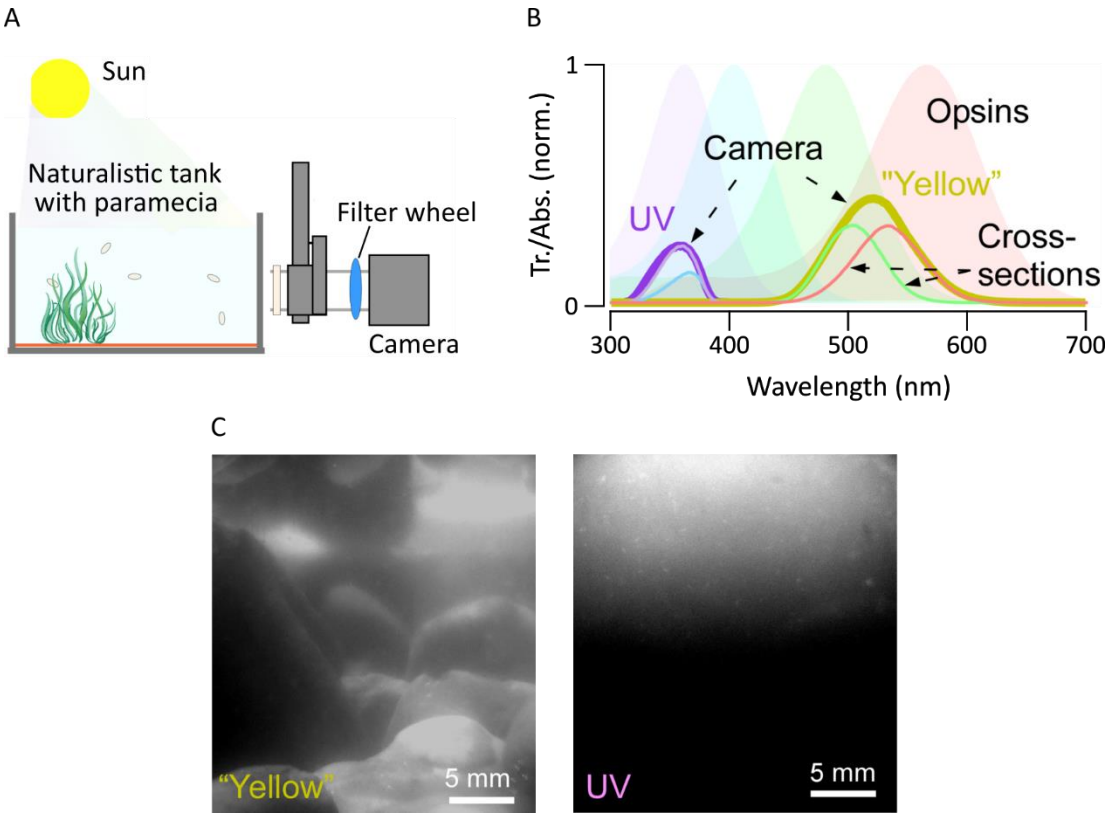


**Figure 4.2.** Paramecia are detectable only through a UV filter. **A)** The setup for taking filtered images from a naturalistic tank with paramecia. **B)** Visual pigment absorbance (Abs.) spectra for UV, blue, green and red cones in zebrafish larvae and transmission (Tr.) spectra for UV and "yellow" filters used in the setup. **C)** Pictures of the same scene taken with the yellow and UV filters. Yellow filter transmits longer wavelengths providing structural details from the scene while excluding small paramecia, whereas the UV picture only shows UV bright paramecia in the upper part of the water column. Modified from (Yoshimatsu *et al.*, 2019, data by Takeshi Yoshimatsu).

## 4.2 Methods

### *4.2.1 Animals*

All procedures were performed in accordance with the UK Animals (Scientific Procedures) act 1986 and approved by the animal welfare committee of the University of Sussex. Both AB Wild Type and nfsB-mCherry transgenic line zebrafish larvae at the age of 6-8 *dpf* were used (Yoshimatsu *et al.*, 2016). Animals were housed at a steady 28.5 °C temperature with 14:10 day-night cycle and fed 3 times a day with normal dried fry and live paramecia once a day from 4 *dpf* onwards.

High concentration stocks of *Paramecium caudatum* (Sciento P320: Paramecium caudatum) were used to start ongoing culture bottles. To start a culture, dry hay was boiled for 20 minutes following 24-48h drying before transferring to 1,000 ml bottles. 10-20 ml of the paramecia stock

was added to each bottle, followed by 700-800 ml of reverse osmosis water. The bottles were renewed every 14-18 days by filtering the existing bottles with 70 µm Falcon cell strainer to create a new starting stock with high concertation of paramecia.

*4.2.2 UV cone ablation in nfsB-mCherry line*

On the day preceding behaviour experiments, the nfsB-mCherry line zebrafish larvae were placed in petri dish with fish system water with 10 mM concentration of metronidazole (M3761-5G, Sigma-Aldrich) for two hours before returning to normal fish system water. nfsB-mCherry line fish express the bacterial nitroreductase enzyme (NTR) with Opn1sw1 promoter in the UV cones (Yoshimatsu *et al.*, 2016). Metronidazole reacts with the NTR and transforms into cytotoxin that kills the UV cones. Before metronidazole treatment the expression of the enzyme in the UV cones was confirmed with the expression of fluorescent protein under fluorescent microscope. With the nfsB-mCherry line UV cones can be ablated from the retina without altering the blue, green and red cone densities.

*4.2.3 Experiment setup*

Three UV LEDs (Thorlabs LED370E - 375 nm Epoxy-Encased LED, 2.5 mW, T-1 3/4), a red-green-blue (RGB) LED ring (NeoPixel 1/4 60 Ring - 5050 RGB LED with Integrated Drivers) and an infrared (IR) sensitive Raspberry Pi camera were attached to the ceiling of a light-tight box (Fig. 4.3B). The peak sensitivities for the LEDs used in these experiments were at 621 nm (red), 507 nm (green) and 375 nm (UV) (Fig. 4.3A). An IR LED plate (Roithner LaserTechnik L2X2-I5LA, 940 nm, 24 x 20 mW/sr, 400 mA, Uf: 6 VDC, 120°) was mounted on a 3D printed holder with a diffuser and a small (⌀ 35 mm) petri dish above holding the fish during an experiment. The whole system was used with Raspberry Pi 3 Model B+ with a modified version of the FlyPi (Chagas *et al.*, 2017) to control the LEDs and the camera.

An individual larva was mounted in 2% low melting point agarose (Fisher Scientific, Cat: BP1360-100) strip to prevent free swimming but still allowing free movement for eyes and tail (Figs. 4.1B and 4.3B) approximately in the middle of a ⌀ 35 mm petri dish for each experiment. Immediately after mounting the dish was filled with fish systems water. The fish were left to rest for a minimum of 2 hours before the start of a recording. After the resting time paramecia were added to the dish with a mounted larva. The number of paramecia in the dish was considered to be appropriate when the camera view in the setup had constantly at least one paramecium

swimming around. To make sure that the fish were able to move their eyes and tail, each fish was tested by moving a pair of tweezers right in front of it to create a startle response with both eye and tail movements. If fish did not react, it was excluded from recordings. Next, the dish was placed in the behaviour box and left to rest for 5 minutes in darkness before starting the recording. Infrared was turned on to make sure the number of paramecia in the dish was sufficient to have a continuous flow of them going around the fish. For the first experiments, 2-minute videos under UV and red lights were taken for three cycles (total of 12 minutes) for each fish (Fig. 4.3C). For the second set of experiments, each recording consisted of 20 one-minute recordings under alternating UV and green light.

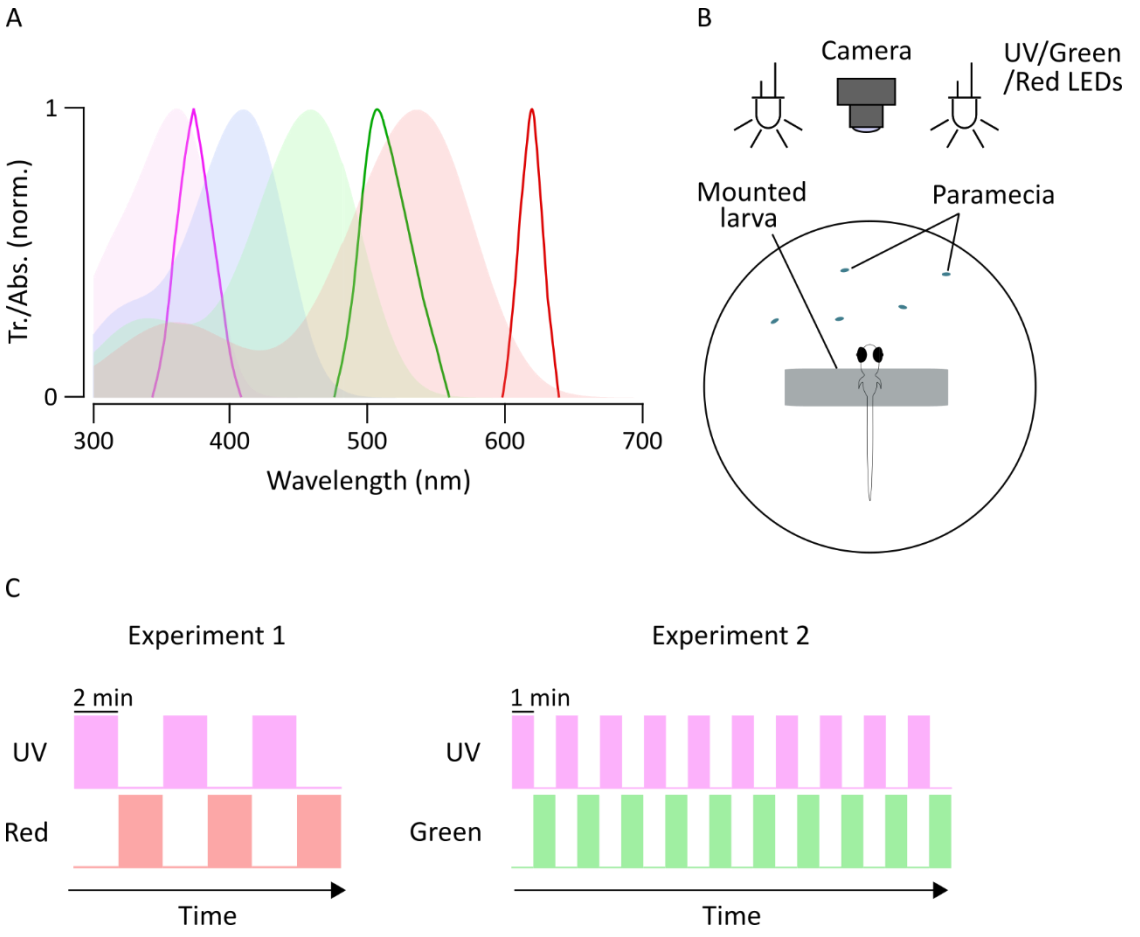


**Figure 4.3.** Behaviour experiment setup. **A)** Visual pigment absorption (Abs.) curves (shaded background) and transmission (Tr.) spectra for UV, green and red LEDs (solid pink, green and red lines, respectively). **B)** For each experiment, an individual 6-8 *dpf* zebrafish larva was mounted on a petri dish with agarose. The fish was covered with fish system water with freely swimming paramecia. Against infrared background illumination, the fish were recorded from above with IR sensitive camera. **C)** Top illumination with red/green/UV LEDs was altered in every 2 minutes (UV vs. red experiment) or in every minute (UV vs. green experiment).

*4.2.4 Data analysis*

Each video recording lasted for 70 seconds. The first 10 seconds were excluded from analysis to diminish the effect of increased activity after the light conditions changed (Burgess and Granato, 2007). Prey detection behaviours towards a single paramecium were annotated manually afterwards. From *n* = 7 wild-type fish in UV vs. red experiments it was also possible to measure the distance from the tip of the fish nose to the paramecium when the response was first triggered. These distances were calculated with self-made scripts on IGOR Pro 7 (Wavemetrics) and Fiji (NIH). Statistical significances were calculated with Wilcoxon Signed Rank Test for paired data when comparing light conditions within each fish line and Mann-Whitney Wilcoxon test for unpaired data when comparing fish lines to each other (threshold $p<0.05$).

**4.3 Results**

At first, I took video recordings from both wild-type (hereafter "WT", *n* = 12) and UV cone ablated zebrafish line (*n* = 6) for total of 12 minutes, alternating 2 minutes in UV and 2 minutes in red light for three cycles. The red LED was first chosen as the opponent condition to UV as the red-light transmission is only activating the red sensitive cones while completely ignoring green, blue and UV cones (Fig. 4.3A). This provided a good opportunity to compare the two extremes of short and long wavelengths. The WT fish showed significantly more reactions per minute towards freely swimming paramecia under UV than red light (Fig 4.4A). Fish without properly functioning UV cones did not show any difference between the two light conditions but had a higher number of reactions under red light than the WT fish. In addition, WT fish reacted more frequently under UV light than the fish with ablated UV cones in the same light conditions.

In most WT videos, several paramecia were present that could have triggered the prey detection behaviours. However, in some instances it was possible to clearly determine which paramecium evoked the reaction under UV light. In these cases, the distance from the tip of the fish nose to the paramecium was measured (Figs. 4.4B-C). Figure 4.4B shows all the paramecia that evoked a response in relation to the location of the fish (*n* = 7 WT fish, 47 individual paramecia) and Figure 4.4C the distribution of detection distances. Although most of the paramecia fall in the distance range of 1-2.5 mm, larvae appear to be able to detect prey items at up to 4.5 mm distance.

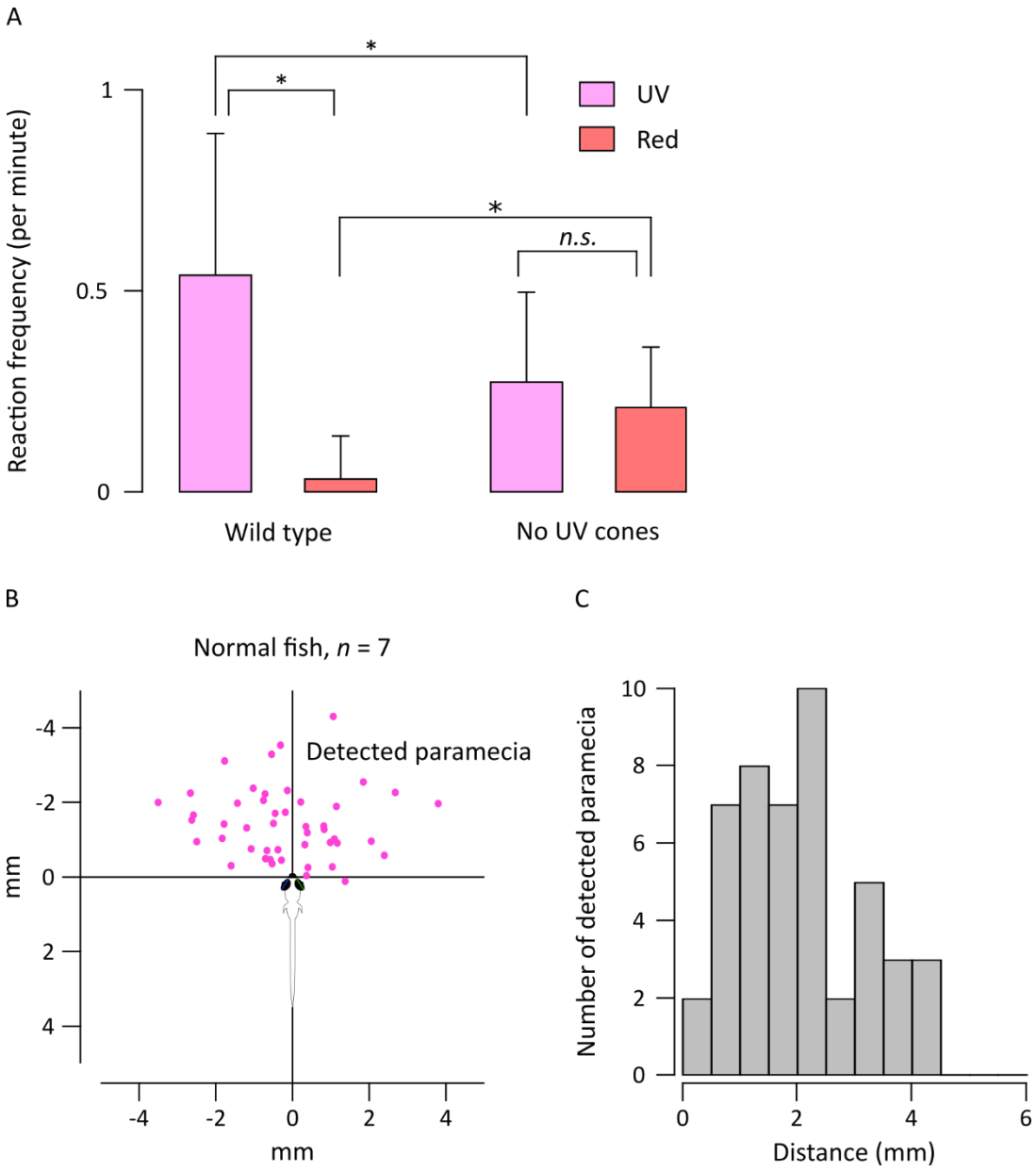


**Figure 4.4.** UV vs red light experiment results. **A)** Wild type fish with normal vision show prey detection behaviours more frequently under UV than red light. Fish without UV cones ("No UV cones") show no difference between light conditions but have higher reaction frequency under red light than the wild type fish. UV vs. red light condition comparisons within wild type (*n*=12) and UV cone ablated (*n*=6) fish lines: paired Wilcoxon signed rank test, p=0.0019 and p=0.14, respectively. WT vs. UV cone ablated fish lines compared under UV light and red light: Mann-Whitney Wilcoxon test for unpaired data, p=0.000026 and p=0.032, respectively. **B)** The location of 47 detected paramecia in relation to a zebrafish larva. **C)** The distribution of paramecia detection distances. B and C data only from WT fish under UV light.

Although the UV vs. red experiments show a clear difference between the two light conditions and two fish lines, several aspects needed improving. First, to gain better understanding how the long wavelength sensitive green and red cones together compare to the now well-assumed, prey detection driving UV channel, the light condition pair was changed to UV vs. green. The

green LED activates rather equally both green and red cones, with minimal contribution to blue cones while still ignoring the UV cones (Fig. 4.3A). Second, the power inputs from UV, green and red LEDs were measured. In the previous UV vs. red experiments the power from UV LEDs was higher than that from the red LEDs. Accordingly, a perceived-brightness effect could also partly explain the differences. To overcome this experimental bias, the power inputs for UV and green LEDs were subsequently equalized for a second set of experiments (Fig. 4.5). Third, the sample size for UV cone ablated line (*n*= 6) was not high enough to make consistent conclusions. This was fixed for the next set of experiments.

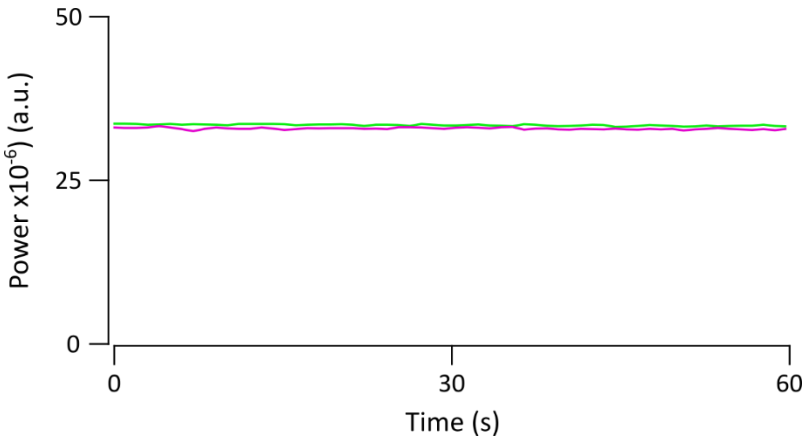


**Figure 4.5.** Power inputs for green and UV (pink) LEDs after power equalization during one measurement video in the UV vs green experiments. Power outputs remained stable over prolonged use.

For the second set of experiments, WT (n = 11) and UV ablated (n = 13) fish lines were recorded over 20 minutes in 1-minute intervals between UV and green light (Figs. 4.3C and 4.6A). Figure 4.6A shows all individual reactions in both light conditions over the course of the total experiment time. Overall the results are in line with the first set of UV vs. red experiment. Wild type fish with normal vision reacted over two times more often in total than the UV cone ablated line (53 and 23 reactions, respectively). Under UV light, WT fish had a significantly higher reaction frequency than the UV cone ablated line, or when simply compared to green light conditions (Fig. 4.6B). In addition, fish without UV cones showed more often prey detection behaviours under green light than WT fish under green light. However, there was no considerable difference between green and UV light conditions when the fish did not have UV cones.

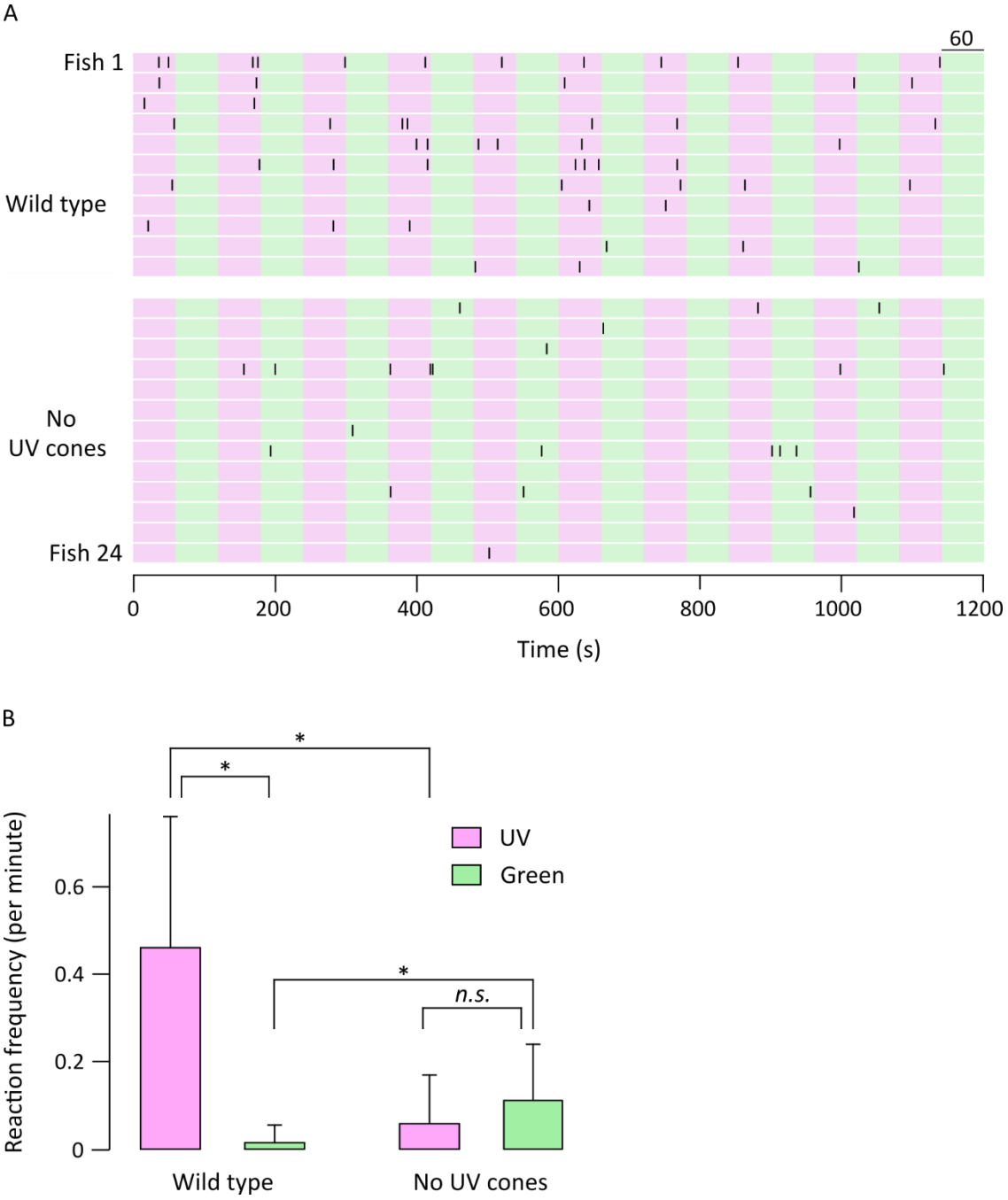


**Figure 4.6.** UV vs. green experiments show similar results as the UV vs. red experiments. **A)** A raster plot showing all reactions in wild type and UV cone ablated fish lines ("No UV cones") over the total experiment time under alternating UV and green light. **B)** WT fish have significantly higher reaction frequency under UV than green light and when compared to fish without UV cones under UV light. Fish without UV cones react to paramecia more often under green light than fish with normal vision but did not have a difference when compared to UV light conditions. UV vs. green light condition comparisons within wild type (*n*=11) and UV cone ablated (*n*=13) fish lines: paired Wilcoxon signed rank test, p=0.0019 and p=0.14, respectively. WT vs. UV cone ablated fish lines compared under UV light and green light: Mann-Whitney Wilcoxon test for unpaired data, p=0.000026 and p=0.032, respectively.

These results clearly demonstrate how zebrafish larvae rely on UV light in prey detection. However, this does not mean that they are completely blind for paramecia under other light conditions. The larvae still show some reactions towards these prey items under green light, but the frequency is greatly reduced.

**4.4 Discussion**

Several fish species living in habitats ranging from coral reefs to fresh waters are known to have UV light sensitive cones in their retina (Cronin and Bok, 2016). UV light can be used to detect dark silhouettes against bright background to aid predator detection, or to see UV bright prey items in otherwise crowded visual environment (Browman, Novales-Flamarique and Hawryshyn, 1994; Nava, An and Hamil, 2011; Cronin and Bok, 2016; Novales Flamarique, 2016). Small zooplankton, such as paramecia, scatter UV light making them appear as bright, small dots in the short wavelength rich upper part of the water column (Fig. 4.2C) (Novales Flamarique, 2013; Zimmermann *et al.*, 2018; Yoshimatsu *et al.*, 2020). In zebrafish larva, detection of such prey items triggers a series of characteristics locomotor behaviours such as eye convergence and tail flicker in order to get closer before the actual prey capture event (Bianco, Kampff and Engert, 2011; Patterson *et al.*, 2013; Mearns *et al.*, 2019). In line with predictions from the previous studies (Novales Flamarique, 2013, 2016; Cronin and Bok, 2016), here I have demonstrated how zebrafish larvae use UV light to detect prey. Reactions towards freely moving paramecia were significantly reduced under red and green light compared to UV light, suggesting that short wavelengths indeed are the most important source for providing visual cues of nearby prey items. To demonstrate that these behaviours rely on visual cues detected by UV cones, I performed the same studies with a transgenic zebrafish line that had UV cones ablated. In general, fish without UV cones reacted to paramecia less frequently and importantly did not show any difference when UV light condition was compared to red or green lights. As the UV cones are removed from the transgenic line, this could simply mean that the fish are mostly blind under UV light, with the blue cones occasionally getting excited by the paramecia swimming by. In addition, the reasons behind the fact that the reaction frequency under red and green light increases with the mutated fish are intriguing. As the input from UV cones is removed, there could be a change in strategy to detect the prey that involves more other cones. To more carefully define whether these reactions are due to simple chance, additional experiments in darkness should be done in future.

Previous research has shown how the artificial stimulus needs to be small enough and move at appropriate speed to create prey capture behaviours (Bianco, Kampff and Engert, 2011; Semmelhack *et al.*, 2014). In addition to these parameters, I can now suggest that to create most naturalistic visual cues in controlled environments, the stimulus should also comprise UV light. Since previous experiments in "white" light conditions without UV have also been efficient enough to elicit needed behaviours towards live or artificial stimuli (McElligott and O'Malley, 2005; Bianco, Kampff and Engert, 2011; Patterson *et al.*, 2013; Semmelhack *et al.*, 2014; Muto and Kawakami, 2018), other wavelengths of light in addition to UV might provide visible cues from the nearby prey. In my setup the UV LED transmission spectrum aligns rather perfectly with the UV cone absorbance spectrum peak. However, as the absorbance spectra from UV and blue cones overlap, the role of the blue cones cannot be completely ignored, especially since the red and green LED transmission spectra have mostly excluded the blue cones. This could be one important difference to the above-mentioned studies with "white" light, as the broad spectrum light stimulator is likely to excite the blue cones as well.

Since the UV LED stimulus in my experiments overlaps significantly with both UV and blue cone absorbance spectra, it is not possible to rule whether the zebrafish larvae detect UV bright paramecia through single channel achromatic contrast or with chromatic contrast with UV and blue light. Naturally, next steps include testing the role blue cones might play in these behaviours. Unfortunately, this cannot be resolved by simply adding a blue LED in the system as that would excite not just blue and UV cones but also green cones and the beta band of the red cones. To better understand how individual cone channels affect the prey detection circuits on the behaviour level, different transgenic lines can be used to create fish that does not lack just one cone type but two different cones (or ultimately, all but one type). Several possible combinations, e.g. fish lacking UV and blue cones or green and red cones, can be utilised. In addition, it is equally important to test different light stimulus combinations. This way it can be better understood if the UV cones alone drive the most efficient prey detection, or whether inputs from other cones together with UV channel further increase the reaction frequency and detection distance. This approach would further distinguish if the paramecia are truly detected via achromatic contrast with single cone channel and the possible role of short wavelength (UV vs. blue) colour vision.

Currently the RGB LED ring in the setup has transmission peaks most suitable for human trichromatic colour vision and is significantly different from zebrafish cone absorption spectra. Although the red and green LEDs provided a good comparison to the better situated UV LEDs, this can be easily improved by inserting RGB LEDs with peak transmissions closer to the peak

spectral sensitivities of the zebrafish red, green and blue cones. In addition, the equalised power inputs from the LEDs are not the perfect representation of the naturalistic light source. As discussed in Chapter 3, in nature most light is available in the range of green and red light (450-600 nm), with UV cones getting least excitation (Zimmermann *et al.*, 2018). Adjusting LED power inputs closer to that of nature spectral environment could alter my current results drastically. However, light spectrum variations in natural habitats are highly complicated across visual space and possibly vary over time of the day and seasons over the year. Therefore, fine tuning the light stimulus in this way in laboratory settings might over-complicate the setup conditions to a point where the results become difficult to interpret.

Zebrafish larvae have a high density of UV cones in the ventro-temporal part of the retina ("strike zone") looking towards the upper front part of the scene (Zimmermann *et al.*, 2018). After a paramecium detection has triggered the eye convergence reaction, these strike zones from both eyes overlap further increasing the UV cone density in the binocular field of view (Yoshimatsu *et al.*, 2020). In line with my findings under UV light with wild type fish, previous research on prey detection under broad "white" light demonstrated how most paramecia are detected within 1-2 mm (Bianco, Kampff and Engert, 2011). However, in those experiments the maximal distance remained within 3.5 mm, whereas I found that the fish can detect paramecia up to 4.5 mm away. Based on the number of UV cones in the strike zone, a 100 µm sized paramecium can be viewed only with a single UV cone at 3 mm distance (Yoshimatsu *et al.*, 2020). Remarkably, as the wild type fish with normal vision can see and react to paramecia up to 4.5 mm away (Fig. 4.4C), the whole prey capture behaviour cascade can presumably be initiated with a signal starting only from a single cone at a time. Alternatively, the paramecium might sequentially pass multiple cones and triggering the response. As the red and green light stimuli were capable to trigger some reactions as well, further studies are needed to see whether or not there are differences in the detection distance between different cones. In addition, although UV cones in general can react either to UV light turning on or off, the cones in the strike zone are especially tuned to react only for UV bright stimulus (Yoshimatsu *et al.*, 2020). This further supports the idea that the UV cones in the strike zone create a specific channel to detect UV bright prey items, such as paramecia in the upper part of the visual field.

Using head-mounted larvae facilitate the analysis of specific eye and tail movements. However, as the larva cannot actually strike and capture the prey in the end, the real role of the UV cones in the prey capture efficiency cannot be studied with the current setup. Some behaviour studies on prey capture with freely moving larvae have been done previously, but these have mostly focused on prey detection distances and angles under white light (Bianco, Kampff and Engert,

2011; Patterson *et al.*, 2013; Muto and Kawakami, 2018). Additional studies with freely foraging larvae under different light stimuli are needed to fully understand whether or not the zebrafish can just see but also eventually capture their prey more efficiently under UV light.

# *Chapter 5 – General discussion*

Colour vision in daylight or photopic light levels is based on cone photoreceptor inputs to the neuronal circuits of the retina where the spectral information is further processed before reaching the brain (Baden and Osorio, 2019). Here, signals from both eyes via ganglion cell axons are analysed in context of previous experience and other sensory inputs (Rodieck, 1998; Chiu and Weliky, 2004; Kuai *et al.*, 2019). Integrating chromatic and achromatic information together allows the brain to generate an internal representation of the outside world with an addition of more specific details that can elicit behavioural responses (Mullen, 1985; Lind and Kelber, 2011).

The capacity for colour vision varies for each animal species, for example, based on the types and distributions of rod and cone photoreceptor cells, conformation of the ocular media (cornea, lens and vitreous), size and location of the eyes and the features of the neuronal layer of the retina. These details of the eyes are often adapted to extract necessary spectral information for survival from their natural habitats (Osorio and Vorobyev, 1996; Lind *et al.*, 2017). As the spectral conditions have major differences not just between terrestrial and underwater environments but also within the same habitat (Chiao, Cronin and Osorio, 2000; Tedore and Nilsson, 2019), different species living in the same place can receive different information for their survival. In addition, the type of behavioural response a visual stimuli can trigger might change between species and can be drastically different depending on their ecological needs (White *et al.*, 1994; Altshuler, 2001). Because of this, it is important to carefully study the natural spectral environment an animal is living in in context of their visual properties to fully understand what their eyes are designed to see and how their behaviour patterns relate to this information.

In this thesis, I have demonstrated how my low-cost, self-made hyperspectral scanners (Chapter 2 and 3) can take high spectral resolution measurements from terrestrial and underwater environments. In Chapter 2 I also showed how these measurements can be analysed with virtually any known animal spectral sensitivity. In this way it is possible to understand how the number of different cone types and their spectral sensitivities affect the amount of chromatic details visible in the scene. As the central focus of thesis is on zebrafish, I then characterised their natural spectral environments in the Indian subcontinent (Chapter 3). This revealed that while the average light spectrum is mostly stimulating green and red cones in these habitats, there is a colour rich zone area around the horizon with short wavelength dominating upper part of the visual field and long wavelength dominating bottom. This upper part of the visual field is rich in UV light, which aids zebrafish larvae to detect UV bright paramecia as prey. Then, in Chapter 4 I demonstrate with behaviour experiments on larval zebrafish how UV light is the most important cone channel to detect UV bright prey items when compared to red or green

light conditions. This further proves how different cone channels alone can detect important visual features that drive crucial behaviour responses for survival.

### 5.1 Spectrometer based hyperspectral scanners provide high spectral resolution details

One of the main goals of this thesis was to design and build low-cost hyperspectral scanners to take high spectral resolution light measurements in underwater environments (Chapter 2 and 3). Although my spectrometer based approaches are somewhat similar to Baden *et al.* (2013), they are substantially different from previous studies that have mainly used sets of narrow bandpass interference filters in front of a wide spectrum (400-700 nm) sensitive CCD cameras (Nagle and Osorio, 1993; Osorio, Ruderman and Cronin, 1998; Párraga *et al.*, 1998; Ruderman, Cronin and Chiao, 1998; Chiao, Cronin and Osorio, 2000). While this filter-based method also creates hyperspectral datasets, my scanners with sub-nm spectral resolution provide notably more accurate light spectrum measurements. This is especially useful when studying fine differences in cones spectral tunings between species (Chapter 2, Nevala and Baden, 2019) or within species. Zebrafish is a particularly useful example of the latter, as they have four different options for green cone opsins and two for red cone opsins (Chinen *et al.*, 2003; Takechi and Kawamura, 2005b). The $\lambda_{max}$ differences between the opsin types are fairly subtle (9-38 nm in green cones, 10 nm in red cones) and the most commonly expressed opsin changes as the fish develops from young larva to adult (Robinson, Schmitt and Dowling, 1995; Chinen *et al.*, 2003; Takechi and Kawamura, 2005b). How these small changes in spectral sensitivity over the fish lifetime affect the chromatic details visible in their natural habitats could not be studied with methods that cannot separate such small variations. As the larvae and adult zebrafish have different behavioural goals (feeding vs. mating), it is tempting to assume that they need to extract different spectral information from their surroundings.

While my 60° image forming scanner provides good spectral details, it does not reach the same spatial resolution as the commercially available camera systems. Because light has to go through an elongated slit to reach the sensor in the spectrometer, my 60° image forming scanner has a ~4.2° horizontal x ~9.0° vertical resolution (Chapter 2, Nevala and Baden, 2019). The 4.2° is close to the 3° behavioural resolution in zebrafish larvae when tracking stripes (Haug *et al.*, 2010). However, this falls far behind the spatial acuity adult zebrafish can resolve (~0.6°). Because of this, my method alone is not comprehensive enough to provide comparable details between adult and larvae zebrafish. As discussed in Chapter 2, improving the spatial resolution on the 60° image forming scanner would not be straightforward without compromising the time each scan

requires. As no method alone is perfect, complementary approaches should be used. One solution for this could be the multispectral approach where specifically designed filters represent the absorbance spectra of each cone photoreceptor type in the animal's retina (Tedore and Nilsson, 2019). Together with a high spatial resolution camera, this multispectral approach provides species-specific spectral data from the scene and could fulfil the current shortcomings on my designs.

One major advantage of designing and building one's own equipment is that they can be easily modified for different needs without major financial investment. Indeed, open access "DIY science" has become increasingly popular to reduce costs of the often pricy commercial options, provide solutions for more complicated research questions that do not have easily available equipment and to make science available for everyone regardless of their accessibility to state-of-the-art equipment (Marder, 2013; Goble, 2014; Maia Chagas, 2018). My scanners were designed to overcome financial limitations, but at the same time to find a way to take light measurements in underwater scenes that have been under represented in natural imaging studies (except see Chiao, Cronin and Osorio (2000) and Johnsen *et al.* (2013, 2016)). In addition, my scanners provide spectral details deep in the UV that has been lacking from previous studies. To further contribute to the open access scenery, all instructions to build my low-cost, 60° image forming scanner are readily available online (https://github.com/BadenLab/Hyperspectral-scanner) in addition to my open access database for the 60° scanner data (https://zenodo.org/communities/hyperspectral-natural-imaging) (Chapter 2, Nevala and Baden, 2019).

### 5.2 Spectral characterisation of zebrafish's natural environment

Zebrafish live on the Indian subcontinent in shallow side pockets of larger water bodies and in slowly moving streams (McClure, McIntyre and McCune, 2006; Engeszer *et al.*, 2007; Parichy, 2015). In Chapter 3 I first showed examples of these natural environments and then explicitly described the spectral variations based on my measurements with the 60° image forming scanner and the 180° vertical line scanner. Previous studies have shown how light becomes more monochromatic in water with increasing depth and how this narrow light spectrum at the bottom is shifted towards longer wavelengths in fresh waters (Levine and MacNichol, 1982; Chiao, Cronin and Osorio, 2000). My results from the 180° scanner demonstrate similar constriction in the spectral range: as the light intensity decreases with increasing depth, the spectral peak is shifted approximately 60 nm towards the longer wavelengths from 524 nm at

the top of the water body to 586 nm at the bottom (Chapter 3, Fig. 3.6). For each scan, the 60° scanner was always placed to point directly towards the horizon. The average spectrum from all individual spectra from these measurements demonstrate a slight redshift when compared to the peak sensitivity of the red cones at 548 nm (Chapter 3, Fig. 3.4). In line with this, the E-I zones covering the horizon and areas below that show similar shift towards longer wavelengths in the 180° scanner dataset. Zebrafish larvae have an uneven distribution of different cone types across their retina (Zimmermann *et al.*, 2018). My results from the spectral distributions match well with these, as the long wavelength sensitive green and red cones are mostly looking towards horizon and the bottom. Interestingly, while most of the UV cones are looking short wavelength dominating upper part of scenery, the blue cones are gazing mostly the horizon.

As shown both with action camera data excluding UV and image forming 60° scanner including the whole spectral range (200-1,000 nm), most of the chromatic details for the zebrafish larvae to see are located around the horizon and immediately below that. This chromatically rich zone is squeezed between more achromatic upper and lower parts of the visual field. Functional imaging on bipolar cells in the larval zebrafish eyes has shown that these achromatic and chromatic zones in nature are reflected in the same manner on the different parts of the retina pointing towards these corresponding parts in the visual field (Zimmermann *et al.*, 2018). 2-photon *in vivo* imaging on zebrafish larvae's inner retina reveal a mixture of achromatic, monochromatic and chromatic (colour opponent) responses from bipolar cell terminals (Zimmermann *et al.*, 2018). Interestingly, all these responses from bipolar cells dominate certain areas of the retina indicating functional anisotropies. In line with the PCA results from the zebrafish's natural scenes, all colour opponent bipolar cells are located looking towards the lower and outward-facing visual field. Many of these main colour opponent bipolar cell responses translate further to the following ganglion cell layer, although the role of blue light is more limited and the ganglion cell responses are further complicated by the addition of time aspect (Zhou *et al.*, 2020) In addition, both monochromatic UV responsive bipolar cells and UV-On retinal ganglion cells have highest densities at the strike zone (Zimmermann *et al.*, 2018; Zhou *et al.*, 2020). In line with previous experiments on human chromatic computations (Ruderman, Cronin and Chiao, 1998; Lewis and Li, 2006), most chromatic contrasts visible for zebrafish are done between long and short wavelengths. This main chromatic variance together with achromatic data always cover nearly all variance in the measurements. Only a small part (<1 %) is left for more complex chromatic details. This is further represented in the larval zebrafish's bipolar colour opponent bipolar cells, as 80% of these responses compute short versus long wavelength antagonisms (Zimmermann *et al.*, 2018). From this data, it cannot be

clearly interpreted what these small details could mean for the fish. Further measurements with a higher spatial resolution setup, such as the multispectral filter camera by Tedore and Nilsson (2019), are needed to supplement my existing datasets. This would also make possible to compare the differences in the spectral inputs available to the adult and larvae zebrafish to understand how different their visual worlds actually are.

Like many other vertebrates, zebrafish are known to have two options for the chromophore bound to their opsins: 11-cis-retinal and 11-cis-3,4-didehydroretinal or A1 and A2 vitamins, respectively. Changing the chromophore from A1 to A2 redshifts the spectral sensitivity of the middle and long wavelength sensitive cones approximately 20-60 nm. As the existence of A2 vitamin in zebrafish has only been demonstrated in laboratory conditions after thyroid hormone treatment (Allison *et al.*, 2004; Enright, Toomey, Sato, *et al.*, 2015) the common understanding is that the zebrafish always have A1 vitamin as a chromophore. However, evidence from wild fish in nature is lacking. In addition, previous spectral sensitivity measurements directly from the cone outer segments have been done in adults (Allison *et al.*, 2004; Enright, Toomey, Sato, *et al.*, 2015). Thyroid hormone levels change during the zebrafish development, with peak at 10-21 *dpf* larvae and decline again as the individual matures to adult (Chang *et al.*, 2012). As the thyroid hormone can cause a change from A1 to A2, the possibility of the spectral sensitivity shift with A2 chromophore cannot be completely excluded. The visual pigments with most common opsins for green and red cones in larval zebrafish have the $\lambda_{max}$ values at 467 and 548 nm (Takechi and Kawamura, 2005b), staying slightly at shorter wavelengths when compared to the peaks of the average spectra in their natural habitats. Changing the chromophore from A1 to A2 could shift the spectral sensitivity of the cones to align better with the general spectrum available. However, the lower activation levels with A2 chromophores makes them thermally more unstable and noisy (Barlow, 1957; Donner, Firsov and Govardovskii, 1990; Ala-laurila *et al.*, 2003, 2007). Because of this, the warm waters zebrafish larvae inhabit might force all the chromophores to be A1 vitamins to increase the signal to noise ratio. Furthermore, several migrating animals are known to change their chromophore in either direction either after metamorphosis (Wilt, 1959; Liebman and Entine, 1968) or when moving to a new environment for breeding (Wald, 1957; Beatty, 1966). Interestingly, thyroid hormone is also known to have some seasonal variation and can affect the reproductive hormone cycle in mammals (Dardente *et al.*, 2019). Although the zebrafish are not known to migrate between different environments during the breeding season between April and August, the possible effect of hormonal changes in adults prior mating cannot be left out. Detailed microspectrophotometer (MSP) measurements from cone outer segments to determine shifts in spectral sensitivity in wild

zebrafish larvae and adults during different seasons are needed to further establish the possible role of the A2 chromophore.

Changes in the light levels between day and night drive internal circadian rhythms in an animal. This visually driven rhythmicity has also been found in zebrafish (Cahill, 1996; Rajendran *et al.*, 1996). After a photon has activated the chromophore bound in the opsin pocket by conformation change and the phototransduction cascade has started, the activated all-*trans*-retinal form of the chromophore is transferred to the pigment epithelium to be transformed back to its original form. This transfer happens with IRPB (interphotoreceptor retinoid-binding protein). During midday with the highest light levels, the expression rates of the IRPB are significantly higher when compared to darkness (Rajendran *et al.*, 1996). As this can lead to changes in photoreceptor sensitivity, different behaviours (such as feeding and breeding) might be timed to happen at certain times of the day. Since the spectrum of light has some variation from dawn to dusk (Mcfarland, Ogden and Lythgoes, 1979; Cronin *et al.*, 2014), the behaviours might also rely on the specific spectral features of the visual cues available at that time. Therefore, future experiments should include spectral measurements through the whole course of the day and during different seasons to reveal possible fluctuations in the observable spectral information. This could reveal not just the small chromatic details driving certain visually guided behaviours but also the possible differences between adult and larvae as they have different main interests, such as mating and feeding, respectively.

### 5.3 UV channel drives prey detection

As discussed, most of the short wavelengths available for zebrafish to see are located at the upper parts of the water body (Chapter 3). UV and blue cones catch most of their photons only from this direction as these parts of the light are quickly absorbed and scattered with organic material dissolved in the water with increasing depth (Levine and MacNichol, 1982). Zebrafish larvae feed on small, organic material and zooplankton, such as paramecia (Arunachalam *et al.*, 2013) that appear as UV bright spots against otherwise crowded visual environment in the zebrafish's field of view (Yoshimatsu *et al.*, 2020).

In Chapter 4 I demonstrated how wild type zebrafish larvae reacted more frequently to the freely moving paramecia under UV light when compared to red and green light conditions. Interestingly, when the UV cones are ablated from the retina and the fish is virtually "blind" in this spectral range, they show an increased reaction frequency towards the prey under red and green light. As this is the first time prey detection behaviours have been studied under different

light conditions, the exact role of each cone type feeding in to the prey detection circuit cannot be determined completely. Especially the input from blue cones was mostly excluded from my red and green light stimuli. Even though these findings predict that UV channel is strongly involved in detecting prey items, previous studies using broad "white" light (assumingly excluding UV) have also successfully initiated prey detection responses (Bianco, Kampff and Engert, 2011; Patterson *et al.*, 2013; Semmelhack *et al.*, 2014). This suggests that blue cones might provide an important input to the circuit initiating prey capture behaviours or that the fish is using a specific combination of several cone channels. Since the fish still responded occasionally to red and green light in my experiments, it is possible that the best light conditions to detect prey involve a broad spectrum of light where the UV channel further enhances the contrast.

Starting from 3 mm distance, one 100 µm sized paramecium can be viewed only with one UV cone when observed with strike zone, the high UV cone density area (Yoshimatsu *et al.*, 2020). My experiments on wild type fish under UV light showed how the fish detected paramecia up to 4.5 mm distance with most events triggered in the range of 1-2.5 mm. Previously it has been recorded that zebrafish can see prey approximately 3.5 mm away, with most detections around 1-2 mm (Bianco, Kampff and Engert, 2011). Although the difference in the maximal detection distance between my experiments and the previous study is small (1 mm), it is possible that the UV channel improves the contrast to see small prey items significantly to increase the detection distance. In theory this could mean that the distance a paramecium is seen with a single UV cone is infinite. However, the scattering and absorbance of short wavelengths especially in these murky fresh waters probably limit the detection distance significantly. Currently data for distance measurements from other light conditions are lacking. Further experiments are needed conclude if the paramecia could be seen at similar distances with other cones as well. As all cone types have slightly different high density areas in the larval zebrafish retina (Zimmermann *et al.*, 2018), it is possible that the reactions towards prey at certain distance under different light conditions depend on angle the item is viewed.

Several studies have suggested that UV light is used not only to detect food items, but can also provide information on possible predators casting dark silhouettes (Nava, An and Hamil, 2011; Cronin and Bok, 2016). The UV cones in the strike zone are tuned to respond best to UV bright items, which further supports the idea of this specified area driving mainly prey detection (Zimmermann *et al.*, 2018; Yoshimatsu *et al.*, 2020). Interestingly, UV cones in other parts of the retina show preferred responses to UV dark stimulation and could be used to see the upcoming predator casting a dark shadow (Zimmermann *et al.*, 2018). Behaviour experiments have

demonstrated how small enough objects trigger a prey detection behaviours, whereas larger stimuli cause escape reactions as the object is possibly interpreted as a predator (Bianco, Kampff and Engert, 2011; Semmelhack *et al.*, 2014). Behavioural assays on adult zebrafish demonstrated how the fish show avoidance responses when presented either a non-UV-reflective cue against UV reflective background or vice versa (Nava, An and Hamil, 2011). When the visual stimuli did not reflect UV light in any manner, the fish showed significantly reduced responses. As the visual stimuli triggering prey detection responses might not depend solely on the size of the stimuli but also on the spectral properties, similarly the visual cue causing escape behaviours could be reinforced by including UV light. As the long wavelength sensitive red and green cones are most suitable to detect general spatial features (rocks, plants) and a dark silhouette from a predator could easily be missed among these larger structures from the scene (Chapter 3, Zimmermann *et al.*, 2018), the UV channel could provide an important route to see the upcoming danger.

From my behaviour experiment results it can be concluded that UV channel plays an important role for prey detection behaviours in larval zebrafish. If and how the other cones contribute to these behaviours or enhance the inputs from UV cones to the circuit still remains unclear. Previous studies on characterizing the functionality of the bipolar cells in the larval zebrafish retina showed how UV channel acts as an individual channel and are not included in the other RGB chromatic computations at this level (Zimmermann *et al.*, 2018). However, it should be noted that this does not mean that further comparisons cannot happen at the following ganglion cell layer or further up in the brain. Understanding how such small and simple visual cues as a UV bright paramecium feeds into the prey detection behaviours demonstrates perfectly how even the seemingly simplest animal can do complex computations to survive in their natural visual world.

# References

Ala-laurila, P. *et al.* (2003) 'The thermal contribution to photoactivation in A2 visual pigments studied by temperature effects on spectral properties', *Visual Neuroscience*, 20(4), pp. 411–419.

Ala-laurila, P. *et al.* (2007) 'Chromophore switch from 11- cis -dehydroretinal (A2) to 11- cis -retinal (A1) decreases dark noise in salamander red rods', *Journal of Physiology*, 1, pp. 57–74.

Allen, A. E., Martial, F. P. and Lucas, R. J. (2019) 'Form vision from melanopsin in humans', *Nature Communications*, 10: 2274.

Allison, W. T. *et al.* (2004) 'Visual pigment composition in zebrafish: Evidence for a rhodopsin-porphyropsin interchange system.', *Visual neuroscience*, 21(6), pp. 945–952.

Allison, W. T. *et al.* (2010) 'Ontogeny of cone photoreceptor mosaics in zebrafish', *Journal of Comparative Neurology*, 518, pp. 4182–4195.

Altshuler, D. L. (2001) 'Ultraviolet reflectance in fruits, ambient light composition and fruit removal in a tropical forest', *Evolutionary Ecology Research*, 3, pp. 767–778.

Arunachalam, M. *et al.* (2013) 'Natural history of zebrafish (Danio rerio) in India.', *Zebrafish*, 10(1), pp. 1–14.

Attneave, F. (1954) 'Some informational aspects of visual perception', *Psychological Review*, 61(3), pp. 183–193.

Baden, T. *et al.* (2013) 'A tale of two retinal domains: Near-Optimal sampling of achromatic contrasts in natural scenes through asymmetric photoreceptor distribution', *Neuron*, 80(5), pp. 1206–1217.

Baden, T. and Osorio, D. (2019) 'The Retinal Basis of Vertebrate Color Vision', *Annual Review of Vision Science*, 5, pp. 3.1-3.24.

Barlow, H. B. (1957) 'Purkinje shift and retinal noise.', *Nature*, 179(4553), pp. 255–256.

Beatty, D. D. (1966) 'A study of the succession of visual pigments in Pacific salmon (*Oncorhynchus*)'', *Canadian Journal of Zoology*, 44, pp. 429–455.

Bianco, I. H., Kampff, A. R. and Engert, F. (2011) 'Prey Capture Behavior Evoked by Simple Visual Stimuli in Larval Zebrafish', *Frontiers in Systems Neuroscience*, 5, pp. 1–13.

Bilotta, J. and Saszik, S. (2001) 'The zebrafish as a model visual system', *International Journal of*

*Developmental Neuroscience*, 19(7), pp. 621–629.

Branchek, T., Bremiller, R. (1984) 'The Development of Photoreceptors in the Zebrafish, Brachydanio rerio. I. Structure', *The Journal of comparative neurology*, 224, pp. 107–115.

Brelstafø, G. *et al.* (1995) 'Hyper-spectral camera system:- acquisition and analysis', *Proc. SPIE*, 2587, pp. 150–159.

Bridges, C. D. B. (1965) 'Absorption properties, interconversions, and environmental adaptation of pigments from fish photoreceptors.', *Cold Spring Harbor Symposia on Quantitative Biology*, 30, pp. 317–334.

Browman, H. I., Novales-Flamarique, I. and Hawryshyn, C. W. (1994) 'Ultraviolet photoreception contributes to prey search behaviour in two species of zooplanktivorous fishes', *Journal of Experimental Biology*, 186, pp. 187–198.

Buchsbaum, G. & Gottschalk, A. (1983) 'Trichromacy , opponent colours coding and optimum colour information transmission in the retina', *Proc. R. Soc. Lond. B*, 220, pp. 89–113.

Burgess, H. A. and Granato, M. (2007) 'Modulation of locomotor activity in larval zebrafish during light adaptation', *Journal of Experimental Biology*, 210(14), pp. 2526–2539.

Cahill, G. M. (1996) 'Circadian regulation of melatonin production in cultured zebrafish pineal and retina', *Brain Research*, 708, pp. 177–181.

Chagas, A. M. *et al.* (2017) 'The €100 lab: A 3D-printable open-source platform for fluorescence microscopy, optogenetics, and accurate temperature control during behaviour of zebrafish, Drosophila, and Caenorhabditis elegans', *PLoS biology*, 15(7): e2002702.

Chang, B. S. W. *et al.* (1995) 'Opsin Phylogeny and Evolution: A Model for Blue Shifts in Wavelength Regulation', *Molecular Phylogenetics and Evolution*, pp. 31–43.

Chang, J. *et al.* (2012) 'Changes in Thyroid Hormone Levels during Zebrafish Development', *Zoological Science*, 29(3), pp. 181–184.

Chiao, C.-C., Cronin, T. W. and Osorio, D. (2000) 'Color signals in natural scenes: characteristics of reflectance spectra and effects of natural illuminants', *Optical Society of America*, 17(2), pp. 218–224.

Chinen, A. *et al.* (2003) 'Gene duplication and spectral diversification of cone visual pigments of zebrafish', *Genetics*, 163(2), pp. 663–675.

Chiu, C. and Weliky, M. (2004) 'The role of neural activity in the development of orientation selectivity', Cambridge, MA: MIT Press.

Cronin, T. W. *et al.* (2014) *Visual Ecology*. Princeton University Press.

Cronin, T. W. and Bok, M. J. (2016) 'Photoreception and vision in the ultraviolet', *The Journal of Experimental Biology*, 219(18), pp. 2790–2801.

Dardente, H. *et al.* (2019) 'An integrative view of mammalian seasonal neuroendocrinology', *Journal of Neuroendocrinology*, 31:e12729.

Donner, K., Firsov, M. L. and Govardovskii, V. I. (1990) 'The frquency of isomerization-like "dark" events in rhodopsin and porphyropsin rods of the bull-frog retina', *Journal of Physiology*, 428, pp. 673–692.

Douglas, R. H. and McGuigan, C. M. (1989) 'The spectral transmission of freshwater teleost ocular media-An interspecific comparison and a guide to potential ultraviolet sensitivity', *Vision Research*, 29(7), pp. 871–879.

Easter Jr., S. S. and Nicola, G. N. (1996) 'The Development of Vision in the Zebrafish', *Developmental biology*, 180(2), pp. 646–663.

ElMasry, G., Sun, D.-W. and Allen, P. (2012) 'Near-infrared hyperspectral imaging for predicting colour, pH and tenderness of fresh beef', *Journal of Food Engineering*, 110(1), pp. 127–140.

Endler, J. (1993) 'The Color of Light in Forests and Its Implications', *Ecological Monographs*, 63(1), pp. 1–27.

Engeszer, R. E. *et al.* (2007) 'Zebrafish in the wild: a review of natural history and new notes from the field', *Zebrafish*, 4(1), pp. 21–40.

Engstrom, K. (1960) 'Cone Types and Cone Arrangement in the Retina of Some Cyprinids', *Acta Zoologica*, 41, pp. 277–295.

Enright, J. M., Toomey, M. B., Sato, S. Y., *et al.* (2015) 'Cyp27c1 red-shifts the spectral sensitivity of photoreceptors by converting Vitamin A1 into A2', *Current Biology*, 25(23), pp. 3048–3057.

Enright, J. M., Toomey, M. B., Sato, *et al.* (2015) 'Cyp27c1 Red-Shifts the Spectral Sensitivity of Photoreceptors by Converting Vitamin A1 into A2', *Current Biology*, 25(23), pp. 3048–3057.

Estévez, O. and Spekreijse, H. (1982) 'The "silent substitution" method in visual research',

*Vision Research*, 22, pp. 681–691.

Feng, L. *et al.* (2019) 'Hyperspectral imaging for seed quality and safety inspection: a review', *Plant Methods*, 15(1), pp. 1–25.

Foster, D. H. *et al.* (2006) 'Frequency of metamerism in natural scenes', *Journal of the Optical Society of America A*, 23(10), p. 2359-2372.

Gahtan, E., Tanger, P. and Baier, H. (2005) 'Visual prey capture in larval zebrafish is controlled by identified reticulospinal neurons downstream of the tectum', *Journal of Neuroscience*, 25(40), pp. 9294–9303.

Giurfa, M. *et al.* (1996) 'Detection of coloured stimuli by honeybees: minimum visual angles and receptor specific contrasts', *Journal of Comparative Physiology A*, 178(5), pp. 699–709.

Goble, C. (2014) 'Better software, better research', *IEEE Internet Computing*, 18, pp. 4–8.

Goetz, A. F. H. *et al.* (1985) 'Imaging Spectrometry for Earth Remote Sensing', *Science*, 228(4704), pp. 1147–1153.

Govardovskii, V. I. *et al.* (2000) 'In search of the visual pigment template', *Visual Neuroscience*, 17(4), pp. 509–528.

Gowen, A. A. *et al.* (2007) 'Hyperspectral imaging - an emerging process analytical tool for food quality and safety control', *Trends in Food Science and Technology*, 18(12), pp. 590–598.

Hancock, P. J. B., Baddeley, R. J. and Smith, L. S. (1992) 'The principal components of natural images', *Network: Computation in Neural Systems*, 3(1), pp. 61–70.

Haug, M. F. *et al.* (2010) 'Visual acuity in larval zebrafish: behavior and histology.', *Frontiers in zoology*, 7: 8.

Hubbard, R. and Sperling, L. (1973) 'The Colors of the Visual Pigment Chromophores', *Exp. Eye Res.*, 17, pp. 581–589.

Hunt, D. M. *et al.* (2001) 'Vision in the ultraviolet.', *Cellular and molecular life sciences : CMLS*, 58(11), pp. 1583–1598.

Jacobs, G. H. and Deegan, J. F. D. I. (1999) 'Uniformity of colour vision in Old World monkeys', *Proc. Biol. Sci.*, 266(1432): pp. 2023–2028.

Jacobs, G. H., Neitz, J. and Deegan, J. F. (1991) 'Retinal receptors in rodents maximally sensitive to ultraviolet light', *Nature*, 353, pp. 655–656.

Johnsen, G. *et al.* (2013) Chapter 20 - Underwater hyperspectral imagery to create biogeochemical maps of seafloor properties, *Subsea Optics and Imaging*, pp. 508-535.

Johnsen, G. *et al.* (2016) 'The use of underwater hyperspectral imaging deployed on remotely operated vehicles - methods and applications', *IFAC-PapersOnLine*, 49(23), pp. 476–481.

Johnsen, S. (2012) *The Optics of Life - A Biologist's Guide to Light in Nature*. Princeton University Press.

Johnsen, S. and Widder, E. A. (2001) 'Ultraviolet absorption in transparent zooplankton and its implications for depth distribution and visual predation', *Marine Biology,* 138, pp. 717–730.

Jouary, A. *et al.* (2016) 'A 2D virtual reality system for visual goal-driven navigation in zebrafish larvae', *Scientific Reports*, 6, pp. 1–13.

Juusola, M. *et al.* (2017) 'Microsaccadic information sampling provides Drosophila hyperacute vision', *eLife*, 6:e26117.

Koskelainen, A. *et al.* (2000) 'Measurement of thermal contribution to photoreceptor sensitivity', *Nature*, 403, pp. 220–3.

Kuai, S.-G. *et al.* (2019) 'Integration of motion and form cues for the perception of self-motion in the human brain', *The Journal of Neuroscience*, 10.

Lagogiannis, K., Diana, G. and Meyer, M. P. (2019) 'Learning steers the ontogeny of an efficient hunting sequence in zebrafish larvae', *bioRxiv*.

Land, M. F. and Nilsson, D.-E. (2012) 'Animal Eyes', Oxford University Press.

Lawrence, C. (2007) 'The husbandry of zebrafish (Danio rerio): A review', *Aquaculture*, 269, pp. 1–20.

Lelong, C. C. D., Pinet, P. C. and Poilve, H. (1998) 'Hyperspectral imaging and stress mapping in agriculture: A case study on wheat in Beauce (France)', *Remote Sensing of Environment*, 66(2), pp. 179–191.

Levine, J. S. and MacNichol, E. F. (1982) 'Color Vision in Fishes', *Scientific American*, 246(2), pp. 140–149.

Lewis, A. and Li, Z. (2006) 'Are cone sensitivities determined by natural color statistics?', *Journal of Vision*, 6, pp. 285–302.

Liebman, P. A. and Entine, G. (1968) 'Visual pigments of frog and tadpole (*Rana pipiens*)',

*Vision Research*, 8, pp. 761–775.

Lind, O. *et al.* (2017) 'Coevolution of coloration and colour vision?', *Philosophical Transactions of the Royal Society B*, 372: 20160338.

Lind, O. and Kelber, A. (2011) 'The spatial tuning of achromatic and chromatic vision in budgerigars', *Journal of Vision*, 11(7):2, pp. 1–9.

Lu, G. and Fei, B. (2014) 'Medical hyperspectral imaging: a review', *Journal of Biomedical Optics*, 19(1), p. 010901.

Maia Chagas, A. (2018) 'Haves and have nots must find a better way: The case for open scientific hardware', *PLoS biology*, 16(9), p. e3000014.

Marder, E. (2013) 'Living science: The haves and the have nots', *eLife*, 2:e01515.

McClure, M. M., McIntyre, P. B. and McCune, A. R. (2006) 'Notes on the natural diet and habitat of eight danionin fishes, including the zebrafish Danio rerio', *Journal of Fish Biology*, 69(2), pp. 553–570.

McElligott, M. B. and O'Malley, D. M. (2005) 'Prey tracking by larval zebrafish: Axial kinematics and visual control', *Brain, Behavior and Evolution*, 66(3), pp. 177–196.

Mcfarland, W. N., Ogden, J. C. and Lythgoes, J. N. (1979) 'The influence of light on the twilight migrations of grunts', *Env. Biol. Fish*, 4(1), pp. 9–22.

Mearns, D. S. *et al.* (2020) 'Deconstructing hunting behavior reveals a tightly coupled stimulus-response loop', *Current Biology*, 30, p. 54-69.

Monteiro, S. T. *et al.* (2007) 'Prediction of sweetness and amino acid content in soybean crops from hyperspectral imagery', *ISPRS Journal of Photogrammetry and Remote Sensing*, 62(1), pp. 2–12.

Morris, D. P. *et al.* (1995) 'The attenuation of solar UV radiation in lakes and the role of dissolved organic carbon', *Limnology and Oceanography*, 40(8), pp. 1381–1391.

Mullen, K. T. (1985) 'The contrast sensitivity of human colour vision to red-green and blue-yellow chromatic gratings', *The Journal of Physiology*, 359(1), pp. 381–400.

Muto, A. and Kawakami, K. (2018) 'Ablation of a Neuronal Population Using a Two-photon Laser and Its Assessment Using Calcium Imaging and Behavioral Recording in Zebrafish Larvae', *Journal of Visualized Experiments*, 136(57485).

Nagle, M. G. and Osorio, D. (1993) 'The tuning of human photopigments may minimize red-green chromatic signals in natural conditions.', *Proceedings of the Royal Society B*, 252, pp. 209–213.

Nathans, J. (1990) 'Determinants of Visual Pigment Absorbance : Identification of the Retinylidene Shiff's Base Counterion in Bovine Rhodopsin', pp. 9746–9752.

Nava, S., An, S. and Hamil, T. (2011) 'Visual detection of UV cues by adult zebrafish (Danio rerio)', *Journal of vision*, 11(6):2, pp. 1–5.

Neuhauss, S. C. F. (2003) 'Behavioral genetic approaches to visual system development and function in zebrafish', *Journal of Neurobiology*, 54(1), pp. 148–160.

Nevala, N. E. and Baden, T. (2019) 'A low-cost hyperspectral scanner for natural imaging and the study of animal colour vision above and under water', *Scientific Reports*, 9(1), pp. 1–14.

Novales Flamarique, I. (2013) 'Opsin switch reveals function of the ultraviolet cone in fish foraging', *Proceedings of the Royal Society B*, 280: 20122490.

Novales Flamarique, I. (2016) 'Diminished foraging performance of a mutant zebrafish with reduced population of ultraviolet cones.', *Proc. R. Soc. B*, 283: 20160058.

Osorio, D., Ruderman, D. L. and Cronin, T. W. (1998) 'Estimation of errors in luminance signals encoded by primate retina resulting from sampling of natural images with red and green cones', *Journal of the Optical Society of America a-Optics Image Science and Vision*, 15(1), pp. 16–22.

Osorio, D. and Vorobyev, M. (1996) 'Colour vision as an adaptation to frugivory in primates', *Proceedings of the Royal Society B*, 263, pp. 593–599.

Pahlberg, J. (2007) *Spectral Tuning and Adaptation to Different Light Environments of Mysid Visual Pigments*. University of Helsinki.

Parichy, D. M. (2015) 'Advancing biology through a deeper understanding of zebrafish ecology and evolution', *eLife*, 4:e05635.

Park, J. H. *et al.* (2008) 'Crystal structure of the ligand-free G-protein-coupled receptor opsin', *Nature*, 454(7201), pp. 183–187.

Párraga, C. a *et al.* (1998) 'Color and luminance information in natural scenes.', *Journal of the Optical Society of America. A, Optics, image science, and vision*, 15(3), pp. 563–569.

Patterson, B. W. *et al.* (2013) 'Visually guided gradation of prey capture movements in larval zebrafish', *Journal of Experimental Biology*, 216(16), pp. 3071–3083.

Peitsch, D. *et al.* (1992) 'The spectral input systems of hymenopteran insects and their receptor-based colour vision', *Journal of Comparative Physiology A*, 170(1), pp. 23–40.

Rajendran, R. R. *et al.* (1996) 'Zebrafish interphotoreceptor retinoid-binding protein: differential circadian expression among cone subtypes', *The Journal of Experimental Biology*, 199, pp. 2775–2787.

Raymond, P. A., Barthel, L. K. and Curran, G. A. (1995) 'Developmental patterning of rod and cone photoreceptors in embryonic zebrafish', *Journal of Comparative Neurology*, 359(4), pp. 537–550.

Robinson, J. *et al.* (1993) 'Zebrafish ultraviolet visual pigment: absorption spectrum, sequence, and localization.', *Proceedings of the National Academy of Sciences of the United States of America*, 90(13), pp. 6009–6012.

Robinson, J., Schmitt, E. A. and Dowling, J. E. (1995) 'Temporal and spatial patterns of opsin gene expression in zebrafish (*Danio rerio*)', *Vis Neurosci*, 12(5), pp. 895–906.

Rodieck, R. W. (1998) 'Chapter 12 - Informing the brain', in *The First Steps in Seeing*. Sinauer Associates, Inc., pp. 266–291.

Rossel, E. (2017) *OtterVIS LGL spectrophotometer*. Available at: https://www.thingiverse.com/thing:2215840 (Accessed: 18 December 2017).

Ruderman, D. L., Cronin, T. W. and Chiao, C.-C. (1998) 'Statistics of cone responses to natural images: implications for visual coding', *Journal of the Optical Society of America A*, 15(8), p. 2036.

Rushton, W. A. H. (1972) 'Pigments and signals in colour vision', *The Journal of Physiology*, 220, pp. 1–31.

Saremi, S. and Sejnowski, T. J. (2016) 'Correlated Percolation, Fractal Structures, and Scale-Invariant Distribution of Clusters in Natural Images', *IEEE Transactions on Pattern Analysis and Machine Intelligence*, 38(5), pp. 1016–1020.

Saszik, S., Bilotta, J. and Givin, C. M. (1999) 'ERG assessment of zebrafish retinal development.', *Visual neuroscience*. Lund University Libraries, 16(5), pp. 881–8.

Schmitt, E. a and Dowling, J. E. (1999) 'Early retinal development in the zebrafish, Danio rerio:

light and electron microscopic analyses.', *The Journal of comparative neurology*, 404(4), pp. 515–536.

Semmelhack, J. L. *et al.* (2014) 'A dedicated visual pathway for prey detection in larval zebrafish', *eLife*, p. 3:e04878.

Siebeck, U. E. (2013) 'Chapter 17 - Communication in the Ultraviolet: Unravelling the Secret Language of Fish', in Witzany, G. (ed.) *Biocommunication of Animals*, pp. 1–420.

Siebeck, U. E. and Marshall, N. J. (2001) 'Ocular media transmission of coral reef fish - can coral reef fish see ultraviolet light?', *Vision research*, 41(2), pp. 133–149.

Simoncelli, E. P. and Olshausen, B. A. (2001) 'Natural Image Statistics and Neural Representation', *Annual Review of Neuroscience*, 24, pp. 1193–1216.

Soules, K. A. and Link, B. A. (2005) 'Morphogenesis of the anterior segment in the zebrafish eye.', *BMC developmental biology*, 5(1), p. 12.

Spence, R. *et al.* (2006) 'The distribution and habitat preferences of the zebrafish in Bangladesh', *Journal of Fish Biology*, 69(5), pp. 1435–1448.

Spence, R. *et al.* (2007) 'The behaviour and ecology of the zebrafish, Danio rerio', *Biological Reviews*, 83(1), pp. 13–34.

Stockman, A. and Sharpe, L. T. (2000) 'The spectral sensitivities of the middle- and long-wavelength-sensitive cones derived from measurements in observers of known genotype', *Vision Research*, 40(13), pp. 1711–1737.

Suliman, T. and Novales Flamarique, I. (2014) 'Visual pigments and opsin expression in the juveniles of three species of fish (rainbow trout, zebrafish, and killifish) following prolonged exposure to thyroid hormone or retinoic acid', *Journal of Comparative Neurology*, 522, pp. 98–117.

Takechi, M. and Kawamura, S. (2005a) 'Temporal and spatial changes in the expression pattern of multiple red and green subtype opsin genes during zebrafish development.', *The Journal of Experimental Biology*, 208, pp. 1337–1345.

Takechi, M. and Kawamura, S. (2005b) 'Temporal and spatial changes in the expression pattern of multiple red and green subtype opsin genes during zebrafish development', 208, pp. 1337–1345.

Tappeiner, C. et al. (2012) 'Visual acuity and contrast sensitivity of adult zebrafish', *Frontiers in*

*Zoology,* 9:10.

Tedore, C. and Nilsson, D.-E. (2019) 'Avian UV vision enhances leaf surface contrasts in forest environments', *Nature Communications*, 10: 238.

Toomey, M. B. *et al.* (2016) 'Complementary shifts in photoreceptor spectral tuning unlock the full adaptive potential of ultraviolet vision in birds', *eLife*, 5:e15675.

Trivedi, C. A. and Bollmann, J. H. (2013) 'Visually driven chaining of elementary swim patterns into a goal-directed motor sequence: a virtual reality study of zebrafish prey capture', *Frontiers in Neural Circuits*, 7, pp. 1–18.

Twig, G., Levy, H. and Perlman, I. (2003) 'Color opponency in horizontal cells of the vertebrate retina', *Progress in Retinal and Eye Research*, 22, pp. 31–68.

Uto, K. *et al.* (2016a) 'Development of a Low-Cost, Lightweight Hyperspectral Imaging System Based on a Polygon Mirror and Compact Spectrometers', *IEEE Journal of Selected Topics in Applied Earth Observations and Remote Sensing*. IEEE, 9(2), pp. 861–875.

Uto, K. *et al.* (2016b) 'Development of a Low-Cost Hyperspectral Whiskbroom Imager Using an Optical Fiber Bundle, a Swing Mirror, and Compact Spectrometers', *IEEE Journal of Selected Topics in Applied Earth Observations and Remote Sensing*, 9(9), pp. 3909–3925.

Wald, G. (1939) 'The porphyropsin visual system', *The Journal of General Physiology*, pp. 775–794.

Wald, G. (1957) 'The metamorphosis of visual systems in the seal lamprey', 40(6), pp. 901–914.

Warren, J. and CC-BY-SA 2017 Public Lab contributors (no date) *Desktop Spectrometry Kit 3.0*. Available at: https://publiclab.org/wiki/desktop-spectrometry-kit-3-0 (Accessed: 18 December 2017).

Webster, M. A. and Mollon, J. D. (1997) 'Adaptation and the Color Statistics of Natural Images', *Vision Res.*, 37(23), pp. 3283–3298.

White, R. H. *et al.* (1994) 'Wavelength Discrimination and the Role of Ultraviolet Vision in the Feeding Behavior of Hawkmoths', 26(4), pp. 427–435.

Whitmore, A. V and Bowmaker, J. K. (1989) 'Seasonal variation in cone sensitivity and short-wave absorbing visual pigments in the rudd *Scardinius erythrophthalmus*', *Journal of Comparative Physiology A*, 166, pp. 103–115.

Wilt, F. H. (1959) 'The Differentiation of Visual Pigments in Metamorphosing Larvae of *Rana catesbeiana*', *Developmental Biology*, 1, pp. 199–233.

Yokoyama, S. *et al.* (1999) 'Adaptive evolution of color vision of the Comoran coelacanth (*Latimeria chalumnae*)', 96, pp. 6279-6284.

Yoshimatsu, T. *et al.* (2016) 'Presynaptic partner selection during retinal circuit reassembly varies with timing of neuronal regeneration *in vivo*', *Nature Communications*. 7: 10590.

Yoshimatsu, T. *et al.* (2020) 'Fovea-like Photoreceptor Specializations Underlies Single UV Cone Driven Prey-Capture Behaviour in Zebrafish', *Neuron.* 107, pp. 1-18.

Zele, A. J. *et al.* (2018) 'Melanopsin photoreception contributes to human visual detection, temporal and colour processing', *Scientific Reports*. 8: 3842.

Zhou, M. *et al.* (2020) 'Zebrafish Retinal Ganglion Cells Asymmetrically Encode Spectral and Temporal Information across Visual Space', *Current Biology*. 30, pp. 1–16.

Zigman, S. (1971) 'Eye Lens Color: Formation and Function', *Science*, 171(3973), pp. 807–809.

Zimmermann, M. J. Y. *et al.* (2018) 'Zebrafish Differentially Process Color across Visual Space to Match Natural Scenes', *Current Biology*, 28, pp. 2018–2032.

# Appendix 1: Manual for the 60° hyperspectral scanner

As described in Nevala, NE and Baden, T. 2019. A low-cost hyperspectral scanner for natural imaging and the study of animal colour vision above and under water. *Scientific Reports* 9:10799.

*Overview*

In this document we provide detailed instructions how to construct a complete hyperspectral scanner as presented in the accompanying paper, including a bill of materials (BOM) and use instructions. The Arduino code and SCAD files are provided on the project's GitHub page at https://github.com/BadenLab/3Dprinting_and_electronics/tree/master/Hyperspectral%20scanner.

*Bill of Materials (BOM)*

All details of the parts used and estimated costs are listed in Table 1. Without the protector case housing and waterproofing the costs are approximately £113, excluding the spectrometer. With the protector case housing and waterproofing the costs are around £340. In addition to these parts, a working laptop with the Arduino IDE (https://www.arduino.cc) and the spectrometer software (in our case from Thorlabs (https://www.thorlabs.com/software_pages/viewsoftwarepage.cfm?code=OSA) installed are required. For the analysis we provide instructions using IGOR Pro 7 Wavemetrics (https://www.wavemetrics.com/order/order_igordownloads.htm).

*Circuit board*

The overall operational and circuit logic is show in Figure 1. The circuit can be completed simply with all wires as indicated, or by organising pieces on a custom circuit board.

**Table 1: Parts for hyperspectral scanner**

| | Supplier | Part number | Quantity | Unit price (£) | Full price (£) | Essential | Comments |
|---|---|---|---|---|---|---|---|
| **Electronics** | | | | | | | |
| Arduino Uno<br>https://www.amazon.co.uk/Arduino-A000066-ATMEGA328-Microcontroller-Board/dp/B008GRTSV6/ref=sr_1_3?ie=UTF8&qid=1525263060&sr=8-3&keywords=arduino+uno | Amazon | | 1 | 17.30 | 17.30 | Yes | Any cheap clone is OK. |
| MG90S Aluminum Metal Gear Servo Micro<br>https://www.amazon.co.uk/TowerPro-MG90S-Metal-Micro-Servo/dp/B00UB2ZBV0 | Amazon | | 2 | 9.54 | 9.54 | Yes | Comes in pack of 2. |
| 9V battery<br>https://uk.rs-online.com/web/p/9-volt-batteries/8264435/ | RS Online | | 1 | 1.80 | 1.80 | Yes | |
| USB cable type A/B (From laptop to Arduino)<br>https://www.amazon.co.uk/Cable-Type-1-80-Connection-EDM/dp/B078ZPXSVS/ref=sr_1_16?s=diy&ie=UTF8&qid=1525263526&sr=1-16&keywords=USB+cable+type+A+B | Amazon | | 1 | 1.89 | 1.89 | Yes | |
| USB 2.0 cable A to Mini B (From laptop to spectrometer)<br>https://www.amazon.co.uk/rhinocables%C2%AE-Male-Cable-black-Lengths/dp/B076H1CJKF/ref=sr_1_11?s=computers&ie=UTF8&qid=1525263132&sr=1-11&keywords=USB+cable+type+A+B | Amazon | | 1 | 2.50 | 2.50 | Yes | |
| Toggle switch<br>http://uk.farnell.com/multicomp/1md1t1b1m1qe/switch-dpdt-5a-120vac/dp/9473513 | Farnell | 1MD1T1B1M1QE | 1 | 2.41 | 2.41 | Yes | |
| 5 pin Din Plug<br>https://www.amazon.co.uk/Plug-Nickel-Finish-Rubber-Boot/dp/B000LAPU4A/ref=sr_1_2?s=diy&ie=UTF8&qid=1525264155&sr=1-2&keywords=DIN+5+pin | Amazon | NE325 | 2 | 2.27 | 4.54 | Yes | |
| 5 pin Din Chassis Socket<br>https://www.amazon.co.uk/pin-Chassis-Socket-Nickel-Finish/dp/B000LARV0Q/ref=sr_1_1?s=diy&ie=UTF8&qid=1525348842&sr=1-1&keywords=5+pin+Din+Chassis+Socket+Nickel+Finish | Amazon | NE328 | 2 | 1.66 | 3.32 | Yes | |
| BNC plug (male)<br>http://uk.farnell.com/pomona/4970/test-lead-black-red-149-22mm-500vrms/dp/2526735?st=BNC%20plug%20male | Farnell | 4970 | 1 | 9.68 | 9.68 | Yes | |
| Wiring (any)<br>https://uk.rs-online.com/web/p/hookup-equipment-wire/0331862/ | RS Online | 331-862 | 100 cm | 0.35 | 10.55 | Yes | |
| 9V battery clip<br>http://uk.farnell.com/bud-industries/hh-3449/battery-retainer-clip/dp/1650667?st=9V%20battery%20clip | Farnell | 8459-0674 | 1 | 0.88 | 0.88 | Yes | |
| SMB to BNC adapter cable | | | 1 | | | Yes | Included with spectrometer. |

**Other parts**

| | | | | | | | |
|---|---|---|---|---|---|---|---|
| 1150 Protector Case<br>https://peliproducts.co.uk/1150-protector-case.html | Peli products UK | 1150-000-110 | 1 | 48.50 | 48.50 | For underwater | |
| UniBond Repair Power Epoxy Plastic<br>https://www.amazon.co.uk/UniBond-Repair-Power-Epoxy-Plastic/dp/B003UGKTHK | Amazon | | 1 | 5.85 | 5.85 | For underwater | |
| Lapurete's Silica Gel Packets Desiccant<br>https://www.amazon.co.uk/Lapuretes-Desiccant-Regenerative-Humidity-Indicator-25%C3%9710g/dp/B01CHSA0JS | Amazon | | 1 | 9.14 | 9.14 | For underwater | Comes in pack of 25. |
| AquaMate Fish Tank Sealant<br>https://www.amazon.co.uk/Everbuild-LEUDBBNJS2125-AquaMate-Fish-Sealant/dp/B0012RRFCQ | Amazon | | 1 | 3.42 | 3.42 | For underwater | |
| Multipurpose water repellent silicone grease<br>https://www.amazon.co.uk/gp/product/B006O7HTDE/ref=oh_aui_detailpage_o09_s00?ie=UTF8&psc=1 | Amazon | | 1 | 3.99 | 3.99 | For underwater | |
| UVFS Broadband Window, Uncoated<br>https://www.thorlabs.com/thorproduct.cfm?partnumber=WG42012 | Thorlabs | WG42012 | 1 | 105.57 | 105.57 | For underwater | |
| PVC Tube (19mm inner/25 mm outer diameter)<br>http://pvctubeonline.co.uk/pvc_tube.htm | PVC Tube Online | PVC19mmT | 3 m | 10.85 | 10.85 | For underwater | |
| Steel sheet CR4 \| 250mm x 250mm x 1mm<br>https://www.amazon.co.uk/Steel-sheet-CR4-250mm-1mm/dp/B00KRF9G4Y/ref=sr_1_7?ie=UTF8&qid=1526301901&sr=8-7&keywords=metal+sheet | Amazon | | 1 | 4.99 | 4.99 | For underwater | Needs to be cut in smaller pieces |
| IP66 Weather resistant sealed 150*250*100mm ABS enclosure<br>https://www.amazon.co.uk/gp/product/B01M8I26BV/ref=oh_aui_detailpage_o02_s00?ie=UTF8&psc=1 | Amazon | | 1 | 13.55 | 13.55 | For underwater | |
| 2kg Empty and Filled Shot Bags (Lead weights)<br>https://www.amazon.co.uk/1kg-Empty-Filled-Shot-Bags/dp/B00M1WK3BQ/ref=sr_1_1?s=sports&ie=UTF8&qid=1526302223&sr=1-1&keywords=1kg+2kg+3kg+Empty+and+Filled+Shot+Bags+1kg+2kg+3kg | Amazon | | 1 | 18.50 | 18.50 | For underwater | |
| Square UV Enhanced Aluminum Mirror<br>https://www.thorlabs.com/thorproduct.cfm?partnumber=PFSQ05-03-F01 | Thorlabs | PFSQ05-03-F01 | 1 | 23.91 | 23.91 | Yes | |
| Square UV Enhanced Aluminum Mirror<br>https://www.thorlabs.com/newgrouppage9.cfm?objectgroup_id=264 | Thorlabs | PFSQ10-03-F01 | 1 | 35.19 | 35.19 | Yes | |
| Screw for mirror holders | | | 4 | | | Yes | Included with micro-servos. |

| | |
|---|---|
| **Total cost for only essential parts** | £113.31 |
| **Total cost for full system** | £337.67 |
| **Total cost for full system with spares** | £347.87 |

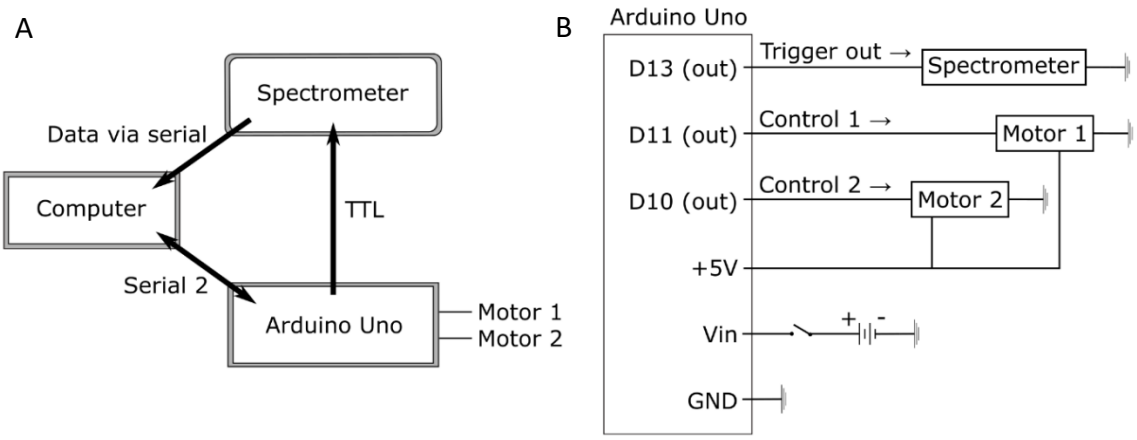


**Figure 1. (A)** The operational logic and **(B)** the circuit diagram.

*Printing 3D parts*

All 3D printed parts were designed using OpenSCAD which is freely available at (http://www.openscad.org/). All scripts are provided on the GitHub. The precise measurements of the printed parts are designed to fit the commercial protector case used (see Table 1, Fig. 2C) and a Thorlabs CCS200 spectrometer. If other types of cases, spectrometers or components are used, measurements for the base (Fig. 2A) should be adjusted accordingly. In addition to the base, other essential 3D printed parts for the scanner are the mirror holders attached to the two micro-servo motors and a pinhole placed in front of the spectrometer sensor (Fig. 2D). For the waterproofed version, tube and window holders are also needed (Fig. 2E and F). The dimensions of these are determined by the size of the window and tube used and should be adjusted accordingly if other versions are used. Before starting to assemble the scanner or the waterproof casing, make sure to have all the necessary components and 3D printed parts ready and in correct size.

A

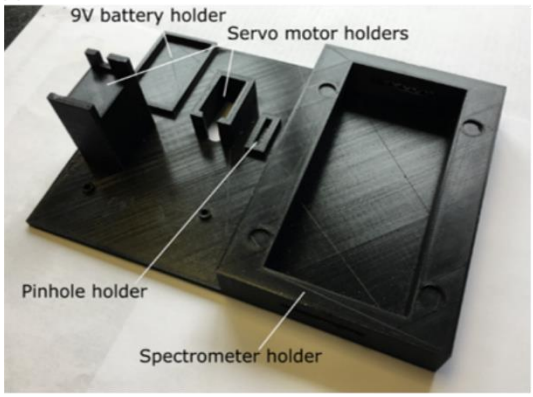
9V battery holder
Servo motor holders
Pinhole holder
Spectrometer holder

B

C

D

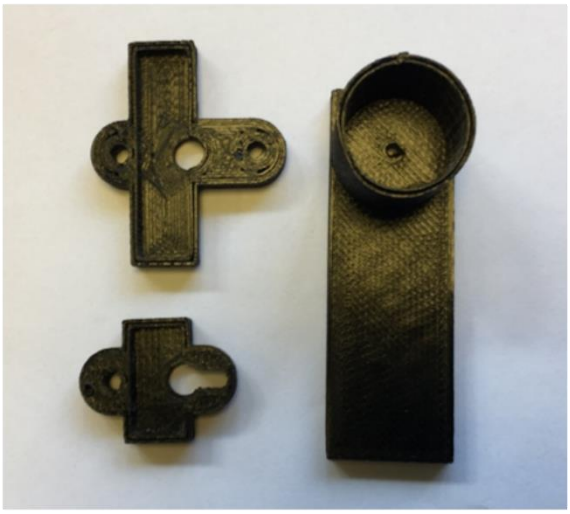

E

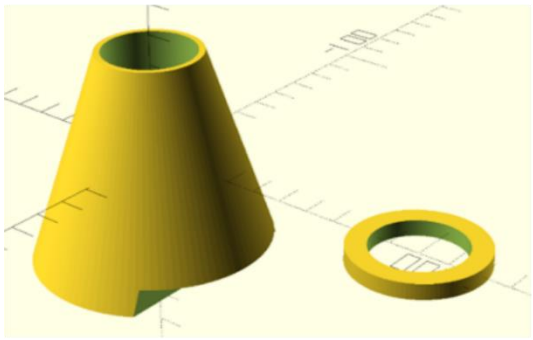

F

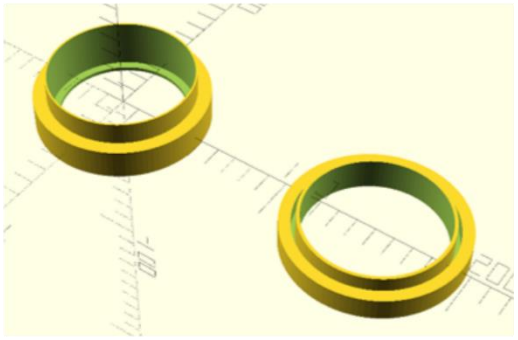

G

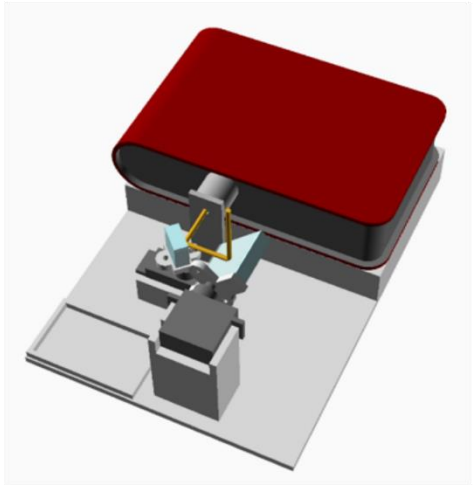

**Figure 2 (previous page). (A)** A 3D printed base showing slots for 9V battery, two servo motors, a pinhole and a spectrometer. The higher servo motor holder should be the one holding the big mirror and the lower one holding the smaller mirror. In addition, we drilled two small slits to use a strap to secure the spectrometer to the base. **(B)** The base inside the protector case with all the components. **(C)** The complete scanner with waterproofed housing. **(D)** 3D printed mirror holders and a pinhole. **(E)** Screenshot of the 3D parts for the outside (left) and the inside (right) support parts for the tube. **(F)** Screenshot of the 3D parts for the base (left) and the cap (right) parts of the window holder. **(G)** A schematic illustration of the optical path (Arduino, 9V battery and chords are left out for clarity).

*Assembling the scanner (after the electronics are assembled)*

1. Position the circuit and Arduino as shown above. This can be taped down if desired.
2. Attach the mirror holders to the servo-motors with screws that come with the servo-motors.
3. Place the servo-motors on the base. The servo-motor with larger mirror holder should be placed on the more elevated motor holder (Fig. 2B). Attach mirrors to the servo-motors. The holders should be tight enough to hold the mirrors without additional support, but if not, a small dot of the sealant can be used to glue them into place.
4. Attach the 9V battery to the base and connect it with the circuit board.
5. Add the spectrometer and mount the pinhole in front of it.
6. Connect the power cords between laptop and Arduino + spectrometer, and the trigger cord between spectrometer and Arduino.

*Waterproofing the protector case*

1. To insert the front window, drill a 75 mm diameter hole to the front panel of the case (Fig. 3). Insert the base part of the window holder to the inner side of the case.
2. Carefully add two-component glue around the window (be careful not to smear the front or back parts of the window with glue) and insert the window to the holder. There should be enough glue all around the window to prevent any water to leak in! Carefully remove any extra glue from the window.
3. Add two-component glue to the outer rim and the groove of the cap part and press it firmly against the base part. Leave to dry.

4. Use fish tank sealant to carefully cover all possible seams inside and outside. Be careful not to leave any sealant on the window. Let the sealant dry over night or until it is completely set.

5. Confirm that the window inserted is waterproof before continuing to the next part.

6. Drill a 26 mm diameter hole as shown in Fig. 3 for the cables/tube. The hole should be positioned in the middle of the panel at the intended top of the scanner. Pass the tube through the hole, the tube should be a very tight fit.

7. Take the 3D printed inside support for the tube and apply two-component glue on one side of the part. Press the part firmly against the wall inside the box around the tube hole.

8. Take the 3D printed outside support for the tube and apply two-component glue on the wider bottom part of it. Press firmly against the outside part of the wall around the tube hole (the stepped edge should go on top of the lid only a little bit).

9. Leave to dry.

10. Take the tube and apply a large amount of sealant around the outer part of it for approximately 5 cm length. Push the tube through the holders until the edge of the tube is evenly levelled with the inside tube holder (so that no additional tube projects inside the case).

11. Apply ample sealant between the outside tube holder and the tube. The sealant can “overflow” a little bit, but make sure to leave an even surface. Apply a thick but smooth layer of sealant to all possible seams around the inside and outside tube holders (the inside tube holder can be “covered” with silicone as long as there is enough space for the cords to get through the tube). Leave to dry over night or until the sealant is completely dry.

12. Confirm that the box is waterproof before continuing to the next part.

13. Pass the power cord for Arduino and the spectrometer trigger cord through the tube (alternatively this can also be done before inserting the tube into its place).

14. To further improve the waterproofing, we also added a light layer of grease in the seams of the case. Appropriate care and testing should be completed before the case is placed under water with electronics and spectrometer inside.

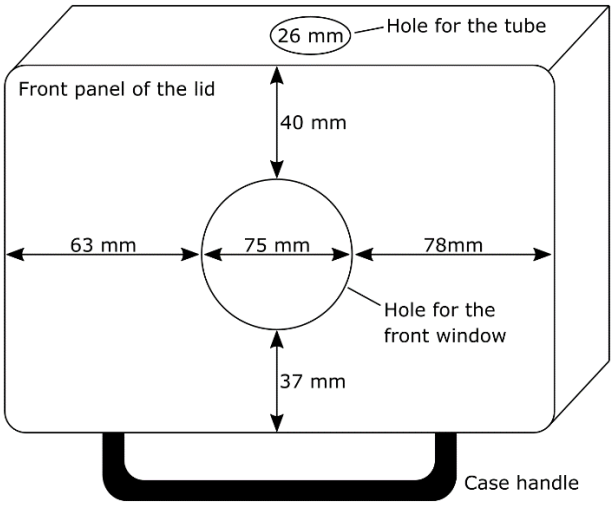


**Figure 3.** Positions of the holes for the window on the front panel of the case lid and the tube.

*Assembling the scanner inside the protector case*

1. Leave approximately a 1.5 – 2 cm thick layer of foam that comes with the case at the bottom. Place the base with all components attached to it on top of the foam. For underwater measurements we added scrap metal plates underneath the foam to decrease its buoyancy to the point where it would robustly sit on a riverbed at ~50 cm depth. In addition, or alternatively, lead weights can be used.

2. Attach the power cords to Arduino and spectrometer, and the trigger cord between the two.

3. Place the base so that the centre of the bigger mirror is centred relative to the front panel window. Secure the position using leftover foam pieces. Additional foam should also be applied carefully on top of the spectrometer and the other parts of the base (but not the mirrors) to prevent any additional movement when the scanner is turned to upright position. If necessary, the spectrometer can also be attached to the base with straps or tape.

4. Close the lid. Check that the big mirror is not touching the front window.

5. To hold the scanner in an upright position, we used an additional hard plastic box (Fig. 4).

6. To prevent condensation inside the box, we recommend using humidity absorbing Silica Gel Packets inside the scanner box.

**Figure 4.** A hard plastic box supporting the upright position of the scanner. The edge of the plastic box had to be cut to prevent covering of the window of the scanner.

*Operating the scanner*

1. Connect the Arduino and the spectrometer to the laptop. Turn the battery switch on Arduino in to "ON" position. This provides an additional power source for the Arduino from the 9V battery.
2. Launch both Arduino IDE and Thorlabs spectrometer software on the laptop.
3. Create an empty folder called "Spectra" on the Desktop.
4. Preparing the Thorlabs spectrometer software (these steps should be re-done each time the software is started as it does not store these preferences):
    a. Under the "Sweep" bar, choose "Trigger Mode: Software" and take one single test measurement by pressing "Single" (Fig. 5). A single sweep spectrum should appear on the screen.
    b. Under "File", choose "Export trace" and save the test file in the "Spectra" folder created earlier. Choose "text file" in the "save as type". Press "save".
    c. On the window popping up, choose "comma" for the "Separate Columns by". Press "Ok". Now all the files for the actual measurements will be saved as text files and columns will be separated by commas. Delete the test file from the "Spectra" folder before doing any measurements!
    d. Change the "Trigger Mode" to "External" before starting a measurement.

e. Choose a desired Integration Time (in ms, Fig. 5). Note: this must be smaller than the “Sampling time” in Arduino script, which defines the mirror movement intervals. Typical values used are approximately 100-200 ms for the Integration time and 260-500 ms for the Sampling time.

5. Preparing the Arduino script:

   a. Upload the “servo*.ino” script to the Arduino using the Arduino IDE (if in doubt how to do that, consult the Arduino online help). Choose a desired sampling time (in ms, Fig. 6). Note: this must be longer than the “Integration time” on the Thorlabs software.

   b. Press “Save” and “Upload”. Once complete, open the serial monitor.

   c. By moving the mirrors with AWSD commands (see “Operating the Arduino code”), move the mirrors until you can see the pinhole hole in the centre of each mirror by looking straight down at the bigger mirror through the box window. Enter these mirror positions as the X- and Y-offset values in the script (Fig. 6). Save and upload again. The mirrors should ideally be re-aligned like this every time before starting a measurement, and certainly if the box if substantially moved or reconnected.

   d. Choose a desired scan mode.

6. Go back to the Thorlabs software. Under “File”, choose “Auto Save”. Output directory should be set to the “Spectra” folder. Set naming of the files as wanted and File Format to “text”. Press “Ok”. In the pop-up window choose “Ok”.

7. Under “Sweep”, press “Repeat”. Ensure that the “spectra” folder on the Desktop is empty.

8. Go back to Arduino Serial Monitor and choose “P” followed by pressing Enter to run the scan.

9. Measured scans should appear in the spectra folder. After the scan is finished, move the data to a separate folder before taking any more measurements to avoid mixing up the data.

10. If the scanner is measuring fewer or extra points than the scan mode is indicating, integration and/or sampling time should be adjusted until correct number is achieved. However, with each scan mode one additional point is always included (e.g. with “Spiral

1000” mode correct number of scanned points is 1001, with “Spiral 600” mode correct number of scanned points is 601 etc.). The first sweep should always be excluded from the analysed data (just delete it).

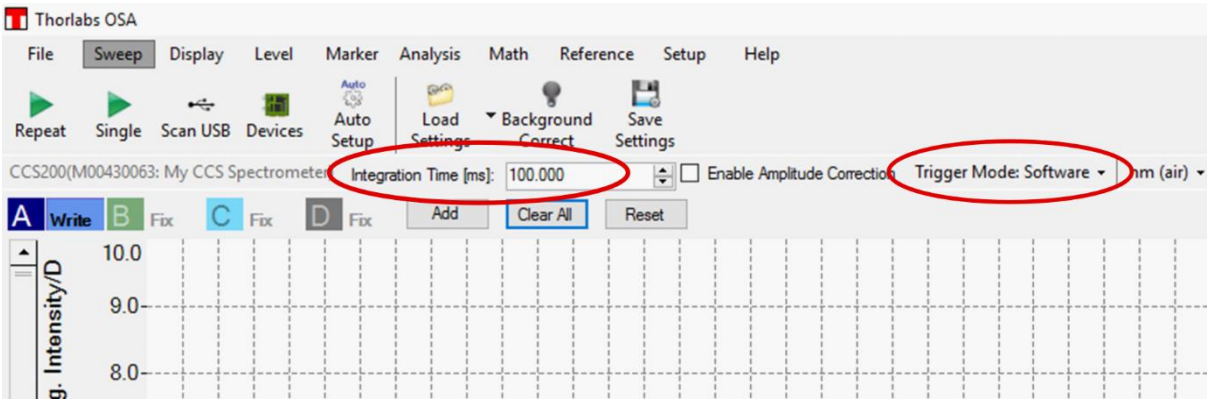


**Figure 5.** A screenshot of the Thorlabs software for the spectrometer highlighting where the Integration time and the Trigger mode can be changed.


**Figure 6.** A screenshot of the Arduino IDE showing where the X- and Y-offsets and the sampling time can be modified.

*Operating the Arduino code*

In the serial command window, the below commands (followed by ”Enter”) can be used:

Z – Set both servo-motor offsets to the Xoffset and Yoffset values as defined in the top of the Arduino script.

D – Calibrate X servo-motor to right.

A – Calibrate X servo-motor to left.

W – Calibrate Y servo-motor upwards.

S – Calibrate Y servo-motor downwards.

Q – Cycle through the different scan modes (explained below, Fig. 7).

R – Send 50 triggers without changing the position of the servo-motors (useful for testing).

T – Send one individual trigger without changing the position of the servo-motors (useful for testing).

P – Execute the selected scan mode.

*Scan modes*

Figure 7 shows the pattern and path of the four possible scan modes (a 100 points square and 300, 600 or 1000 points spirals, Fig. 7). Each of them covers the same 60-degree area with different angular spacing. The paths covering all the measuring points are optimised to achieve a minimal path length.

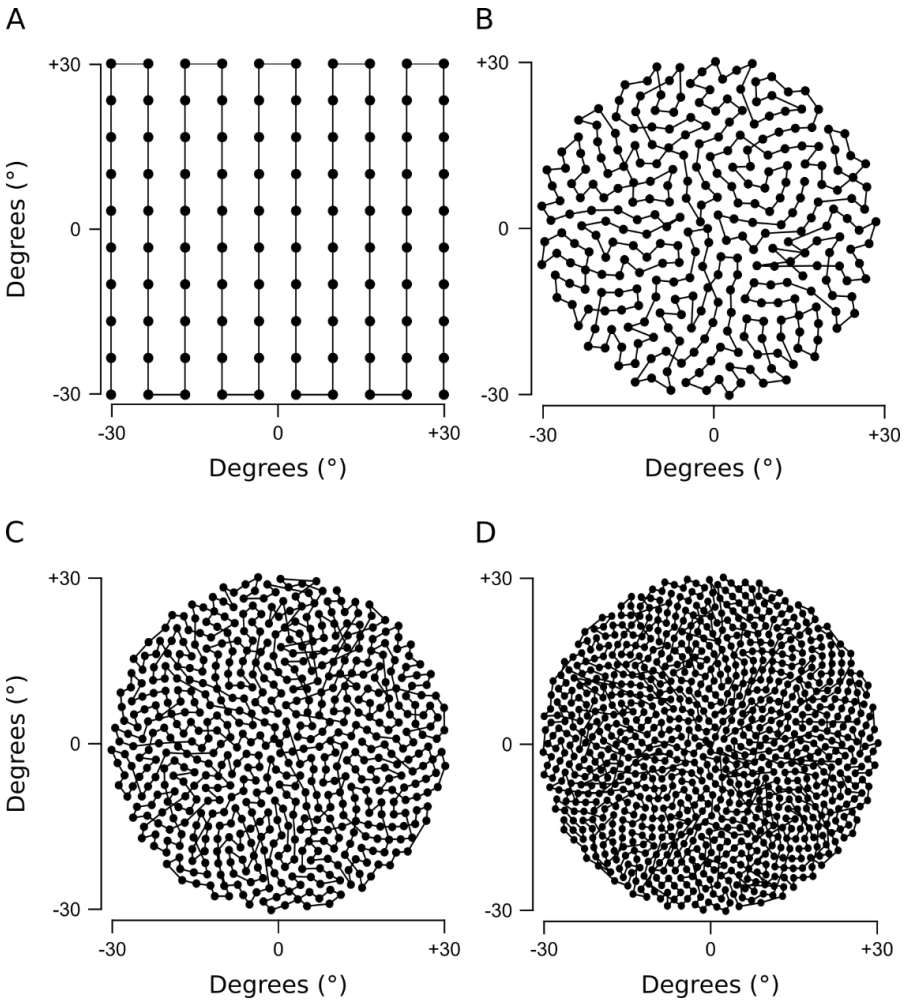


**Figure 7.** The 4 possible scan modes. **(A)** 100 points square. **(B)** 300 points spiral. **(C)** 600 points spiral. **(D)** 1000 points spiral.

*Analysis in Igor Pro*

1. Download the Scanner_empty.pxp Igor experiment file and the Scanner_v15.ipf Igor script file from the project's GitHub page.
2. Save the Scanner_empty.pxp file with a different file name.
3. Create a new folder under "root". Each individual complete scan requires a separate folder. Move the red arrow next to the "root" folder and drag it to point to your (currently empty) measurement file.
4. Open the folder where the raw data from the scan is. Select all the files but <u>leave the first point out</u>. By selecting the first selected file (the second file all in all), drag all the files to Igor. For each pop-up window, select "Load". Note that each individual file creates two waves in Igor (one of them holding the data, one holding the wavelengths).

IMPORTANT: When dragging the individual “scan pixels” into Igor, make sure that you highlight the full array and then click and drag the first measurement to load the entire dataset at once but in order. Otherwise Igor may load them in the wrong order (it will just auto-name them wave0, wave1, wave2 etc so you will not know it did this unless you check).

5. Choose File – Open File – Procedure, and choose the Scanner_v15.ipf file to open the script in the experiment.
6. Run the function “Collect(DataFolder)”, where DataFolder is replaced with the name of your folder holding the data in Igor. This removes every other wave from the measurement folder (the wavelength waves) and creates one wave with all the data in it.
7. Choose the desired animal you want to analyse your data with. In the script, set the “Chromat type” (Fig. 8) to the number of opsins the animal uses (see the folder for the opsin types in the Data Browser). For example, zebra finch have 4 different opsins, so the Chromat type is set to 4.
8. If using the waterproofed casing, the edges of the image can be cropped in “XEdgeCrop_deg” (= 0 to 30 degrees) to get rid of the shadowing caused by the case (Fig. 8).
9. The image can be rotated 90 degrees using the “flipflop” variable (=0 or 1) in case the scanner is used in any other position than showed in Figs. 2C and 4.
10. Run the analysis using function Analyse(DataFolder,Scanpath,species,display_stuff). As an example, the function can be written as Analyse("Cactus","Scanpaths:Spiral1000_30deg","Zebrafinch_oil",1) where “Cactus” is the name of the data folder, “Scanpaths:Spiral1000_30deg” is the scan path used to collect the data, “Zebrafinch_oil” is the name of the folder under “Opsins” folder holding the desired opsin templates for zebra finch and “1” (or alternatively “0”) will display or not display the image after analysis. An example of the result after analysis is shown in Fig. 9.

```
63  function Analyse(DataFolder,Scanpath,species,display_stuff)
64  string DataFolder,Scanpath,species
65  variable display_stuff // 0 or 1
66
67  // Chromattype needs to be set to the number of different cones the animal has
68  variable Chromattype = 4
69
70  // How much the image is cropped from the right and left sides. This is only needed
71  // waterproof boxing is used.
72  variable XEdgeCrop_deg = 0
73  // Hack to kill interpolation edge artifact
74  variable extracrop_px = 4
75
76  // If set to 1, rotates the image 90 degrees right + mirrors it
77  variable flipflop = 1
78
```

**Figure 8.** A screenshot of the Igor script showing where the Chromat type, Edge cropping and flipping the scan can be modified.

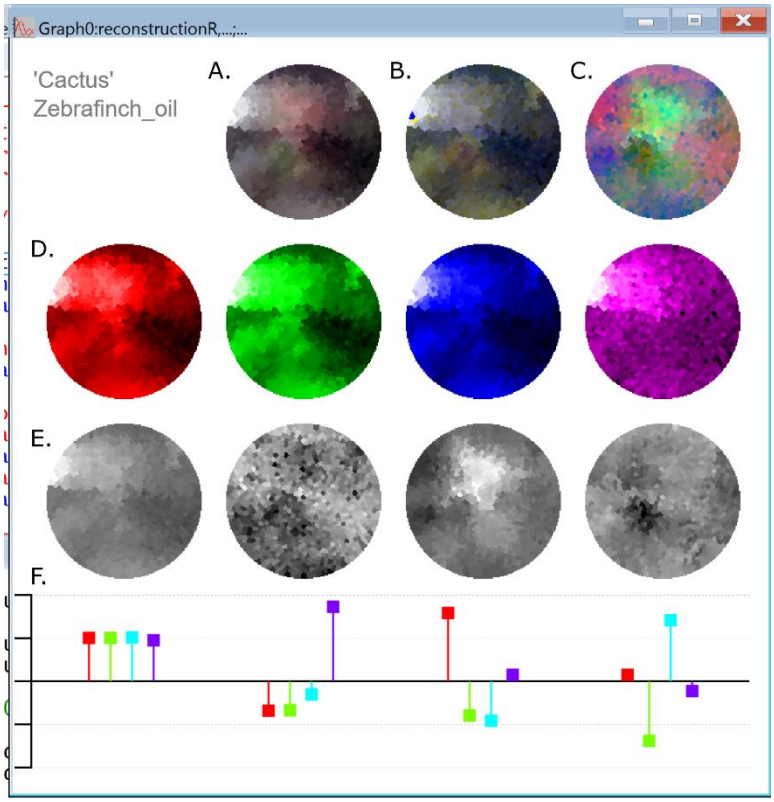


**Figure 9.** An example result graph from Igor after analysis. **(A)** An RGB (Red, Green, Blue) reconstruction of the monochromatic opsin channels from **(D). (B)** Combination of the first 3 opsin maps (from D) as an RGB image. **C,** RGB reconstruction of the principal components in **(E). (F)** Loadings explaining how much information is needed from each opsin channel in D.

# Appendix 2: All 31 measurements taken with the 60° scanner

For each measurement, picture of the scanned scene with an approximation of the scanned area (yellow circle), opsin activation maps for red (R), green (G), blue (B) and UV (U) analysed with zebrafish larva spectral sensitivity, an RGB reconstruction and PC RGB reconstruction is shown. In addition, pictures of the field sites where the measurements were taken are shown: field site 1 (measurements 1-9), field site 2 (measurement 10), field site 3 (measurements 11-17), field site 4 (measurements 18-24), field site 5 (measurements 25 and 26) and field site 6 (measurements 27-31).

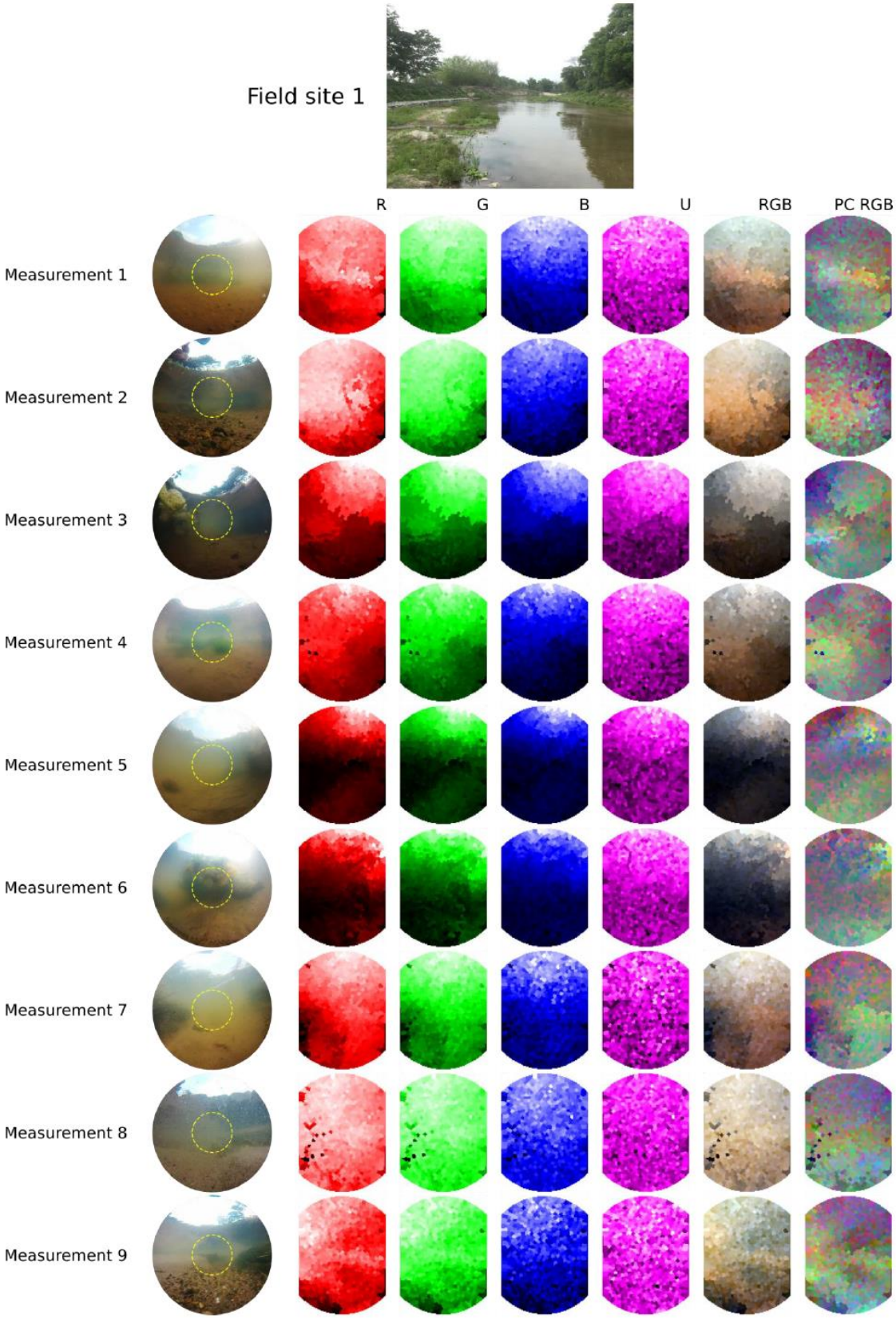
Field site 1
R
G
B
U
RGB
PC RGB
Measurement 1
Measurement 2
Measurement 3
Measurement 4
Measurement 5
Measurement 6
Measurement 7
Measurement 8
Measurement 9

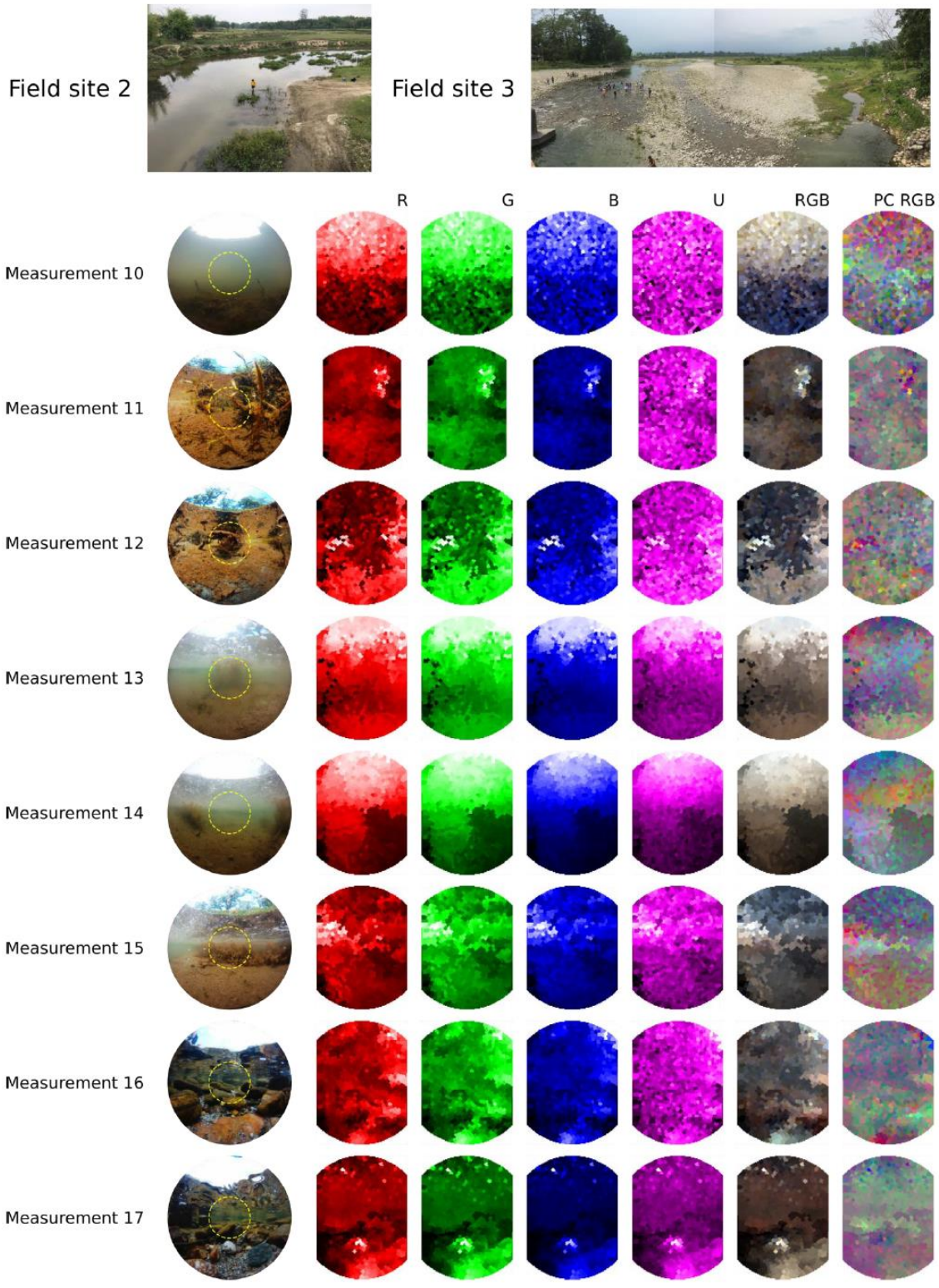
Field site 2
Field site 3
R
G
B
U
RGB
PC RGB
Measurement 10
Measurement 11
Measurement 12
Measurement 13
Measurement 14
Measurement 15
Measurement 16
Measurement 17

Field site 4

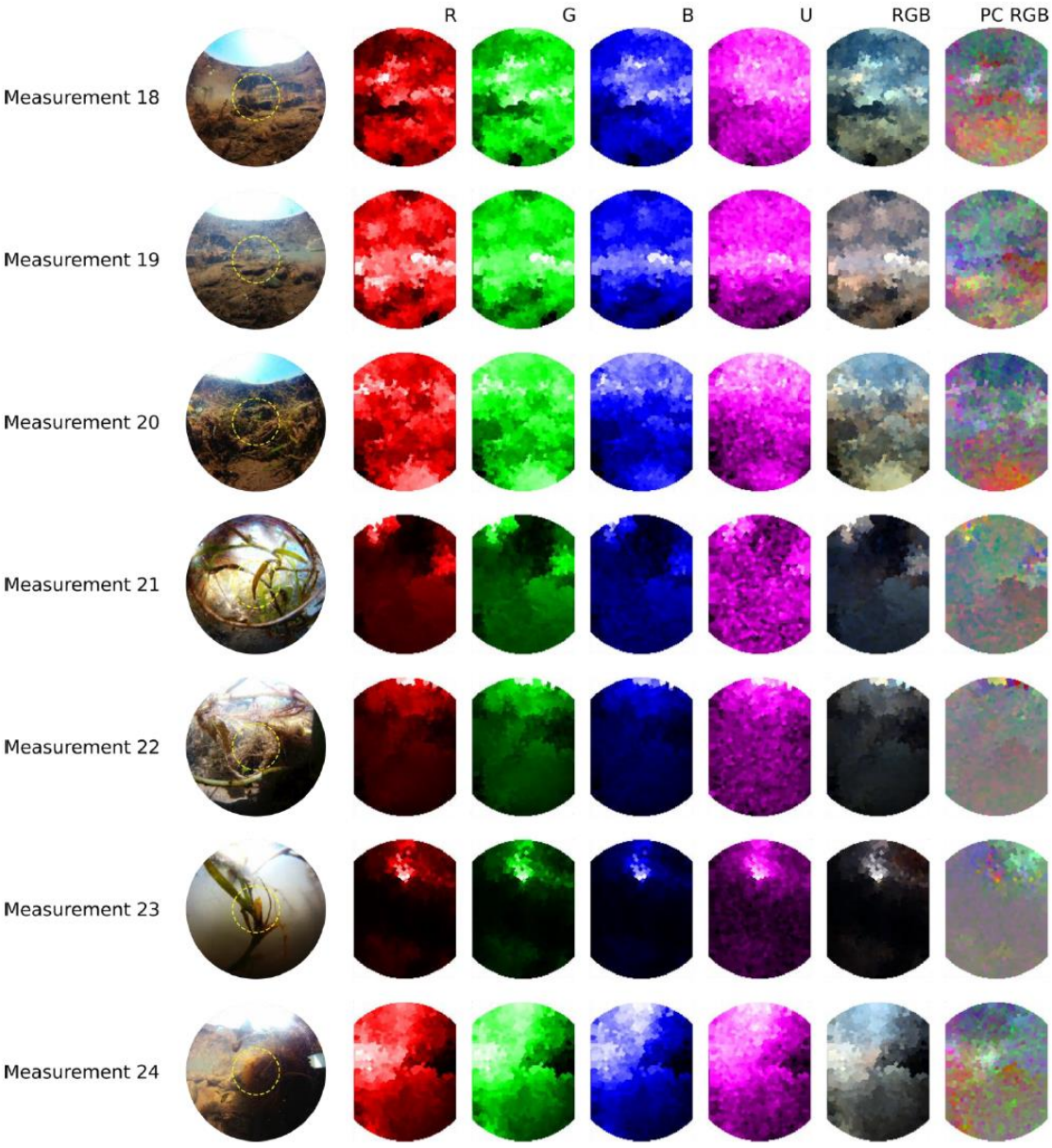
R
G
B
U
RGB
PC RGB
Measurement 18
Measurement 19
Measurement 20
Measurement 21
Measurement 22
Measurement 23
Measurement 24

Field site 5

Field site 6